Radar Altimeter General Waveform Model and Its Application to Cassini Mission

by

Guido Vingione

Department of Aerospace and Mechanical Engineering,

Second University of Naples, Aversa

Italy

November 2007

This page is intentionally left blank.

TABLE OF CONTENTS

TABLE OF FIGURES

ABSTRACT

Since the first dedicated altimeter was launched on Seasat platform in 1978, the technology for conventional (pulse limited) radar altimeters has reached a certain level of maturity thanks to the relatively high number of successful altimetry missions that have been launched or are now in development. Recent attention has been directed towards different altimeter designs: off-nadir looking altimetry, multi-beam altimetry, interferometric altimetry or, more in general, towards altimetry designs that achieve illumination of broader swath of the target surface. The above designs are especially advantageous for interplanetary exploration in which the altimeter sensing conditions are conditioned by mission requirements (i.e. flyby pass). The advantage to use radar altimeter instrument (RA) for exploring target surface in different scenarios (ocean, land, ice) consists in the possibility to predict an analytical function representing the Impulse Response (IR) backscattered from a target surface. However when dealing with space based radar altimeter observations of planetary bodies (like in the Cassini Mission) it is easy to show that some of the classical assumptions are often no longer valid. Therefore the classic altimetry model (i.e. Brown, 1977) cannot be used in order to fit the altimeter waveforms.

The aim of this work is to study a general waveform model independent from particularly Radar altimeter sensing mode. Starting from the same hypotheses made by Brown, but using a different approach, an analytical model of the average altimeter echo waveform is derived. The analytical function obtained, unlike other numerical models introduced in several scientific papers [1, 5, 11, 16, 29], allows to implement an efficient processing algorithm based on Maximum Likelihood Estimation theory (MLE), in order to infer statistical information about the sensed surface (i.e. slope, roughness, backscattering coefficient). Proposed model has been then compared with numerical solution and the simulations clearly report that maximum error in implementing the analytical solution (in a best fitting sense) is less than 2%.

Furthermore the model presented in this work represents the core of the nominal processing algorithm for the Cassini Processing Altimetric Data

ground system (actually integrated at Thales Alenia Space premises in Rome) that has been conceived in order to process the data collected by the Cassini Radar, while operating as an altimeter. The presented theoretical model is considered suitable to describe the radar Altimeter Impulse Response independently from sensing scenarios (nadir, off-nadir, beam limited, pulse limited, etc.) since it reduces substantially the errors in topographic heights estimation with respect to conventional numerical solutions.

ABSTRACT (ITALIANO)

Nell'ultimo decennio le indagini scientifiche conseguite con Radar Altimetri (RA) montati a bordo di satelliti artificiali, hanno raggiunto risultati tali da giustificarne il continuo interesse da parte della comunitá scientifica mondiale. In tal senso la tecnologia radar cerca di venire incontro alle continue esigenze della comunitá scientifica, studiando nuove configurazioni che ormai molto si discostano dai designs convenzionali propri della prima generazione di Radar Altimetri, (ERS, RA2, Topex, etc.) per i quali la superficie illuminata dal fascio radar è esclusivamente caratterizzata o dall'ampiezza dell'impulso trasmesso (pulse limited configuration) o dall'ampiezza del fascio d'antenna (beam limited configuration).

A fronte di una sempre piú matura tecnologia hardware, gli studi teorici sull'interpretazione dei dati altimetrici telerilevati si è basata per decenni sui metodi classici proposti dalla letteratura scientifica. Pertanto non sempre i modelli classici possono essere utilizzati per predire, studiare o simulare le performances dei Radar Altimetri di nuova generazione, con particolare riferimento ai RA impiegati per le esplorazioni planetarie (Cassini Radar, Sharad, Marsis, Mercuri RA, etc). In tale ambito si muove lo studio descritto nel presente lavoro di tesi, ponendosi come scopo ultimo, l'individuazione di un modello analitico che descrivesse le prestazioni di un RA a prescindere dalle particolari condizioni operative (quali la quota operativa, l'off-nadir, beamwidth, banda del segnale).

Partendo dalle ipotesi classiche discusse in Brown 1977, sono stati individuati due modelli analitici per la simulazione della Risposta Impulsiva degli Altimetri, uno valido per angoli di puntamento Off-nadir "piccoli" e l'altro per "grandi" Off-nadir, individuando come soglia di transizione tra i due scenari il valore di 0.37°. Utilizzando tale soglia (durante la fase di processamento) per la selezione del modello da utilizzare, si garantisce un errore relativo inferiore al 2% rispetto ad un modello non-analitico computato con tecniche numeriche.

Ricordiamo esplicitamente che la necessitá di un modello analitico è

strettamente legata alla possibilitá di effettuare analisi di post-processing delle forme d'onda ricevute da Radar Altimetri. Tali indagini, infatti, prevedono l'utilizzo degli strumenti classici di integrazione (e derivazione) multipli, propri dell'Analisi Complessa, i quali, applicati a modelli che non prevedono soluzioni analitiche per le operazioni richieste, rendono l'algoritmo di difficile implementazione e non risponde all'esigenza di poter ricavare informazioni sulla superficie target partendo dall'analisi delle forme d'onda telerilevate.

In questo contesto, ad una prima fase di studio e calcolo del modello è seguita la fase di validazione scientifica del modello stesso e l'implementazione dello stesso nel Cassini Processing Altimetric Data System installato nei laboratori di Thales Alenia Space in Roma. Per validazione si è inteso sia il processo di controllo dell'errore durante l'intera fase di processing, sia l'implementazione di algoritmi per dimostrare l'efficienza (in senso statistico di minimizzare la varianza della stima) del modello tramite il confronto con altri algoritmi di processamento o tramite simulazioni numeriche ad hoc.

Alle considerazioni sulla validazione del modello, segue, l'analisi delle forme d'onda ricevute dalla sonda Cassini durante i primi fly-by e la descrizione dei principali risultati ottenuti apportando correzioni di post-processing.

Le analisi e le considerazioni che di seguito sono descritte sono state inserite nel contesto di un progetto, finanziato dall'ASI, e realizzato presso il Consorzio di Ricerca CORISTA, per lo sviluppo di un Tool software per il processamento delle telemetrie altimetriche provenienti dalla missione Cassini-Huygens, il cui scopo è l'indagine di Saturno e del suo sistema di anelli e lune, ed in particolar modo della luna Titano.

I risultati ottenuti, le metodologie ed i modelli sviluppati durante il trienno di ricerca sono stati pubblicati su riviste specializzate e presentati in Conferenze Nazionali ed Internazionali a cui sono seguite pubblicazioni (vedi Appendice B).

ACKNOWLEDGMENTS

I wish to thank people, friends and colleagues who contributed in many different ways to the accomplishment of the present work. I'm very grateful for so much help. In particular, I like to thank Marco D' Errico, Alessandra Buongiorno and Gianni Alberti for their continuous support in coordination of the technical aspects of the present study.

Furthermore, I am much indebted to Eric Monjoux: his friendly and valuable support allowed the finalization of this work.

The Centre for Remote sensing research CORISTA at Naples is gratefully acknowledged for supplying me with the opportunity to work in the frame of Cassini Mission.

I also like to thank Alessandra Tassa, Andrea Tesseri and Luca Festa for the helpful discussions I had with them.

ABBREVIATION

ABDR	Altimeter Burst Data Record
AHAG	Cassini ALTH with Auto Gain
ALAG	Cassini ALTL with Auto Gain
ALT	Cassini Radar Altimeter
ALTH	Cassini Altimeter High-Resolution
ALTL	Cassini Altimeter Low-Resolution
ASDC	ASI Science Data Center
ASI	Agenzia Spaziale Italiana
BL	Beam Limited
BODP	Burst Ordered Data Products
COTS	Commercial Off The Shelf
DAS	Data Archiving Subsystem
ESA	European Space Agency
FSIR	Flat Surface Impulse Response
FTP	File transfer Protocol
GUI	Graphical User Interface
HW	Hardware
IR	Impulse Response
ISS	Imaging Science Subsystem
JPL	Jet Propulsion Laboratory
LBDR	Long Burst Data Record
MLE	Maximum Likelihood Estimator
MT	Map Tool
PAD	Processing of Altimeter Data

PDS	Planetary Data System
PL	Pulse Limited
PT	Production Tool
RA	Radar Altimeter
SBDR	Short Burst Data Record
S/C	Spacecraft
SDE	Software Development Environment
SIS	Software Interface Specification
SLT	Science Look Tool
SUM	SW User Manual
SW	Software
TBF	Target Body Fixed

1 INTRODUCTION

As soon as the first artificial satellites were launched, in the 1960s, remote sensing of the Earth surface and in particular radar altimetry produced an incredible amount of information on many unknown aspects of the Earth system. In fact, both oceanography and geophysics lived a revolutionary period as a frequent and global measurement of the shape of the ocean and ice surface became possible.

Satellite altimetry offers the capability to observe the Earth in a time frame of several days, providing data products on a grid-scale (the small footprint of the measurement itself and the sampling frequency along the orbital path offer only a limited coverage). Due to the favourable reflective properties of water, the method of altimetry is especially suitable for measurements over the ocean. The spaceborne height measurements technique of the sea surface provide in effect not only the height estimation, but an integrated information set along the sensing path, from the target surface to the spacecraft. The analysis of this altimetry data is being used in a great variety of applications involving such fields as meteorology, climate, ocean topography, land topography, ocean current, geoid modelling, etc. As far as the performance is concerned, the accuracy of the instrument currently achieved fully satisfies the users, since instrument related errors are of the same order of magnitude or better than external error sources (such as ionospheric/tropospheric propagation effects, orbit knowledge, tides/currents etc…) [11].

The high scalability of the altimeters instrument and the possibility to use analytical models to predict the altimeters performance, it allows to design different sensing scenarios. In fact, recent attention has been directed towards different designs: off-nadir looking altimetry, multi-beam altimetry, interferometric altimetry or, more in general, towards altimetry designs that achieve illumination of broader swath of the target surface.

The above designs are especially advantageous for interplanetary exploration in which the altimeter sensing conditions are conditioned by mission requirements (i.e. flyby pass). As previously stated, the advantage to use radar altimeter instrument (RA) for exploring target surface in different scenarios (ocean, land, ice) consists in the possibility to predict an analytical function representing the Impulse Response (IR) backscattered from a target surface. Conventional Radar altimeters are supported by non-controversial mathematical models relating the return waveform to target surface backscattering. These models have been carried out to fit the range compressed data and evaluate the time reference (pulse centroid) in order to compute the range to target heights. It is worth noting that the models presented in literature are describing the IR for RA working exclusively in pulse limited or beam limited mode. However when dealing with space based radar altimeter observations of planetary bodies (like in the Cassini Mission) it is easy to show that some of the classical assumptions are often no longer valid. As a matter of fact, the radar pulse cannot be very short and in addition the distance from the planetary body and the dimension of the body itself can be such that the radar altimeter is forced to work in a transition region between pulse and beam limited modes. Therefore the classic altimetry model (i.e. Brown, 1977) cannot be used in order to fit the altimeter waveform.

The aim of this work is to study a general waveform model independent from particularly Radar altimeter sensing mode. The proposed approach consists in solving the classical integral-equations modelling the altimeter performance [13], by applying the functional analysis method, in order to obtain an analytical function describing the IR at varying parameters (off-nadir, roughness, beamwidth etc). The analytical function obtained, unlike other numerical models introduced in several scientific papers [7-29], allows to implement an efficient processing algorithm based on Maximum Likelihood Estimation theory (MLE), in order to infer statistical information about the sensed surface (i.e. slope, roughness, backscattering coefficient).

Starting point of the present study is the Brown model equation, which models the IR for altimeters in typical “pulse limited” configuration.

The Brown assumptions are valid for all the altimetry systems, independently from their specific configuration or operational scenarios. Therefore it is worth noting that, these assumptions do not restrict the analysis described in section 3 to any particular scenario.

The results of the study have been then applied in the frame of Cassini mission in order to process the data sensed by the Cassini Radar in altimeter mode. In particular, proposed models have been implemented into the Cassini Processing Altimetric Data ground system (see section 4.2) and represent the core of the heights retrieval algorithm.

Following the above considerations, the present work is organized in order to introduce, gradually, the problematic of altimetry measurements, starting from general assumptions to specific model derivation and implementation.

In particular, Chapter 2 is dedicated to Satellite Altimetry principles, by providing a brief overview of the technological evolution of the altimeter instrumentations and applications (section 2.1) and then describing, more in details, the techniques of the altimetry measurements (section 2.2).

The analysis and models computation is detailed in section 3, by describing the analytical aspects of the proposed approach and their implications in altimetry data processing.

The analysis, described in section 3, has been differentiated by considering separately the two sensing modes:

1. Nadir Looking. The model computation for this configuration is described in section 3.1.
2. Off-Nadir Looking. The model computation for this configuration is described in sections 3.2 and 3.3.

Concerning above off-Nadir configurations, the following considerations are needed. In fact, it is possible to distinguish two Off-Nadir operational scenarios:

- Near Nadir configuration, in which the off-nadir angle is comparable with the antenna 3dB aperture. This configuration allows to sense a footprint greater than nadir looking and it is being used in a great variety of applications involving interferometric approach.
- Off-Nadir configuration, in which the off-nadir angle is greater than the antenna 3dB aperture (i.e. off-nadir angle > 1deg). This configuration is used when mission specific goals require a particular attitude or, more typically, when the spacecraft is multi-sensor and the radar is multimode. Therefore the off-nadir angle becomes a compromise between mission requirements and sensor requirements.

Stated that, the Off-Nadir model analysis has been specialized for the two above scenarios and a threshold value (for off-nadir angle) it is provided in order to distinguish the transition between the two operational sensing mode. Results obtained in implementing the models have been described in section 4 with reference to the Cassini Mission. Finally, section 5 summarises the main results of this study and reports conclusive considerations on the usage of propose altimeter waveform model.

REFERENCES

[1] Au, A.Y., Brown, R.D. and Welker, J.E. (1989). Analysis of altimetry over inland seas. NASA Tech. Memo., 100729.

[2] Birkett, C.M. (1994). Radar altimetry - A new concept in monitoring global lake level changes. Eos Trans. AGU, 75 (24), 273–275.

[3] Birkett, C.M. (1995). The contribution of TOPEX/POSEIDON to the global monitoring of climatically sensitive lakes. J. Geophys. Res., 100 (C12), 25, 179–25,204.

[4] Birkett, C.M. and Mason, I.M. (1995). A new Global Lakes Database for a remote sensing programme studying climatically sensitive large lakes. J. Great Lakes Research, 21 (3), 307–318.

[5] Birkett, C.M. (1998). Contribution of the TOPEX NASA radar altimeter to the global monitoring of large rivers and wetlands. Water Resources Research, 34 (5), 1223–1239.

[6] Birkett, C., Murtugudde, R. and Allan, T. (1999). Indian Ocean climate event brings floods to East Africa's lakes and the Sudd Marsh. GRL, 26 (8), 1031–1034.

[7] Birkett, C.M. (2000). Synergistic Remote Sensing of Lake Chad: Variability of Basin Inundation. Remote Sensing of the Environment, 72, 218–236.

[8] Birkett, C.M., Mertes, L.A.K., Dunne, T., Costa, M. and Jasinski, J. (2002). Altimetric remote sensing of the Amazon: Application of satellite radar altimetry. JGR, 107 (D20), 8059, 10.1029/2001JD000609.

[9] Brooks, R.L. (November 1982). Lake elevations from satellite radar altimetry from a validation area in Canada, report. Geosci. Res. Corp., Salisbury, Maryland, U.S.A.

[10] Campos, I. de O., Mercier, F., Maheu, C., Cochonneau, G., Kosuth, P., Blitzkow, D. and Cazenave, A. (2001). Temporal variations of river basin waters from Topex/Poseidon satellite altimetry: Application to the Amazon basin. Earth and Planetary Sciences, 333 (10), 633–643.

[11] Cazenave, A., Bonnefond, P., Dominh, K. and Schaeffer, P. (1997). Caspian sea level from Topex-Poseidon altimetry: Level now falling. Geophys. Res. Letters, 24 (8), 881–884.

[12] Chelton, D.B., Walsh, E.J. and MacArthur, J.L. (1988). ‘Nuts and Bolts’ of Satellite Radar Altimetry. Proceedings of the WOCE/NASA Altimeter Algorithm Workshop, Appendix to U.S. WOCE Technical Report No.2, Chelton, D.B. (Ed.), Corvallis Oregon, 1–43.

[13] Chelton, D.B., Ries, J.C., Haines, B.J., Fu, L.-L. and Callahan, P.S.

(2001). Satellite Altimetry, In Satellite Altimetry and the Earth Sciences: A Handbook of Techniques and Applications, Fu, L.-L. and Cazenave A. (Eds.), Academic Press, San Diego CA, 1–131.

[14] Cudlip, W., Ridley, J.K. and Rapley, C.G. (1992). The use of satellite radar altimetry for monitoring wetlands, Proceedings of the 16th Annual Conference of Remote Sensing Society: Remote Sensing and Global Change, London, UK, 207–216.

[15] Dalton, J.A. and Kite, G.W. (1995). A first look at using the TOPEX/Poseidon satellite radar altimeter for measuring lake levels. Proceedings of the International Workshop on the Application of Remote Sensing in Hydrology , Saskatoon, Canada, NHRI Symp. 0838-1984, No. 14, Kite, G.W., Pietroniro, A. and Pultz, T.D. (Eds.), 105–112.

[16] Guzkowska, M.A.J., Rapley, C.G., Ridley, J.K., Cudlip, W., Birkett, C.M. and Scott, R.F. (1990). Developments in inland water and land altimetry, ESA Contract, CR-7839/88/F/FL.

[17] Kite, G.W. and Pietroniro, A. (1996). Remote sensing applications in hydrological modeling. Hydrological Sciences Journal, 41 (4), 563–591.

[18] Koblinsky, C.J., Clarke, R.T, Brenner, A.C. and Frey, H. (1993). Measurement of river level variations with satellite altimetry. Water Resour. Res., 29 (6), 1839–1848.

[19] Maheu, C., Cazenave, A. and Mechoso, C.R. (2003). Water level fluctuations in the Plata Basin (South America) from Topex/Poseidon Satellite Altimetry. Geophys. Res. Letters, 30 (3), 1143–1146.

[20] Mercier, F., Cazenave, A. and Maheu, C. (2002). Interannual lake level fluctuations (1993-1999) in Africa from Topex/Poseidon: Connections with ocean-atmosphere interactions over the Indian Ocean. Global and Planetary Changes, 141–163.

[21] Mertes, L.A.K., Dekker, A.G., Brakenridge, G.R., Birkett, C.M. and Létourneau, G. (2003). Rivers and Lakes, in Natural Resources and Environment Manual of Remote Sensing, Vol. 5, Ustin, S.L. and Rencz, A. (Eds.), John Wiley & Sons: New York, In Press.

[22] Morris, C.S. and Gill, S.K. (1994a). Variation of Great Lakes water levels derived from Geosat altimetry. Water Resour. Res., 30 (4), 1009–1017.

[23] Morris, C.S. and Gill, S.K. (1994b). Evaluation of the TOPEX/POSEIDON altimeter system over the Great Lakes. J. Geophys. Res., 99 (C12), 24,527–24,539.

[24] Olliver, J.G. (1987). An analysis of results from SEASAT altimetry over land and lakes, paper presented at IAG Symposium, IUGG XIX General Assembly, Int. Assoc. of Geod., Vancouver.

[25] Ponchaut, F. and Cazenave, A. (1998). Continental lake level variations from TOPEX/POSEIDON (1993-1996). Earth and Planetary Sciences, 326, 13–20.

[26] Rapley, C. G., Guzkowska, M.A.J., Cudlip, W. and Mason, I.M. (1987). An exploratory study of inland water and land altimetry using Seasat data, ESA Rep. 6483/85/NL/BI, Eur. Space Agency, Neuilly, France.

[27] Sarch. M.T. and Birkett, C.M. (2000). Fishing and farming at Lake Chad: Responses to lake level fluctuations. The Geographical Journal, 166 (2), 156–172.

[28] Scott, R.F., et al. (1994). A comparison of the performance of the ice and ocean tracking modes of the ERS 1 radar altimeter over non-ocean surfaces. Geophys. Res. Lett. 21 (7), 553–556.

[29] Ulaby, F.T., Moore, R.K. and Fung, A.K. (1981). Microwave Remote Sensing Fundamentals and Radiometry. Microwave Remote Sensing Active and Passive, Vol.1, Simonett, D.S., (Ed.), Artech House, Boston, Mass.

2 SATELLITE ALTIMETRY

Altimeters are active microwave instruments for the accurate measurement of vertical distances (between the spacecraft and the altimeter footprint). The technology determines the two-way delay of the radar pulse echo from the Earth’s surface to a very high precision (to less than a nanosecond). The concept has also the capability to measure the power and the shape of the reflected radar pulses. In the following paragraphs satellite altimetry principles and technique are introduced.

2.1 Overview of the RA Missions

Since the first dedicated altimeter was launched on Seasat platform in 1978, satellite altimetry has lived an incredible and continuous development as long as new sensors were designed and became operational. The accuracy in range measurements gradually reached values that have allowed an extraordinary increase in our knowledge of many aspects of ocean and ice dynamics and variability. A summary of important characteristics for some past and future spaceborn altimeter missions is given in the following.

Mainly, the evolution of the altimeter transmitter is marked by improvements in pulse compression techniques that have substantially reduced peak power requirements. All the altimeter missions below introduced operate at Ku-Band. The choice of frequency is constrained by both the system and operational requirements. Since a narrow transmitted pulse is required to achieve a reasonable range precision, high frequency operation will support both the large receiver bandwidth and narrow antenna beamwidth requirements. The upper limit on the operational frequency is constrained by atmospheric attenuation effects that significantly degrade the performance of the altimeter for frequencies > 18GHz. In some altimetric missions, for instance Topex, the radar altimeter instrument includes C-Band transmitter so that ionispheric propagation delays can be accurately measured. Generally, the two-frequency system will produce a sub-decimeter range precision so that very small variations (particularly in ocean surface) can be detected.

- ERS

The first European satellite to carry a radar altimeter, ERS-1, was launched on 17 July 1991. This satellite was designed to have different orbital configurations. During the first few months, the Commissioning Phase, all instruments were calibrated and validated. Since then, ERS-1 has been flying two Ice Phases (in which the repeat period was 3 days), a Multi-Disciplinary Phase (a 35-day repeat orbit lasting from April 1992 till December 1994), and the Geodetic Phase, which started in April 1994 and had a repeat period of 168-days. The second repeat cycle in this Phase, till the launch of ERS-2, was shifted by 8 km with respect to the first, so a ``336-day repeat'' was obtained. ERS-2 was launched on 21 April 1995 and operated simultaneously to ERS-1, until ERS-1 was retired, in March 2000. Since their launch, ERS satellites have monitored the sea surface almost continuously. The accuracy of their altimeter range measurements has been estimated to be a little under 5 cm.

- TOPEX/Poseidon

TOPEX/Poseidon was launched in 1992 as joint venture between CNES and NASA. While a 3-year mission was initially planned, with a 5-year store of expendables, TOPEX/Poseidon is still flying, 9 years after its launch. Due to the low orbit inclination, data coverage is more limited respect to ERS data. However, TOPEX/Poseidon is equipped with two experimental altimeters, one French and one US-made, that reach an accuracy in sea surface height determination around 3 cm. Thanks to this high performance, for the first time, the seasonal cycle and other temporal variability of the ocean have been determined globally with high accuracy, yielding fundamentally important information on ocean circulation.

- Envisat

In November 2001, the European Space Agency launched Envisat, an advanced polar-orbiting Earth observation satellite which is still providing measurements of the atmosphere, ocean, land, and ice over a several year period. The Envisat satellite has been designed to ensure the continuity of the data measurements of the ESA ERS satellites. A radar altimeter (RA-2) will be mounted on Envisat. This instrument is derived from the ERS-1 and 2 Radar Altimeters, providing improved measurement performance and new capabilities determining the two-way delay of the radar echo from the Earth's surface to a very high precision, within 2.5 centimetres.

- Jason-1

Jason-1 is the first follow-on to TOPEX/Poseidon mission. It was launched in 2001 and provided highly accurate ocean altimetry data and near-real time altimetry data for predicting sea state and ocean circulation. Built by CNES, Jason is a lightweight altimeter based on the experimental secondary altimeter used by TOPEX/Poseidon. A second system at microwave has been used to measure the density of water vapour in the atmosphere, which allowed much more accurate atmospheric corrections. This system was able to measure sea surface height to within 2.5 centimetres.

- CRYOSAT 2

CryoSat1 was the first satellite to be realized in the framework of the Earth Explorer Opportunity Missions of ESA's Living Planet Programme. The mission concept has been selected in 1999 with an anticipated launch in 2004. Cryosat 1 and following Cryosat 2 it is radar altimetry mission dedicated to observations of the Polar Regions. The goal is to study possible climate variability and trends by determine variations in thickness of the Earth's continental ice sheets and marine sea ice cover. The CryoSat2 Mission makes use of a near polar Low Earth Orbit (LEO) non sun-synchronous at an altitude of ~ 720 km with an inclination of 92 degrees. The spacecraft accommodates the Altimeter SIRAL, DORIS receiver and Laser reflector.

In spite of the big progress done, big improvements can be achieved both for what concerns an increase in the range measurements accuracy, that could allow a more precise description of sea surface topography especially for regions where dynamic signals are not particularly strong (as the Mediterranean sea), or thinking of more reliable measurements near the coasts, and finally identifying sampling strategies that could allow a more synoptic and global coverage of the Earth surface which is fundamental for a precise monitoring of mesoscale currents.

2.2 Altimetry Principles and Techniques

The basic concept of satellite altimetry is deceptively straightforward. The principal objective is to measure the range *R* from the satellite to target surface. The altimeter transmits a short pulse of microwave radiation with pre-defined power toward the target surface. The pulse interacts with the rough surface and part of the incident radiation reflects back to the altimeter. The techniques for radar determination of the time *t* for the pulse to travel round trip between the satellite and surface are described in section 3. The range *R* from the satellite to surface is estimated from the round trip travel time by:

$$R = \hat{R} - \sum_j \Delta R_j \,, \qquad (1)$$

where $\hat{R} = {ct}/{2}$ is the range computed neglecting refraction based on free space speed of light c and ΔR_j, *j=1,....,N* are corrections for the various components of the atmospheric refraction and for biases between the mean electromagnetic scattering surface and mean reference target surface.

The range estimate (1) varies along the satellites orbit from along-track variations of both the surface topography (mainly sea-surface) and the orbit height relative to the centre of the Earth. For more accurate mission requirements, as oceanography, the range estimate must be transformed to a fixed coordinate system. As introduced in section 3, this is achieved by precision orbit determination of the height *H* of the satellite relative to a specified ellipsoid approximation of the geoid. The range measurements are then converted to the height *h* of the target surface relative to reference ellipsoid by:

$$R = H - \hat{R} = H - \hat{R} + \sum_j \Delta R_j \qquad (2)$$

It is worth noting that, accurate estimates of *R* and *H* are not sufficient for oceanographic applications of altimeter range measurements. The target-surface height given by (2), relative to the reference ellipsoid, it is the overlapping of a number geophysical effect. In addition to the dynamic effect of geostrophic ocean currents that are of primary interest for oceanographic applications (see Fu-Cazenave, 2001), *h* is affected by undulation of the geoid about the ellipsoidal approximation, tidal heights variations and ocean surface response to atmospheric pressure loading. These effects on the sea-surface height must be removed from h in order to investigate the effect of geostrophic ocean currents.

While complicating altimetric estimation of range *R*, the alteration of the incident radar pulse by a rough surface (sea, land, terrain, ice) can be utilized to extract other geophysical information from the radar return (see section 3.1.3).

A primary characteristic in design of an altimeter system is the area on the target surface over which the range from the altimeter to the reference surface height is measured. The footprint of an antenna is traditionally described in terms of the beam-limited footprint, defined to be the area on target surface within the field of view subtended by the beam width of the antenna gain pattern. For a narrow-beam antenna, the antenna beam-width can be expressed as:

$$\gamma = 2\tan^{-1}\left(\frac{r}{R}\right) \approx 2\frac{r}{R} \qquad (3)$$

where *r* is the footprint radius and *R* is the orbit range.

The limitation of the beam-limited altimeter design can be overcome by transmitting a very short pulse with duration of a few nanoseconds (pulse-limited configuration) from an antenna with a smaller diameter and correspondingly wider beamwidth. The qualitative difference between these two modes is that the illuminated area on the surface is determined by the antenna beamwidth or transmitted pulsewidth, respectively. In order to indicate which mode is being used, the geometry of the altimetry must be examined. Figure 1 shows a nadir oriented antenna operating above a mean surface from the altitude *h*. The antenna beamwidth is given as BW and the transmitted pulsewidth is PW. The diameter of the area of the circle on the surface that is within the beamwidth is:

$$d_B = 2h \tan \frac{BW}{2} \qquad (3.1)$$

Furthermore, the area of the circle formed by the intersection of the leading edge of the pulse with the mean surface when the trailing edge just intersects the surface at nadir point has a diameter given by:

$$d_P = 2\sqrt{(h + cPW)^2 - h^2} \qquad (3.2)$$

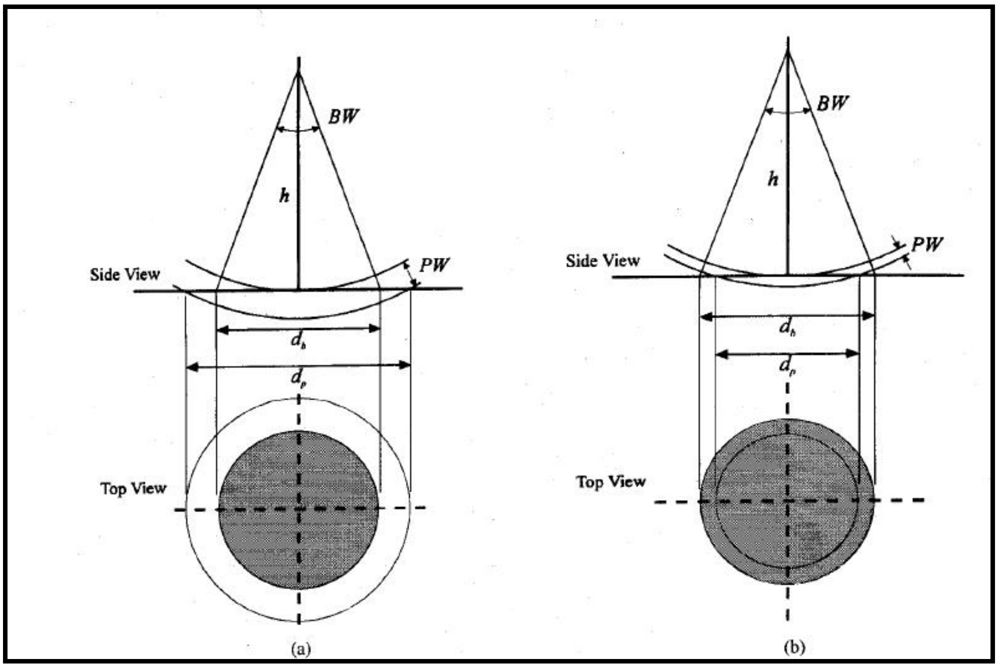

Figure 1 –Geometry of a nadir oriented (a) beamwidth-limited altimeter (dP>dB) and (b) pulsewidth-limited altimeter (dP<dB)

A diagram of the altimeter pulse interaction with a quasi-flat surface is shown in Figure 2. As the incident pulse strikes the surface, it illuminates a circular region that increases linearly with time. Correspondingly, a linear increase in the leading edge of the return waveform occurs. After the trailing edge of the pulse has intersected the surface, the region back-scattering energy to the satellite becomes an expanding annulus of constant area. At this point, the return waveform has reached its peak and then begins to trail off due to the reduction of the off-nadir scattering by the altimeter's antenna pattern. For a rough surface as rough ocean surface, the leading edge of the return pulse will be "stretched" because scattering from wave crests (or rough-peaks more generally) precedes the scattering from the wave troughs as the pulse wavefront progresses downward. Thus, the width of the leading edge of the return pulse can be related the level of the target surface roughness.

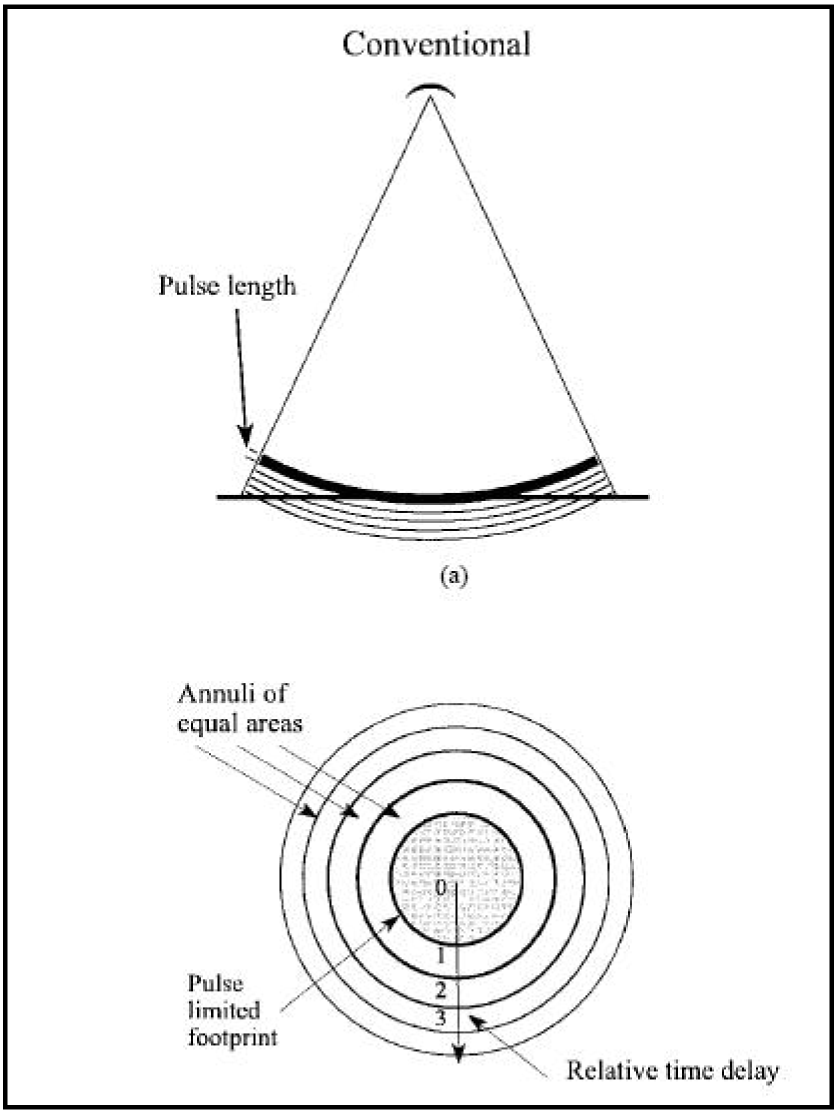

Figure 2 –Conventional Pulse Limited illumination geometry

2.2.1 Off-Nadir Altimeter Technique

Conventional altimeter provides a surface topography profile along the flight line. In most cases, the scientific requirement is to acquire surface topography over two-dimensional surface. A first intuitive solution to the problem of spatial and temporal sampling for the ocean or land observations is represented by the modification of the conventional Pulse Limited radar altimeter concept by extending its limited, although high performing, nadir looking measurement capability with the inclusion of off-nadir measurements taken from additional antenna beams pointed off-nadir. The individual beam's footprints should be spaced in the horizontal plane to achieve the swath widths needed for various scientific applications. The extent of the footprints is determined by the beam forming antenna system. Figure 3 shows the geometry of the acquisition for this kind of system.

The individual beam's footprints should be spaced in the horizontal plane to achieve the swath widths needed for various scientific applications. The extent of the footprints is determined by the beam forming antenna system. The addition of off-nadir beams creates a remarkable increase in the number of intersections (crossovers) between ascending and descending tracks.

The instantaneous surface footprint of a real aperture imaging altimeter usually defines the superficial resolutions X_r and X_a in the cross track and along track dimensions, respectively. The height resolution (ΔH) depends on the surface slope, illumination geometry, and sensor characteristic.

Being ξ the off-nadir angle, the echo will be spread as a result of the oblique geometry as shown in Figure 4 and expressed by the following relation:

$$\Delta H = \frac{H\theta_B \tan(\xi)}{\cos(\xi)} \qquad (4)$$

where θ_B is the angle between the half power points of the main beam. This causes an echo spread that leads to a decrease in the total height measurement accuracy. This effect can be reduced by analysing the total echo shape instead of measuring the time of arrival of the leading edge, but this implies an accurate satellite attitude control system. A possible solution to the attitude estimation problem is to model the expected return waveforms for a range of off-nadir angles and compare them to the measured return. This method requires huge data storage and, inevitably, long processing times.

Another possibility is to analyse the modelled returns and develop an algorithm that is able to indicate the pointing angle when applied to the measured returns. This has the potential of reducing the processing time, but in either case, it is necessary to model the expected or average return waveforms.

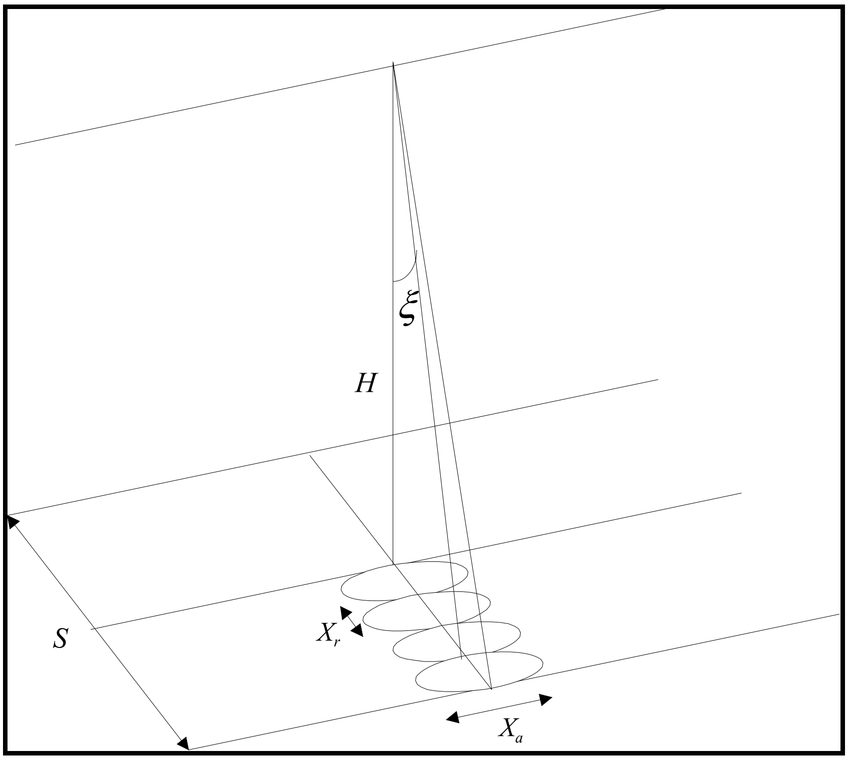

Figure 3 – Geometry for scanning off-nadir radar altimeter

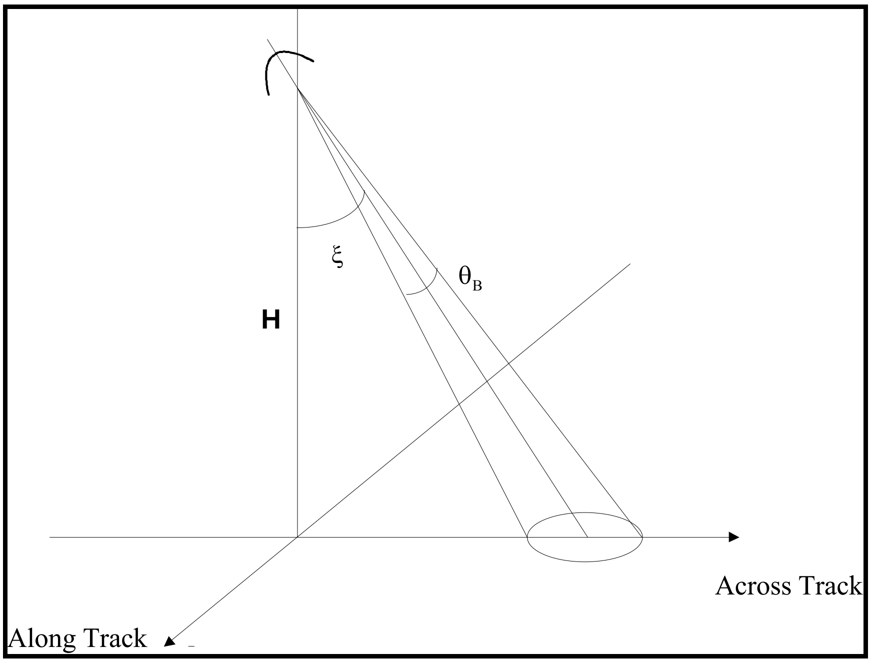

Figure 4 – Across track geometry

2.2.2 RA Spatial Resolution

Starting with the assumption of having a circularly symmetric Gaussian antenna pattern given by the following equation:

$$G(\theta,\omega) = G_0 \exp\left(-\frac{2}{\gamma}\left(1+\beta\cdot\sin^2\omega\right)\sin^2\theta\right) \quad (5)$$

the relations for evaluating the along-track (ρ_{AT}) and cross-track (ρ_{CT}) spatial resolutions achievable by the system are straightforward:

$$\rho_{CT} = h\left[\tan\left(\xi+\frac{\theta_{CSB}}{2}\right)-\tan\left(\xi-\frac{\theta_{CSB}}{2}\right)\right] \qquad (6)$$

$$\rho_{AT} = 2\frac{h}{\cos\xi}\tan\left(\frac{\theta_B}{2}\right) \qquad (7)$$

$$\theta_B = \theta_{CSB} \approx 1.47\frac{\lambda}{D} \qquad (8)$$

Figure 5 and Figure 6 show the results obtained by applying the previous two equations and by varying the values of spacecraft altitude and antenna beamwidths.

The situation can be made clearer if a specific goal for the spatial resolution is fixed and, for example, the spacecraft altitude is plotted as a function of the off-nadir angle for various beamwidth values. This is done in Figure 7 where a goal of 5 Km has been considered.

If the mean values are taken with respect the off-nadir angle (as shown in Figure 7, the spacecraft altitude is almost constant with respect the off-nadir angle, within the considered interval), the results shown in the following Table 1 can be derived.

In addition, to have an estimate of the antenna size (D) to be used, the following relation can be considered where a 56% efficient circular aperture has been considered [15, 16, and 21]. A plot of the achievable antenna aperture as a function of the frequency of operation and antenna size is shown in Figure 8.

Off-nadir angle [deg]	From 0 to 15							
Antenna beamwidth [deg]	0.35	0.40	0.45	0.5	0.55	0.6	0.65	0.7
Cross-track resolution [Km]	5							
Spacecraft altitude [Km]	800	700	622	560	509	467	431	400
Along-track resolution [Km]	5							
Spacecraft altitude [Km]	809	708	629	566	515	472	436	405

Table 1– Mean values of spacecraft altitude with respect the off-nadir angle for achieving a spatial resolution of 5 Km.

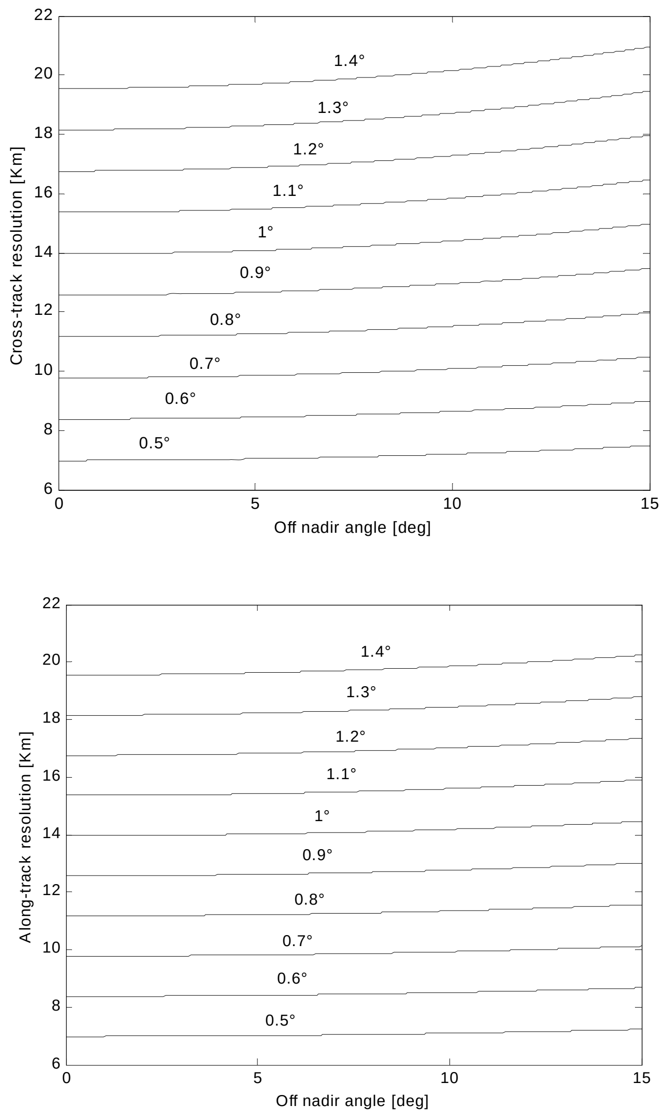

Figure 5 – Along-track and cross-track spatial resolutions as a function of the off-nadir angle for various values of antenna beamwidths (h=800 Km)

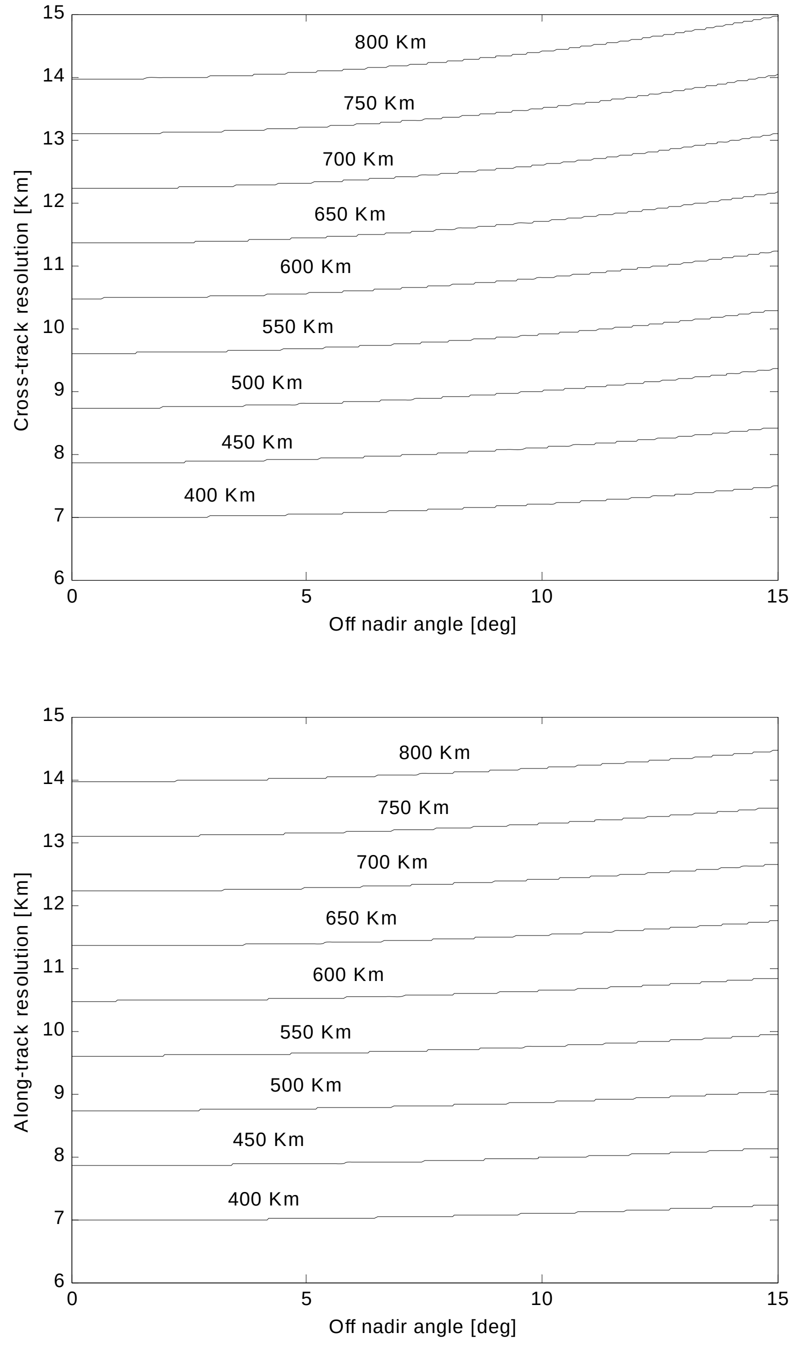

Figure 6 – Along-track and cross-track spatial resolutions as a function of the off-nadir angle for various values of spacecraft altitude (Antenna beamwidth of 1 deg)

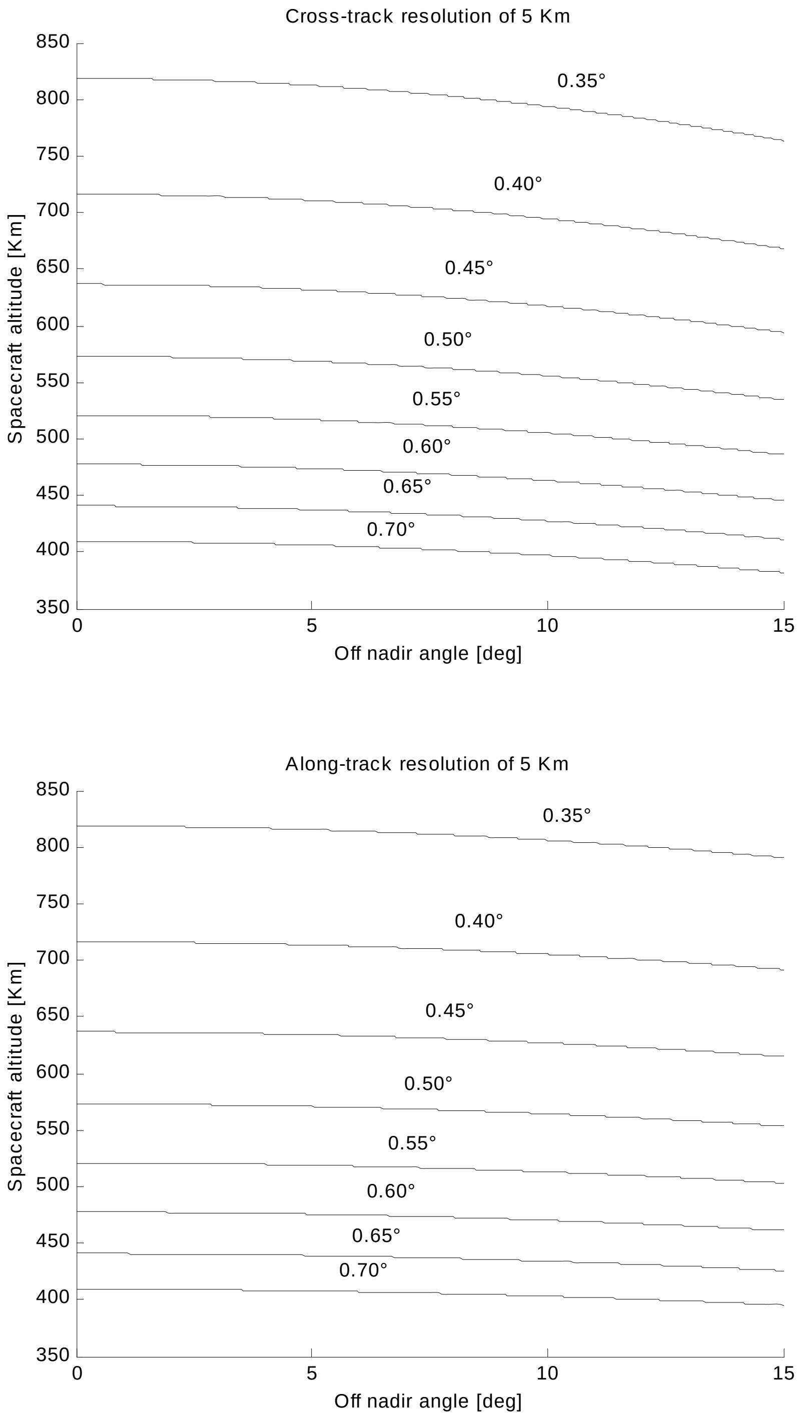

Figure 7 – Spacecraft altitude as a function of the off-nadir angle for various beamwidth values with a fixed spatial resolution of 5 Km.

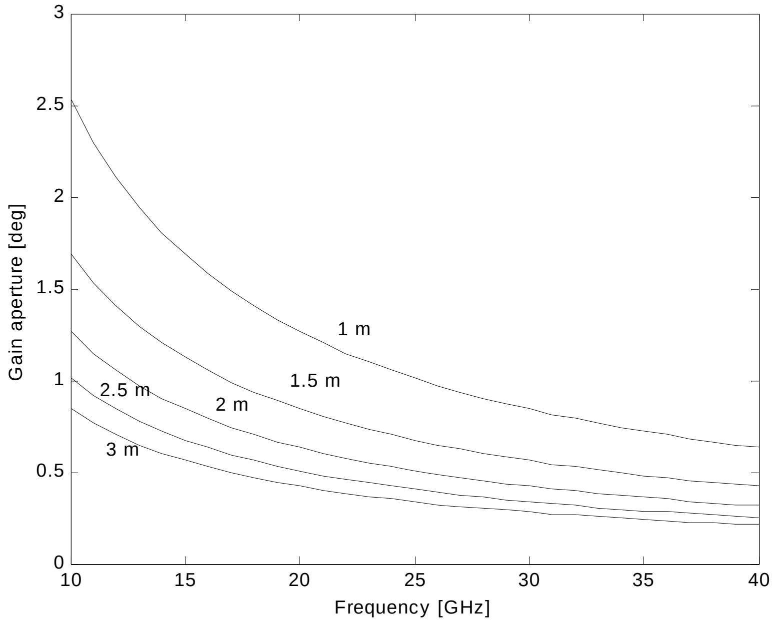

Figure 8 – Gain antenna aperture as a function of the transmitted frequency for various antenna diameters

2.2.3 RA Accuracy

The attainable accuracy that can be interpreted as rms height error is strongly dependent on the implemented estimation algorithm. In the following, a theoretical estimate of the rms height error for a split-gate tracker is derived, on the basis of receiver model shown in Figure 9.

The received signal, before the square-law detection, is a zero-mean narrow-band Gaussian process. The variance of the signal σ_s^2 is, within a scaling factor, the averaged waveform $P_r(\tau)$. By considering an additive noise with a variance σ_n^2, the signal entering the square-law detector has a total variance of $\sigma_s^2 + \sigma_n^2$ and a two-sided bandwidth of $2/T_p$, being T_p the transmitted signal compressed pulse length. T_e is the time spread of $P_r(\tau)$ between 1/e points. Therefore the following waveform model can be used:

$$P_r(\tau) = \exp\left(-\frac{\tau^2}{2(T_e/2)^2}\right) \qquad (9)$$

As discussed in [16], after the square-law detector the signal is Gaussian distributed with a variance:

$$\sigma_y^2 = a^2\left(\sigma_s^2 + \sigma_n^2\right) \qquad (10)$$

where a is the detection scale factor. The last expression can be written as a function of the peak signal-to-noise ratio (SNR) as:

$$\sigma_y = a\ \sigma_s^2 \sqrt{1 + \frac{2}{SNR} + \frac{1}{SNR^2}} \qquad (11)$$

Replacing $a\ \sigma_s^2$ by the range spread function and considering the averaging properties of the postdetection and signal-averaging filter, it is possible to obtain:

$$\sigma_y = \frac{P_r(\tau)}{2}\sqrt{\frac{T_p}{T_e}\left(1 + \frac{2}{SNR} + \frac{1}{SNR^2}\right)} \qquad (12)$$

The factor 1/2 arises from replacing the idealised zonal filter with a realisable filter. By assuming a split-gate tracker that tracks the waveform at $1/\sqrt{e}$, the slope at this point is:

$$\frac{\Delta\tau}{\Delta P_r} = \frac{T_e}{2}\sqrt{e} \qquad (13)$$

The uncertainty in time unit is therefore given by:

$$\sigma_\tau = \frac{\Delta\tau}{\Delta P_r}\sigma_y = \frac{1}{4}\sqrt{T_p T_e\left(1 + \frac{2}{SNR} + \frac{1}{SNR^2}\right)} \qquad (14)$$

Finally, by considering the averaging of a number of statistically independent return waveform over a time period T_A, the range uncertainty is:

$$\sigma_h = \frac{c}{8}\sqrt{\frac{T_p T_e}{PRF \cdot T_A}\left(1 + \frac{2}{SNR} + \frac{1}{SNR^2}\right)} \qquad (15)$$

The pulse repetition frequency of the system (PRF) is limited by the minimum distance (L_d) necessary for the radar to travel for decorrelation, that can be evaluated from the Van Cittert-Zernike theorem (see appendix A2) as modified in [18] to account for the two-way condition.

$$L_d = 0.6\frac{\lambda}{\theta_B} \qquad (16)$$

Therefore, the minimum value for the rms height uncertainty becomes:

$$\sigma_h = \frac{c}{8}\sqrt{0.6\frac{\lambda T_p T_e}{V_s \theta_B T_A}\left(1+\frac{2}{SNR}+\frac{1}{SNR^2}\right)} \qquad (17)$$

where V_s is the spacecraft velocity. From the last relation it is evident that, for improving the accuracy of the radar, would need to increase the antenna aperture at the expenses of the spatial resolution. In addition also the distance travel by the satellite within the integration time T_A should be maintained much less than the accuracy, if the along-track spatial resolution should remain as given by the (7). If this is not the case, the overall along-track spatial resolution can be modelled by assuming both the antenna spatial-filtering effect and averaging over the interval T_A processes to be Gaussian.

Therefore, the one-sigma width of the resulting composite spatial-averaging process is:

$$\rho = \sqrt{(V_s T_A)^2 + \rho_{AT}^2} \qquad (18)$$

In the following two cases-study of achievable accuracy are given based on two different values of along-track aperture: 1 and 0.5 degrees. The first values can be representative of a Ku system (13.5 GHz), while the second values can be reached by using a Ka band radar (36 GHz). The following assumption have been made:

1. the PRF has been set to the maximum value allowed by the Van Cittert-Zernike theorem for assuring a decorrelation among pulses;
2. off-nadir angles ranging from 1 to 10 degrees;
3. for each off-nadir angle the relative IR has been evaluated and the corresponding width T_e between 1/e points measured;
4. a transmitted bandwidth of 320 MHz has been considered implying a time resolution T_p of 3.125 ns;

5. the integration time has been set to the maximum value allowed by the (18) for assuring a specific along-track resolution value;
6. three satellite altitude values have been considered: 400, 600 and 800 Km;
7. two goals for the along-track spatial resolution have been considered: 5 and 10 Km.

With 10 Km of along-track resolution and an antenna aperture of 1 degree only a configuration is possible, that with the satellite flying at 400 km of altitude. The resulting accuracy values as a function of the off-nadir angles and signal to noise ratio are shown in Figure 10.

If the antenna beamwidth is improved up to 0.5 degrees also the configuration at 600 Km is feasible and the relative results are shown in Figure 11 and Figure 12.

With 5 Km of along-track resolution only the configuration with 0.5 degrees of antenna aperture and the satellite altitude of 400 Km is feasible and the results are shown in Figure 13.

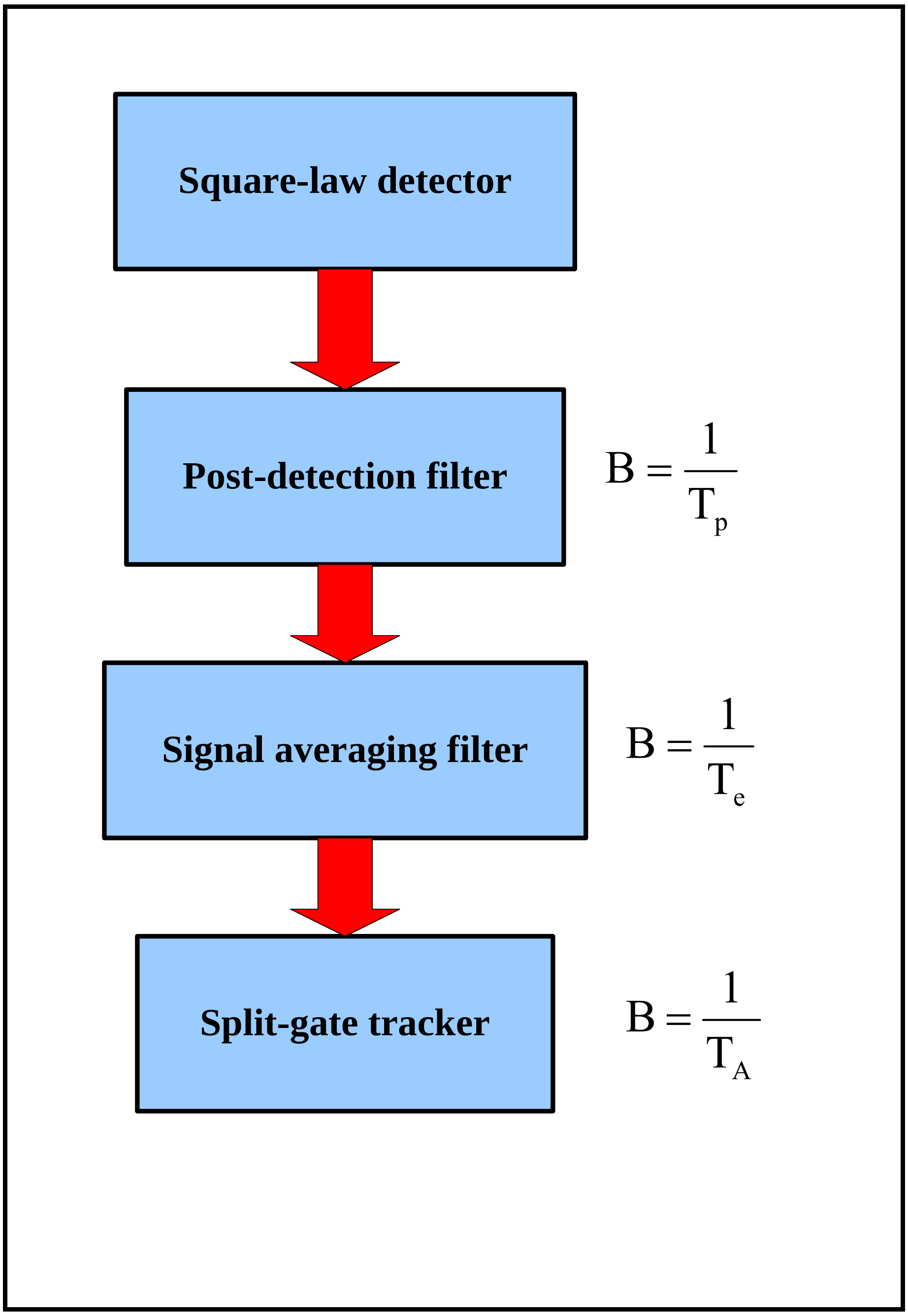

Figure 9 – Receiver model used for the estimation of rms height error

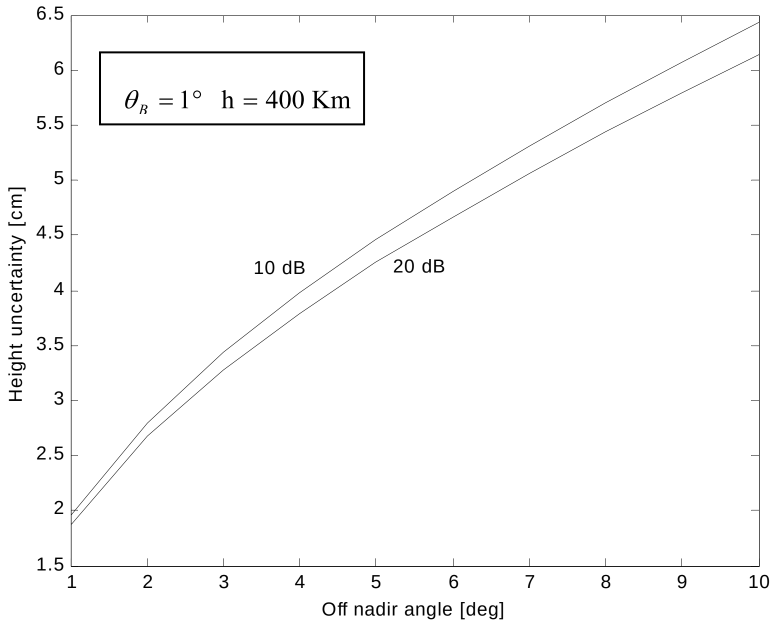

Figure 10 – Achievable height uncertainty as a function of the off-nadir angle and signal to noise ratio for assuring 10 Km of along-track resolution

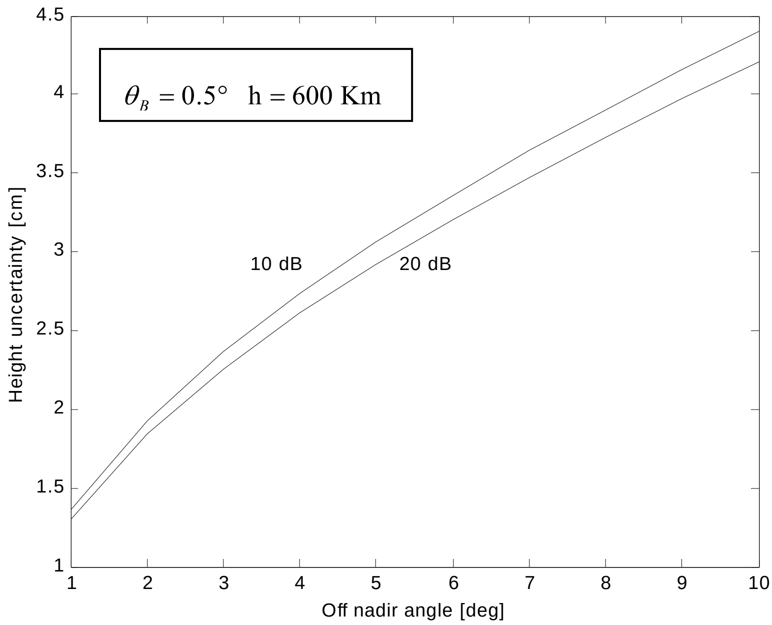

Figure 11 – Achievable height uncertainty as a function of the off-nadir angle and signal to noise ratio for assuring 10 Km of along-track resolution

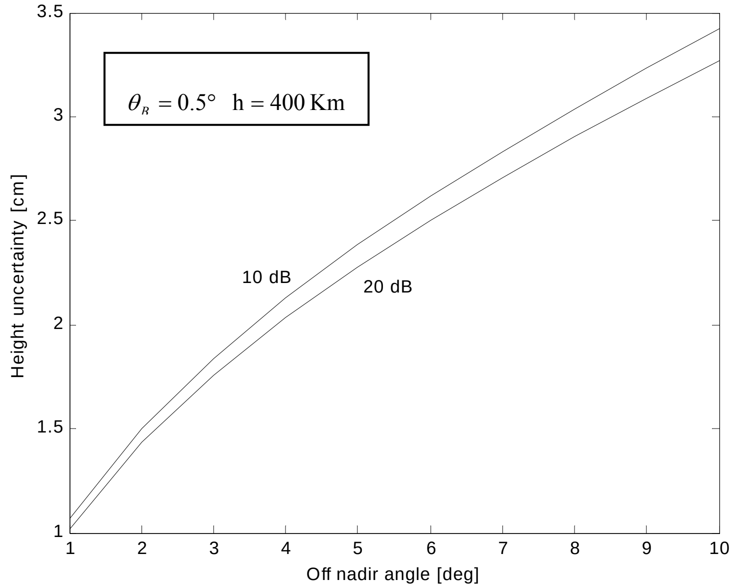

Figure 12 – Achievable height uncertainty as a function of the off-nadir angle and signal to noise ratio for assuring 10 Km of along-track resolution

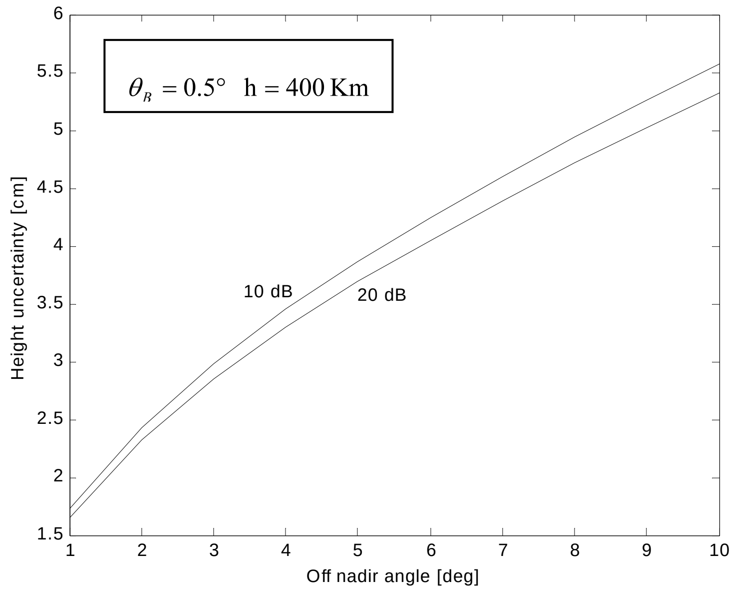

Figure 13 – Achievable height uncertainty as a function of the off-nadir angle and signal to noise ratio for assuring 5 Km of along-track resolution

REFERENCES

[1] Douglas, B.C., D.C. McAdoo, and R.E. Cheney, Oceanographic and geophysical applications of satellite altimetry, Rev. Geophys., 25, 875--880, 1987.

[2] Wunsch, C., and E.M. Goposchkin, On using satellite altimetry to determine the general circulation of the ocean with application to geoid improvements, Rev. Geophys., 18, 725-745, 1980

[3] Stammer D., 1997: Steric and wind-induced changes in TOPEX/POSEIDON large-scale sea surface topography, J. Geophys. Res., 102, C9, 20987-21011.

[4] Vivier F., K.A. Kelly and L. Thompson, 1999: Contributions of wind forcing, waves, and surface heating to sea surface height observations in the Pacific Ocean, J. Geophys. Res., 104, C9, 20767-20788.

[5] Wang L. and C. Koblinsky, 1997: Can the Topex/Poseidon altimetry data be used to estimate air-sea heat flux in the North Atlantic?, Geophys., Res. Lett., 24, NO.2, 139-142.

[6] Behringer, D.W., Sea surface height variations in the Atlantic Ocean: A comparison of TOPEX altimeter data with results from an ocean data assimilation system, J. Geophys. Res., 99, 24685--24690, 1994.

[7] Bhaskaran, S., G. S. E. Lagerloef, G. H. Born, W. J. Emery, R. R. Leben, Variability in the gulf of Alaska from Geosat altimetry data, J. Geophys. Res., 89(C9), 16330-16345, 1993.

[8] Blaha, J. and B. Lunde, Calibrating Altimetry to Geopotential Anomaly and Isotherm Depths in the Western North Atlantic, J. Geophys. Res., 97(C5), 7465--7478, 1992.

[9] Chambers D.P., B.D. Tapley and R.H. Stewart, 1997: Long-period ocean heat storage rates and basin-scale heat fluxes from TOPEX, J. Geophys. Res.,102, C12, 163-177.

[10] Cipollini P., D. Cromwell, P. G. Challenor and S Raffaglio, Rossby waves detected in global ocean colour data, Geophysical Research Letters, Vol. 28 , No. 2, pp. 323-326, 2001.

[11] Cipollini P., D. Cromwell, G. D. Quartly, Observations of Rossby wave propagation in the Northeast Atlantic with TOPEX/POSEIDON altimetry, Advances in Space Research, Vol. 22, No. 11, pp. 1553-1556, 1999.

[12] Cipollini P., D. Cromwell, M. S. Jones, G. D. Quartly, P. G. Challenor, Concurrent altimeter and infrared observations of Rossby wave propagation near 34° N in the Northeast Atlantic, Geophysical Research Letters, Vol. 24, No. 8 , pp. 889-892, 1997.

[13] Kelly, K.A., M.J. Caruso and J.A. Austin, Wind-forced variations in sea surface height in the Northeast Pacific Ocean, J. Phys. Oceanogr.,

23, 2392-- 2411, 1993.

[14] Nerem, R.S., B.D. Tapley and C.-K. Shum, Determination of the Ocean Circulation using Geosat Altimetry, J. Geophys. Res., 95(C3), 3163--3180, 1990.

[15] Challenor, P. G. and R. T. Tokmakian, 1999: Altimeter measurements of the volume transport through the Drake Passage. Advances in Space Research, 22(11), 1549-1552.

[16] Gaspar, P. and C. Wunsch, Estimates from Altimeter Data of Barotropic Rossby Waves in the rthwestern Atlantic Ocean, J. Phys. Oceanogr,. 19(12), 1821--1844, 1989.

[17] Koblinsky, C.J., R.S. Nerem, R.G. Williamson and S.M. Klosko, Global scale variations in sea surface topography determined from satellite altimetry, in Sea Level Changes: Determination and Effects, Geophysical Monograph Vol. 69, IUGG Vol. 11, pp. 155--165, American Geophysical Union, Washington, D.C., 1992.

[18] Le Traon, P. Y. and P. Gauzelin, 1997: Response of the Mediterranean mean sea level to atmospheric pressure forcing, J. Geophys. Res., 973-983.

[19] Leuliette E.W. and J.M. Wahr, 1999: Coupled pattern analysis of sea surface temperature and TOPEX/POSEIDON sea surface height, J. Phys. Ocean., 29, 599-611.

[20] Tapley, B.D., D.P. Chambers, C.K. Shum, R.J. Eanes, J.C. Ries, and R.H. Stewart, Accuracy assessment of the large-scale dynamic topography from TOPEX/POSEIDON altimetry, J. Geophys. Res., 99, 24605--24617, 1994.

[21] Tokmakian R. T. and P. G. Challenor, Observations in the Canary Basin and the Azores Frontal Region Using Geosat Data, Journal of Geophysical Research-Oceans, 98(C3), 4761-4773, 1993.

[22] Aoki S., Imawaki S., Ichikawa K., 1995. Baroclinic disturbances propagating westward in the Kuroshio Extension region as seen by a satellite altimeter and radiometers. J. Geophys. Res., 100, 839-855.

[23] Buongiorno Nardelli B., R. Santoleri, S. Marullo, D. Iudicone and S. Zoffoli, 1999: Altimetric signal and three dimensional structure of the sea in the channel of Sicily, J. Geophys. Res., 104, C9, 20585-20603.

[24] Fu, L.-L., Recent progress in the application of satellite altimetry to observing the mesoscale variability and general circulation of the oceans, Rev. Geophys. Space Phys., 21, 1657--1666, 1983.

[25] Iudicone, D., S. Marullo, R. Santoleri, and P. Gerosa, 1998: Sea level variability and surface eddy statistics in the Mediterranean sea from TOPEX/POSEIDON data, J. Geophys. Res., 103, 2995-3012.

[26] Joyce, T.M., K.A. Kelly, D.M. Schubert and M.J. Caruso, Shipboard and Altimetric Studies of Rapid gulf Stream Variability Between Cape Cod and Bermuda, Deep-Sea Res., 37, 897--910, 1990.

[27] Larnicol, G., P.Y. Le Traon, N. Ayoub and P. De Mey, 1995: Mean sea level and surface circulation variability of the Mediterranean Sea from 2 years of TOPEX/POSEIDON altimetry, J. Geophys. Res., 100, C12, 163-177.

[28] Larnicol, G., N. Ayoub and P.Y. Le Traon, 2001:Majors changes in the Mediterranean Sea level variability from seven years of Topex/Poseïdon and Ers-1/2 data, submitted to Jour Mar. Sys.

[29] Matthews, P.E., M.A. Johnson and J.J. O'Brien, Observations of Mesoscale Ocean Features in the Northeast Pacific using Geosat Radar Altimetry, J.Geophys. Res., 97(C11), 17829--17840, 1992.

[30] Morrow, R., R. Coleman, J. Church, and D. Chelton, Surface eddy momentum flux and velocity variances in the Southern Ocean from Geosat altimetry, J. Phys. Oceanogr., 24, 10, 2050-2071, 1994.

[31] Wilkin, J., and R. A. Morrow, Eddy kinetic energy and momentum flux in the Southern Ocean: Comparison of a global eddy-resolving model with altimeter, drifter and current-meter data, J. Geophys. Res., 99(C4), 7903-7916, 1994.

[32] Arnault, S. and R.E. Cheney, Tropical Atlantic sea level variability from Geosat (1985--1989), J. Geophys. Res., 99, 18207--18223, 1994.

[33] Arnault, S., Y. Menard and J. Merle, Observing the Tropical Atlantic Ocean in 1986--1987 from Altimetry, J. Geophys. Res., 95(C10), 17921—17945 ,1990.

[34] Carton, J.A., Estimates of Sea Level in the Tropical Atlantic Ocean Using Geosat Altimetry, J. Geophys. Res., 94(C6), 8029--8039, 1989.

[35] Cheney, R.E. and L. Miller, Mapping the 1986--1987 El Niño with Geosat Altimeter data, EOS Trans. AGU, 69(31), 754--755, 1988.

[36] Lillibridge. J.L., R.E. Cheney and N.S. Doyle, The 1991--93 Los Niñ–os from ERS-1 altimetry, Proceedings Second ERS-1 Symposium, pp. 495--499, Hamburg, Germany, 1993.

[37] Egbert, G., A. Bennett and M. Foreman, Topex/Poseidon Tides, J. Geophys. Res., 99, 24821--24852, 1994.

[38] Andersen, O. B., and P. Knudsen: Multi-satellite Ocean tide modelling – the K1 constituent. In Tidal science, Eds R. Ray and P. L. Woodworth, Progress in Oceanography, Vol. 40 No 1-4, 197-216, 1997.

[39] Knudsen, P.: Separation of Residual Ocean Tide Signals in a Collinear Analysis of Geosat Altimetry. Bulletin Geodesique, Vol. 68, No. 1, 7-18, 1994.

3 RADAR ALTIMETER WAVEFORM MODELS

3.1 RA Nadir Looking

Starting from the same hypotheses made by Brown [5], but using a different approach, an analytical model of the average altimeter echo waveform is derived in the following paragraphs, in order to take into account the operative conditions of the Cassini Radar Altimeter imposed by observation geometry and radar parameters.

3.1.1 Nadir FSIR Evaluation

For a nadir pointing radar altimeter, i.e. off-nadir pointing angle $\xi = 0$, an exact closed-form expression for the flat surface impulse response (FSIR) is available in term of the two-way incremental ranging time, i.e. $\tau = t - 2h/c$, instead of absolute time, under the following general assumptions [5]:

1) the scattering surface may be considered to comprise a sufficiently large number of random independent scattering elements
2) the nature of the scattering mechanism is completely *noncoherent*
3) the surface height statistics are assumed to be constant over the total area illuminated by the radar during construction of the mean return
4) the specular points are gaussian distributed
5) the scattering is a scalar process with no polarization effects and is frequency independent
6) the variation of the scattering process with angle of incidence (relative to the normal to the mean surface) is only dependent upon the backscattering cross section per unit scattering area, σ^0, and the antenna pattern
7) the total Doppler frequency spread ($4V_r / \lambda$) due to a radial velocity between the radar and any scattering element on the illuminated surface, is small relative to the frequency spread of the envelope of

the transmitted pulse ($2/T$, where T is the 3 dB width of the transmitted pulse)

8) the antenna beam is considered circularly symmetric with gaussian approximation to the antenna gain, i.e., $G(\theta) \approx G_0 \exp(-(2/\gamma)\sin^2\theta)$
9) for the heights and ranging times of interest $c\tau/h << 1$.

Thus, the average backscattered power from a mean flat surface (illuminated by an impulse) which has a very small scale of roughness, but is characterized by the same backscattering cross section per unit scattering area as the true surface, has the following closed form solution for nadir evaluation:

$$P_{FS}(\tau) = K_{FS}\exp(-\alpha\tau) \qquad (19)$$

where $K_{FS} = \dfrac{G_0^2\lambda^2 c\sigma^0(\psi_0)}{4(4\pi)^2 L_p h^3}$ $,\alpha = \dfrac{4c}{\gamma h}$, $\gamma = -\dfrac{2\sin^2(\theta_{3dB}/2)}{\ln(1/2)}$.

Here G_0 is the peak antenna gain (at boresight), c is the speed of light, λ is the radar carrier wavelength, L_p is the two-way path loss, and h is the spacecraft altitude above the mean flat surface.

The geometry of a radar altimeter system, useful for the FSIR evaluation, is given in .

We note, according to [5], that the radar cross-section $\sigma^0(\psi,\phi)$ is taken to be ϕ-independent, because of the small pulsewidths and narrow antenna beamwidths. That is, the effective illuminated area covers such a small angular spread that σ^0 may be considered to be nearly constant.

An example of nadir pointing FSIR evaluation for the Cassini Radar Altimeter with varying spacecraft altitude is given in Figure 15.

The width of each waveform sampling gate is 30 m, corresponding to the vertical resolution of the Hi-Res Altimeter (ALT) of the Cassini Radar, which is given by $c/(2f_c) \approx 30$ m, where f_c is the sampling frequency.

In the following, t_0 is the reference time, i.e. the instant at which the first echo from the surface within the radar footprint is expected to arrive. Therefore, all the functions will be centred around this value, which at first attempt is settled to be 500 if expressed in range bins ($t_0 \cdot f_c$), as results from LBDR echo data.

The main parameters used in doing these calculations are reported in Table 2.

Frequency	13.78 GHz
Antenna beamwidth (θ_{3dB})	0.350 deg
Sampling frequency (f_c)	5 MHz
Chirp length	150 μs
Chirp bandwidth (B)	4.25 MHz
Pointing angle (ξ)	0 deg

Table 2 – Main parameters for the Hi-Res Altimeter (ALT) of the Cassini Radar

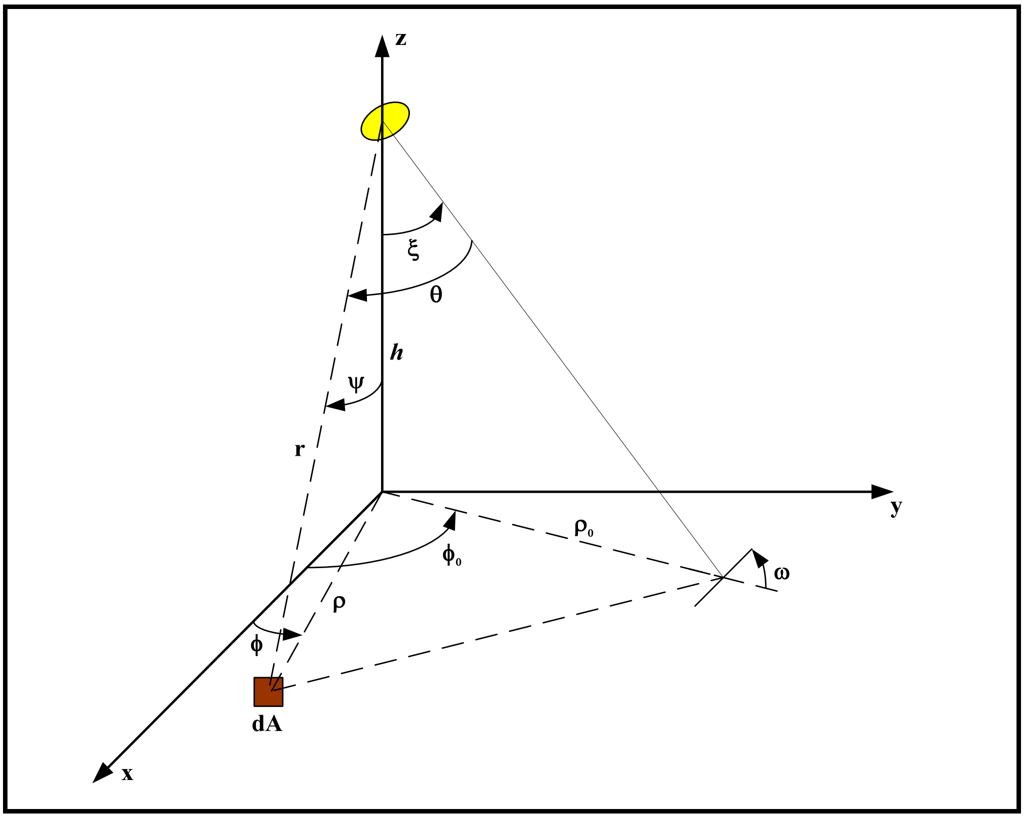

Figure 14 – Geometry for flat-surface impulse response evaluation

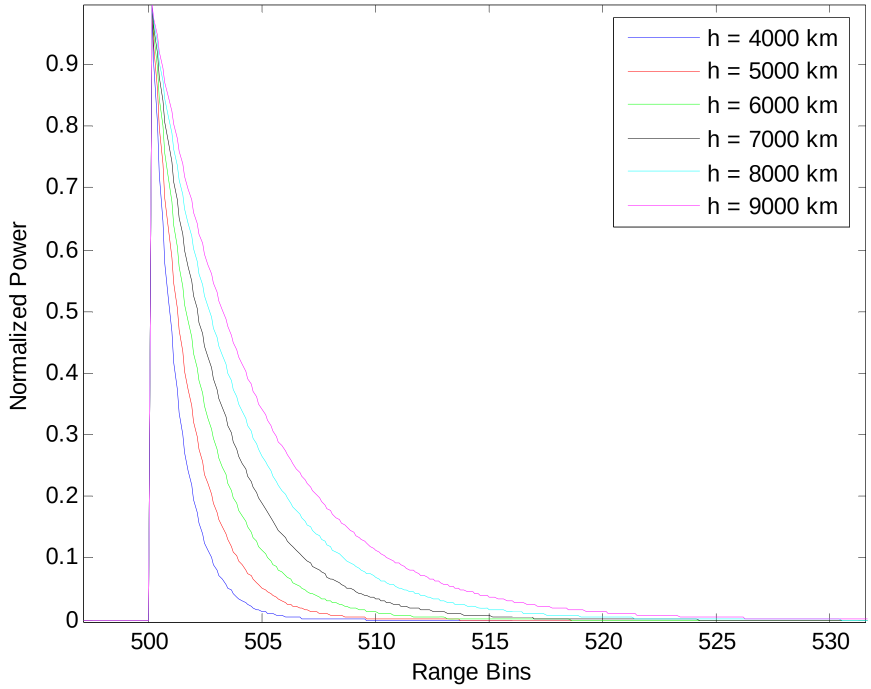

Figure 15 – Nadir pointing FSIR with varying spacecraft altitude

3.1.2 Nadir IR Evaluation

The system impulse response can be evaluated, as done in [3], by the convolution of the FSIR with the height probability density function $P_h(\tau)$ and the system point target response $P_P(\tau)$, i.e.,

$$IR(\tau) = P_{FS}(\tau) * P_h(\tau) * P_p(\tau) \quad (20)$$

These two functions are supposed to be gaussian, and are given by the following expressions:

$$P_h(\tau) = \frac{1}{\sqrt{2\pi}\sigma_h} \frac{c}{2} \exp\left(-\frac{\tau^2}{2\sigma_h^2} \frac{c^2}{4}\right) \qquad (21)$$

$$P_p(\tau) = \frac{P_T T}{\sqrt{2\pi}\sigma_p} \exp\left(-\frac{\tau^2}{2\sigma_p^2}\right) (22)$$

where σ_h is the rms height of the specular points relative to the mean surface level, P_T is the peak transmitted power, and σ_p is related to the 3 dB width of the transmitted pulse by the following relation:

$$\sigma_p = \frac{T}{\sqrt{8\ln 2}}$$

The convolution between $P_h(\tau)$ and $P_p(\tau)$ can be written as:

$$P_{HI}(\tau) = K_{HI}\exp\left(-a\tau^2\right) \qquad (23)$$

where $K_{HI} = P_T\eta\sqrt{2\pi}\dfrac{\sigma_p}{\sigma_C}$, $a = \dfrac{1}{2\sigma_C^2}$, $\sigma_C^2 = \sigma_S^2 + \sigma_p^2$, $\sigma_S = \dfrac{2}{c}\sigma_h$, $\eta = BT$.

Here, the parameter σ_C is the total spreading of the average echo [5], which accounts for the surface roughness $\sigma_h 2/c$.
Hence, the system impulse response (20) is given by:

$$\begin{aligned} P_{FS}(\tau) * P_{HI}(\tau) &= K_{FS}K_{HI}\exp\left(-\alpha\tau\right) * \exp\left(-a\tau^2\right) = \\ &= K_{FS}K_{HI}\int_0^\infty \exp\left(-\alpha\overline{\tau}\right)\exp\left[-a\left(\tau-\overline{\tau}\right)^2\right]d\overline{\tau} = \qquad (24) \\ &= K_{FS}K_{HI}\exp\left(-a\tau^2\right)\int_0^\infty \exp\left(-2b\overline{\tau}\right)\exp\left(-a\overline{\tau}^2\right)d\overline{\tau} \end{aligned}$$

where $2b = \alpha - 2a\tau$.
By using the Abramowitz and Stegum integration method [6], we have that:

$$\int_0^\infty \exp\left(-2b\overline{\tau}\right)\exp\left(-a\overline{\tau}^2\right)d\overline{\tau} = \frac{1}{2}\sqrt{\frac{\pi}{a}}\exp\left(\frac{b^2}{a}\right)erfc\left(\frac{b}{\sqrt{a}}\right) \qquad (25)$$

which can be substituted in the expression (24) to yield:

$$P_{FS}(\tau) * P_{HI}(\tau) = K_{FS} K_{HI} \frac{1}{2}\sqrt{\frac{\pi}{a}} \exp\left(\frac{b^2}{a}\right) erfc\left(\frac{b}{\sqrt{a}}\right) =$$
$$= K_{FS} K_{HI} \frac{1}{2}\sqrt{\frac{\pi}{a}} \exp\left(\frac{\alpha^2}{4a}\right) \exp(-\alpha\tau) \operatorname{erfc}\left(\frac{b}{\sqrt{a}}\right) \quad (26)$$

Now, since $erfc(\bullet) = 1 - erf(\bullet)$, the last equation can be written as:

$$P_{FS}(\tau) * P_{HI}(\tau) = K_{FS} K_{HI} \frac{1}{2}\sqrt{\frac{\pi}{a}} \exp\left(\frac{\delta^2}{2}\right) \cdot$$
$$\cdot \exp\left(-\frac{\delta}{\sigma_C}\tau\right)\left[1 + erf\left(\frac{\tau}{\sqrt{2}\sigma_C} - \frac{\delta}{\sqrt{2}}\right)\right] \quad (27)$$

where $\delta = \alpha\sigma_C$. Finally, the system impulse response can be written as reported in following equation (28):

$$IR(\tau)\big|_{\xi=0} = P_{FS}(\tau) * P_{HI}(\tau) =$$
$$= K\sigma^0 \frac{1}{2}\sqrt{\frac{\pi}{2}} \exp\left(\frac{\delta^2}{2}\right) \exp\left(-\frac{\delta}{\sigma_C}\tau\right)\left[1 + erf\left(\frac{\tau}{\sqrt{2}\sigma_C} - \frac{\delta}{\sqrt{2}}\right)\right]$$

where $K = \dfrac{G_0^2 \lambda^2 c}{2(4\pi)^2 L_p h^3} P_T \eta \sigma_p \sqrt{2\pi}$.

Therefore, the impulse response admits a closed form solution for nadir evaluation, which is the same evaluated in [2]. This equation is not dependent of any condition about the altimeter's operative mode, e.g. pulse-limited or not, and it can be considered as a generalization of the Brown's model.

The Brown's approximate expression for the average return power is of the following form **[5]**:

$$IR(\tau) \approx P_T \eta \sigma_p \sqrt{2\pi} P_{FS}(\tau) \frac{1}{2}\left[1 + erf\left(\frac{\tau}{\sqrt{2}\sigma_C}\right)\right] \quad (29)$$

which is valid for $\tau \geq 0$. If the altimeter operating conditions vary towards a typical pulse-limited mode, then the equation 28 gives back the classical *Brown echo*, whose validity conditions are met when the parameter δ is small (e.g. δ<<1) **[5]**. In fact, in that case, we have that:

$$\frac{\delta^2}{2} << \frac{\delta}{\sigma_C}$$

into the expression (25). Moreover, the term $\delta / \sqrt{2}$ can be neglected with respect to $\tau / \sqrt{2}\sigma_C$, thus obtaining the expression (29).

For the Cassini Radar Altimeter, δ varies between 0.5 and 1.1, as shown in Figure 16.

Since $\delta = \alpha\sigma_C$, in general, the condition δ<<1 can be met if:

1) $\alpha = f(\gamma^{-1}h^{-1})$ is small, i.e. the spacecraft altitude h increases, given the beamwidth and the pulse duration, and/or the antenna parameter $\gamma = f(\theta_{3dB})$ increases
2) σ_C is small, i.e. the parameter σ_p decreases due to a greater bandwidth B.

Some case studies of echo waveforms with varying δ are shown in Figure 17, in order to perform a comparison between the IR model (28) and the Brown's model in case of nadir incidence. For the Skylab S-193 radar altimeter the following parameters have been considered, according to [5]: h=435.5 km, θ_{3dB}=1.78°, σ_p=29.3 ns.

An example of nadir pointing impulse response evaluation for the Cassini Radar Altimeter is given in Figure 18 with varying spacecraft altitude.

In the Figure 19, examples of nadir pointing impulse responses are reported, which have been evaluated for different values of σ_h, the standard deviation of the surface height. As expected, the shape of the IR function exhibits no significant broadening as a consequence of values of the surface roughness which are below the limit settled by the vertical resolution of the altimeter. In fact, the Cassini Radar instrument is not capable to resolve variations in surface heights below 30 m, which is the width of each range bin, and it will not map them.

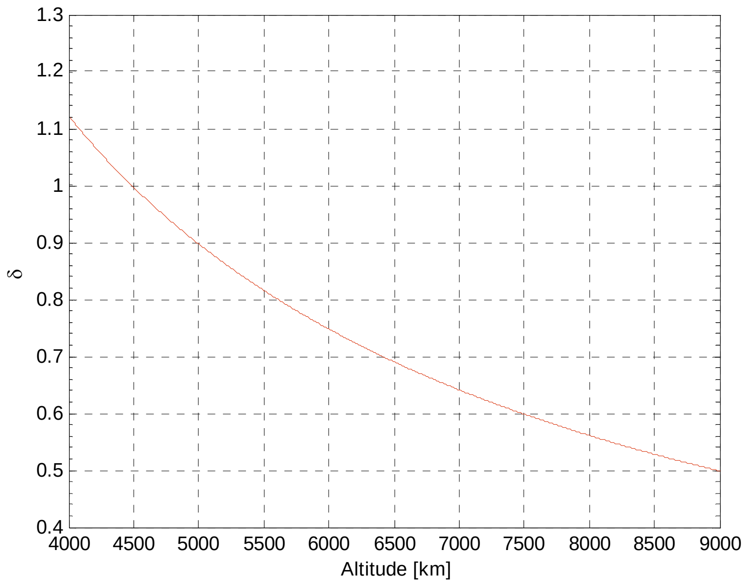

Figure 16 – Parameter δ versus spacecraft altitude for the Cassini Radar Altimeter

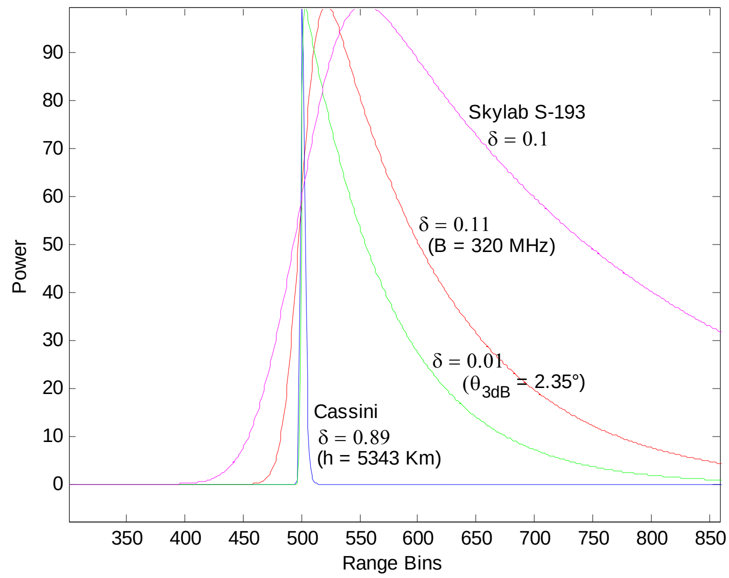

Figure 17 – Comparison between IR models

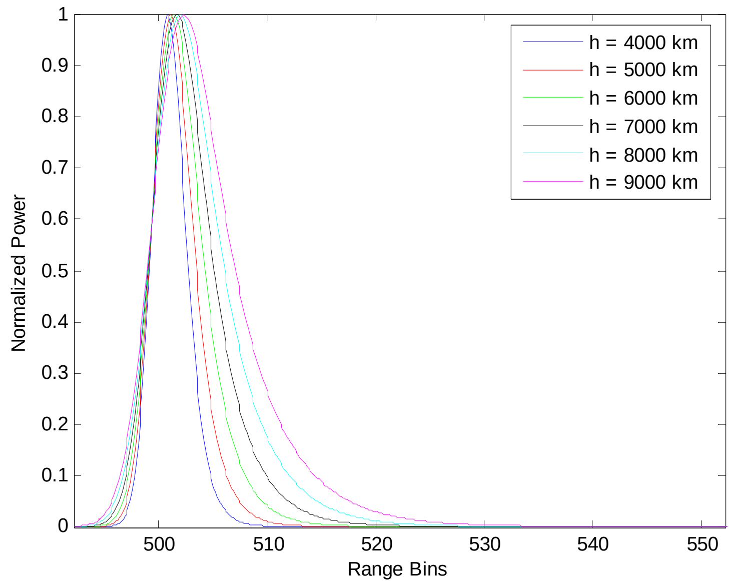

Figure 18 – Cassini Nadir pointing IR simulation with varying spacecraft altitude (rms=2 m)

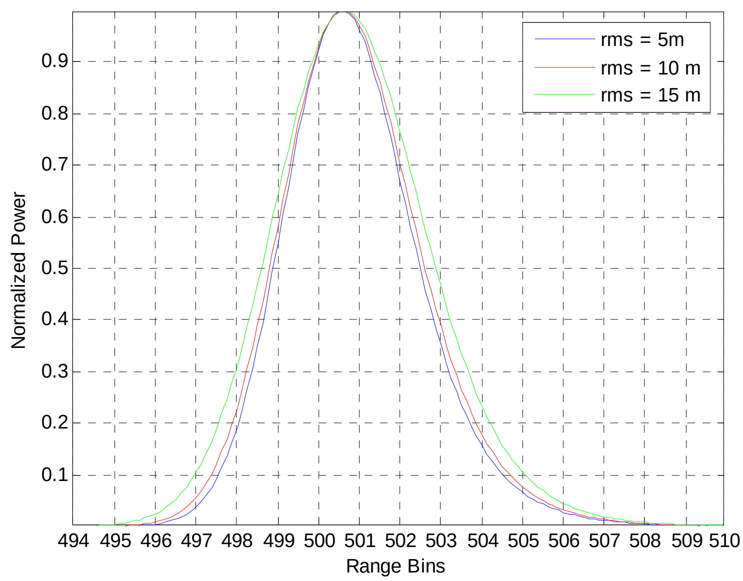

Figure 19 – Nadir pointing IR for different values of surface rms height

3.1.3 MLE Algorithm

We note from (28) that $IR(\tau) = f(t_0, \sigma^0, \sigma_S)$, i.e. the model allows to determine significant parameters describing the surface topographic features and small scale structure. These variables, namely the time delay and the surface reflectivity and roughness, can be estimated through classical methods provided by information theory. The attainable accuracy is strongly dependent on the implemented estimation algorithm. Clearly, for a radar altimeter, the error on height retrieval is the most critical one.

A Maximum Likelihood (ML) estimator will be implemented in the following, in order to obtain statistically optimal estimates of the above parameters. An advantage of such an approach is represented by the opportunity to use numerical methods. For instance, an iterative procedure will be used in the following in order to maximize the likelihood function.

Such an estimator is asymptotically *unbiased*, that is $E(\varepsilon) = 0$, and *efficient*, that is $\mathrm{var}(\varepsilon) = \min$ (asymptotically "minimum variance") where ε is the error of the estimate.

The likelihood function that represents the conditional probability density function of the echo model given the received echo samples, results to be:

$$P\left(\overline{V}/V\right) \qquad (30)$$

where $\overline{V}$ represents the model and V the real data. This method involves the maximization of the likelihood function with respect to V **[8]**, **[9]**. This condition can be stated in the following form:

$$\frac{\partial P\left(\overline{V}\middle|V\right)}{\partial V} = 0 \qquad (31)$$

For most cases of interest to altimetry, the likelihood function is expressed by an exponential form, being $\overline{V}$ a power, i.e. the square modulus of two complex gaussian variables, since the radar echo is typically processed after square law detection. Thus we can write the (30) as:

$$P\left(\overline{V}\middle|V\right) = \frac{1}{\overline{V}}\exp\left(\frac{V}{\overline{V}}\right) \qquad (32)$$

It is more convenient to maximize the logarithm of the likelihood function (*log-likelihood* function) instead of the function itself, since they have their maximum point at the same value. Thus, we can write:

$$\frac{\partial}{\partial \underline{A}}\log\left[P\left(\overline{V}\middle|\underline{A}\right)\right]=0\Leftrightarrow\frac{\partial}{\partial \underline{A}}\left[\log\left(\frac{1}{\overline{V}}\right)-\frac{V}{\overline{V}}\right]\frac{\partial\overline{V}}{\partial \underline{A}}+\frac{V}{\overline{V}^2}\frac{\partial\overline{V}}{\partial \underline{A}}=0$$

where $\underline{A}=\underline{A}(t_0,\sigma^0,\sigma_S)$ is the vector of unknown parameters.

Finally, the condition (31) becomes:

$$\frac{V-\overline{V}}{\overline{V}^2}\cdot\frac{\partial\overline{V}}{\partial \underline{A}}=0 \qquad (33)$$

where the first partial derivatives $\partial\overline{V}/\partial\underline{A}$ are called “gating functions”.

In order to provide the asymptotic behaviour of MLEs, the theoretical Cramer-Rao bounds must be evaluated, which represent the better accuracy attainable in the estimate, i.e. the minimal achievable variance in presence of zero mean white gaussian noise. In fact, the received echo is affected by *speckle*, other than by thermal noise.

For any unbiased estimator, the Cramer-Rao theorem states that the covariance matrix $\underline{\underline{C}}(\underline{A})$ satisfies the following condition:

$$\underline{\underline{C}}\left(\underline{A}\right)-\underline{\underline{F}}^{-1}\left(\underline{A}\right)\geq 0 \qquad (34)$$

where $\underline{\underline{F}}$ is the so-called Fischer “information” matrix of the parameter vector $\underline{A}$. The *ij*-th element of this symmetric matrix is given by expected values of the second partial derivatives of the log-likelihood function (“expected Fisher information” **[10]**),

$$F(i,j)=-E\left\{\frac{\partial^2}{\partial A_i\cdot\partial A_j}\left[\log\left(P\left(\overline{V}\middle|\underline{A}\right)\right)\right]\right\} \qquad (35)$$

where E denotes expected value.

Some important properties of the Fisher matrix, which essentially describes the amount of information data provide about an unknown parameter, are:

1) it is non-negative definite
2) it is additive for independent samples, i.e. the expected Fisher information for a sample of *n* independent observations is equivalent to *n* times the Fisher information for a single observation
3) it is dependent on the choice of parameterization, that is, how the parameters of a model are combined in the model's equation to define the probability density function.

The equation (35) can be written in the following form:

$$F(i,j) = -E\left\{J\left[\log\left(P\left(\bar{V}\middle|\underline{A}\right)\right)\right]\right\} \qquad (36)$$

where

$$J = \begin{pmatrix} \dfrac{\partial^2}{\partial(\sigma^0)^2} & \dfrac{\partial^2}{\partial\sigma^0\partial t_0} & \dfrac{\partial^2}{\partial\sigma^0\partial\sigma_S} \\ \dfrac{\partial^2}{\partial t_0\partial\sigma^0} & \dfrac{\partial^2}{\partial t_0^2} & \dfrac{\partial^2}{\partial t_0\partial\sigma_S} \\ \dfrac{\partial^2}{\partial\sigma_S\partial\sigma^0} & \dfrac{\partial^2}{\partial\sigma_S\partial t_0} & \dfrac{\partial^2}{\partial\sigma_S^0} \end{pmatrix} \qquad (37)$$

The condition (34), i.e. the absolute lower bound on the error variance, becomes (Cramer-Rao inequality):

$$\mathrm{var}\left(A_i\right) \geq \mathrm{F}^{-1}\left(i,i\right) \qquad (38)$$

where $\mathrm{var}\left(A_i\right)$ is the variance of any unbiased estimator of the *i*-th component of $\underline{A}$, and $\mathrm{F}^{-1}\left(i,i\right)$ is the *i*-th diagonal element of the Fisher matrix. Since the unbiased ML estimator under consideration provides an *efficient* estimate of unknown parameters A_i, then the condition (38) becomes:

$$\mathrm{var}\left(A_i\right) = \mathrm{F}^{-1}\left(i,i\right) \qquad (39)$$

i.e. the ML estimator attains the Cramer-Rao lower bound.

3.1.4 Evaluation of Gating Functions for Nadir Pointing Model

It has been demonstrated that Nadir model is described by following equation:

$$\overline{V} = K\sigma^0 \frac{1}{2}\sqrt{\frac{\pi}{2}} \exp\left(\frac{\delta^2}{2}\right) \exp\left(-\frac{\delta}{\sigma_C}\tau\right) \left[1 + erf\left(\frac{\tau}{\sqrt{2}\sigma_C} - \frac{\delta}{\sqrt{2}}\right)\right] \qquad (40)$$

The gating functions which must be evaluated in order to find the MLEs are $\partial\overline{V}/\partial t_0$, $\partial\overline{V}/\partial\sigma^0$, and $\partial\overline{V}/\partial\sigma_S$.

I. Evaluation of $\frac{\partial\overline{V}}{\partial t_0}$:

By placing $A = K\sigma^0 \frac{1}{2}\sqrt{\frac{\pi}{2}}$ into the equation of the model, and considering that $\tau = t - 2h/c = t - t_0$, the nadir model can be written in the following form:

$$\overline{V} = A\exp\left(\frac{\delta^2}{2}\right) \exp\left(-\frac{\delta}{\sigma_C}t\right) \exp\left(\frac{\delta}{\sigma_C}t_0\right) \left[1 + erf\left(\frac{t - t_0}{\sqrt{2}\sigma_C} - \frac{\delta}{\sqrt{2}}\right)\right] \qquad (41)$$

After placing $B = A\exp\left(\frac{\delta^2}{2}\right)\exp\left(-\frac{\delta}{\sigma_C}t\right)$, this equation becomes

$$\overline{V}(t_0) = B\exp\left(\frac{\delta}{\sigma_C}t_0\right)\left[1 + erf\left(\frac{t - t_0}{\sqrt{2}\sigma_C} - \frac{\delta}{\sqrt{2}}\right)\right] \qquad (42)$$

By taking the derivative with respect to t_0 we obtain[1] following equation (43)

[1] Note that: $erf(z) = \frac{2}{\sqrt{\pi}}\int_0^z \exp\left(-t^2\right)dt \Rightarrow \frac{d}{dz}\left(erf(z)\right) = \frac{2}{\sqrt{\pi}}\exp\left(-z^2\right)$

$$\frac{\partial \bar{V}(t_0)}{\partial t_0} = B\frac{\delta}{\sigma_C}\exp\left[\frac{\delta}{\sigma_C}t_0\right]\left[1+erf\left(\frac{t-t_0}{\sqrt{2}\sigma_C}-\frac{\delta}{\sqrt{2}}\right)\right]+B\exp\left[\frac{\delta}{\sigma_C}t_0\right]\frac{\partial}{\partial t_0}\left[1+erf\left(\frac{t-t_0}{\sqrt{2}\sigma_C}-\frac{\delta}{\sqrt{2}}\right)\right]$$

and hence, the first gating function is given by:

$$\frac{\partial \bar{V}(t_0)}{\partial t_0} = \bar{V}\frac{\delta}{\sigma_C} - \sqrt{\frac{2}{\pi}}\frac{1}{\sigma_C}\exp\left[\frac{\delta}{\sigma_C}t_0\right]\exp\left[-\frac{\left(t-t_0\right)^2}{2\sigma_C^2}+\frac{\delta^2}{2}\right] \quad (44)$$

Similarly, the model can be written in the following form:

$$\bar{V} = K\sigma^0\frac{1}{2}\sqrt{\frac{\pi}{2}}\exp\left(\frac{\delta^2}{2}-\frac{\delta}{\sigma_C}\tau\right)\left[1+erf\left(\frac{\tau}{\sqrt{2}\sigma_C}-\frac{\delta}{\sqrt{2}}\right)\right] \quad (45)$$

thus obtaining a more operative expression for the first gating function reported in the following equation (46):

$$\frac{\partial \bar{V}(t_0)}{\partial t_0} = \bar{V}\frac{\delta}{\sigma_C} - \sqrt{\frac{2}{\pi}}\frac{1}{\sigma_C}\exp\left[\frac{\delta^2}{2}-\frac{\delta}{\sigma_C}(t-t_0)\right]\exp\left[-\frac{\left(t-t_0\right)^2}{2\sigma_C^2}+\frac{\delta^2}{2}\right]$$

II. Evaluation of $\frac{\partial \bar{\mathbf{V}}}{\partial \boldsymbol{\sigma}^{\mathbf{0}}}$:

The second gating function is simply given by

$$\frac{\partial \bar{V}}{\partial \sigma^0} = \frac{\bar{V}}{\sigma^0} \quad (47)$$

III. Evaluation of $\frac{\partial \bar{\mathbf{V}}}{\partial \boldsymbol{\sigma}_{\boldsymbol{S}}}$:

Considering that $\delta = \alpha\sigma_c$, we obtain:

$$\bar{V}(\sigma_C) = A\exp\left(\frac{\alpha^2\sigma_C^2}{2}\right)\exp\left(-\alpha\tau\right)\left[1+erf\left(\frac{\tau}{\sqrt{2}\sigma_C}-\frac{\alpha\sigma_C}{\sqrt{2}}\right)\right] \quad (48)$$

After placing $C = A\exp\left(-\alpha\tau\right)$ in the last relation, we have

$$\bar{V}(\sigma_C) = C\exp\left(\frac{\alpha^2\sigma_C^2}{2}\right)\left[1 + erf\left(\frac{\tau}{\sqrt{2}\sigma_C} - \frac{\alpha\sigma_C}{\sqrt{2}}\right)\right] \qquad (49)$$

By taking the derivative with respect to σ_C, we obtain the relation following (50):

$$\frac{\partial\bar{V}(\sigma_C)}{\partial\sigma_C} = \sigma_C^2\alpha^2\exp\left[\frac{\alpha^2}{2}\sigma_C^2\right]\left[1 + erf\left(\frac{\tau}{\sqrt{2}\sigma_C} - \frac{\alpha\sigma_C}{\sqrt{2}}\right)\right] +$$
$$-\sigma_C\exp\left[\frac{\alpha^2}{2}\sigma_C^2\right]\left[\frac{2}{\sqrt{\pi}}\exp\left[-\frac{\left(\tau - \alpha\sigma_C^2\right)^2}{2\sigma_C^2}\right]\left(\frac{\tau}{\sqrt{2}\sigma_C^2} + \frac{\alpha}{\sqrt{2}}\right)\right]$$

and hence equation (51):

$$\frac{\partial\bar{V}(\sigma_C)}{\partial\sigma_C} = \bar{V}\sigma_C\alpha^2 - \sigma_C\exp\left[\frac{\alpha^2}{2}\sigma_C^2\right]\left[\frac{2}{\sqrt{\pi}}\exp\left[-\frac{\left(\tau - \alpha\sigma_C^2\right)^2}{2\sigma_C^2}\right]\left(\frac{\tau}{\sqrt{2}\sigma_C^2} + \frac{\alpha}{\sqrt{2}}\right)\right]$$

Finally, the third gating function is given by

$$\frac{\partial\bar{V}}{\partial\sigma_S} = \frac{\partial\bar{V}}{\partial\sigma_C}\frac{\partial\sigma_C}{\partial\sigma_S} \qquad (52)$$

where $\frac{\partial\sigma_C}{\partial\sigma_S} = \frac{1}{2\sigma_C}\left(2\sigma_S\right) = \frac{\sigma_S}{\sigma_C}$.

3.1.5 Model Implementation and Results

In order to validate the model from a theoretical point of view the algorithm described in section 3.5 has been applied. In the following the main results are reported.

The numerical simulation, performed by a MATLAB® code, leads to the results reported in Figure 20.

A white gaussian thermal noise has been generated and overlapped with the model in order to obtain the simulated radar data. Moreover, in order to reduce the noise in individual pulses, the average of all of the 15 pulses within each burst has been performed.

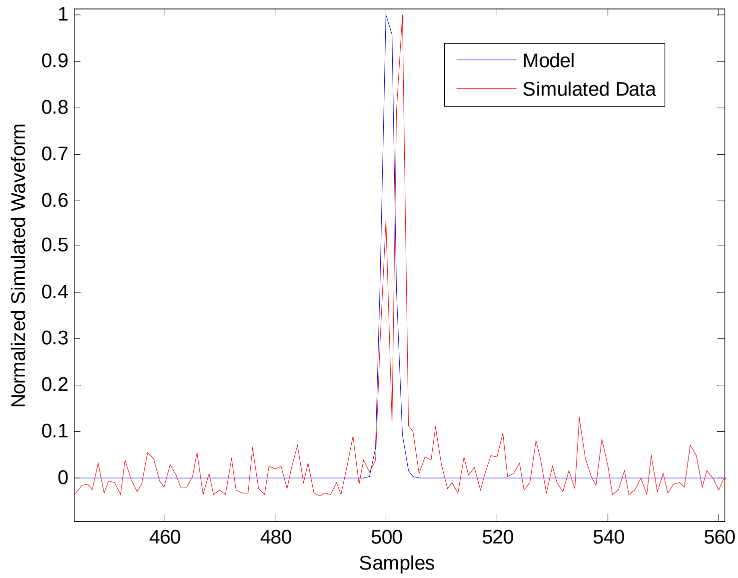

Figure 20 – Fitting of simulated echo with theoretical nadir model

An example of fitting of LBDR data (row data) from Ta fly-by [1], supplied by JPL to ASI, with nadir model described by equation (28), is given in the following. The supplied file contains only high resolution altimeter data from burst #14326 up to #14783 (i.e. 389 bursts).

In Figure 21 the burst #14331 has been considered. A single pulse is obtained by averaging all the received pulses within the burst.

As clearly shown, compressed LBDR data do not fit with this waveform model, which is too tight.

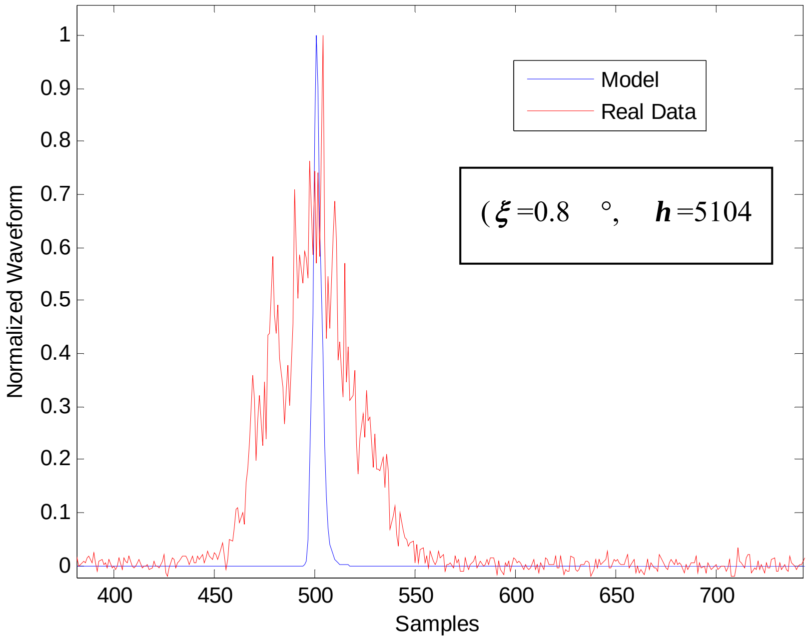

Figure 21 – Fitting of real echo with theoretical nadir model

By considering the pointing angle of the Cassini Radar Altimeter versus the burst number, as resulting from the same sub-set of data[2], we can evidence a variation of pointing angle during the Titan fly-by, as shown in Figure 22. Here the Cassini spacecraft altitude varies from ~ 5000 km up to ~ 9000 km, since the supplied data contain records from the outbound track of hyperbolic fly-by.

For the burst under consideration (i.e. #15 in Figure 22), the off-nadir angle is around 0.8 deg. However, the mean value of ξ is around 0.23 deg. This variation suggests the need of a specific model which takes into account the altimeter antenna boresight off-pointing from the nadir direction.

---

[2] The off-nadir angle is evaluated from the incidence angle at Titan's surface (fly-by trajectory supposed to be rectilinear)

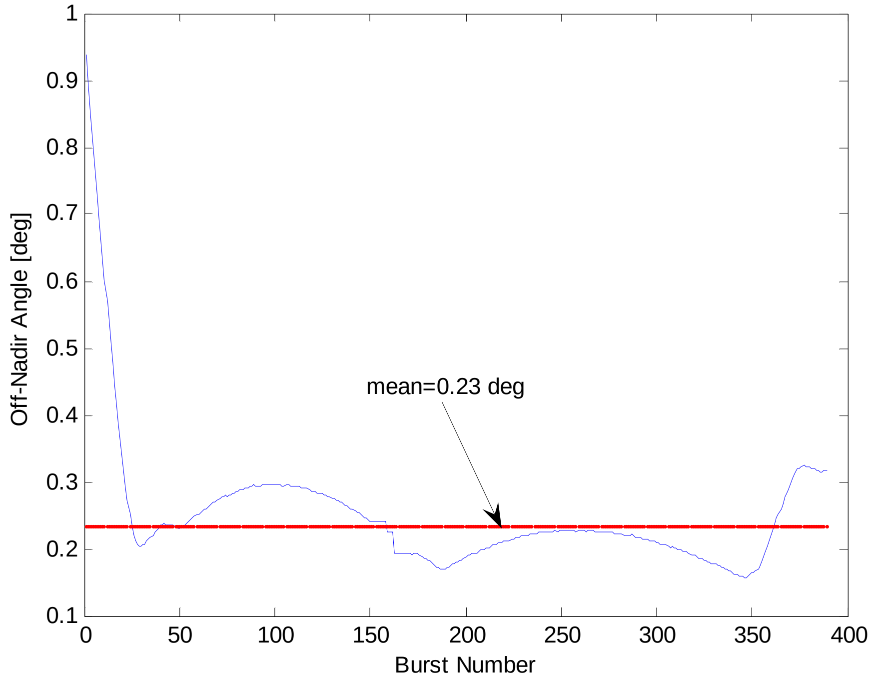

Figure 22 – Cassini Ta fly-by: Off-nadir angle history

3.2 RA Off-Nadir Pointing

As previously introduced in section 2.2.1, conventional altimeter provides a surface topography profile along the flight line. In most cases, the scientific requirement is to acquire surface topography over two-dimensional surface. A first intuitive solution to the problem of spatial and temporal sampling for the ocean observations is represented by the modification of the conventional Pulse Limited radar altimeter concept by extending its limited, although high performing, nadir looking measurement capability with the inclusion of off-nadir measurements taken from additional antenna beams pointed off-nadir. The individual beam's footprints should be spaced in the horizontal plane to achieve the swath widths needed for various scientific applications. The extent of the footprints is determined by the beam forming antenna system. Figure 23 shows the geometry of the acquisition for this kind of system. The individual beam's footprints should be spaced in the horizontal plane to achieve the swath widths needed for various scientific applications. The extent of the footprints is determined by the beam forming antenna system. The addition of off-nadir beams creates a remarkable increase in the number of intersections (crossovers) between ascending and descending tracks.

The instantaneous surface footprint of a real aperture imaging altimeter usually defines the superficial resolutions X_r and X_a in the cross track and along track dimensions, respectively. The height resolution (ΔH) depends on the surface slope, illumination geometry, and sensor characteristic. Being ξ the off-nadir angle, the echo will be spread as a result of the oblique geometry as shown in Figure 24 and expressed by the following relation:

$$\Delta H = \frac{H\theta_B \tan(\xi)}{\cos(\xi)}$$

where θ_B is the angle between the half power points of the main beam. This causes an echo spread that leads to a decrease in the total height measurement accuracy. This effect can be reduced by analysing the total echo shape instead of measuring the time of arrival of the leading edge, but this implies an accurate satellite attitude control system. A possible solution to the attitude estimation problem is to model the expected return waveforms for a range of off-nadir angles and compare them to the measured return. This method requires huge data storage and, inevitably, long processing times. Another possibility is to analyse the modelled returns and develop an algorithm that is able to indicate the pointing angle when applied to the measured returns. This has the potential of reducing the processing time, but in either case, it is necessary to model the expected or average return waveforms. The convolutional model described in equation (20) can be used. It describes the average return waveforms in terms of three known quantities: the average flat surface impulse response (FSIR), the radar system point target response (PTR), and the height probability density function of the specular points on the observed surface. If many waveforms are desired, for a range of pointing angles or *rms* sea height for example, the number of necessary convolution grows.

The FSIR includes the effects of the antenna pattern, surface curvature, range variation within the pulse footprint as a function of time, and the surface backscattering variation as a function of the incidence angle.

In the following paragraphs an altimeter waveform model is analyzed, which could be used to evaluate the average echo waveform behaviour in case of off-pointing from the nadir direction.

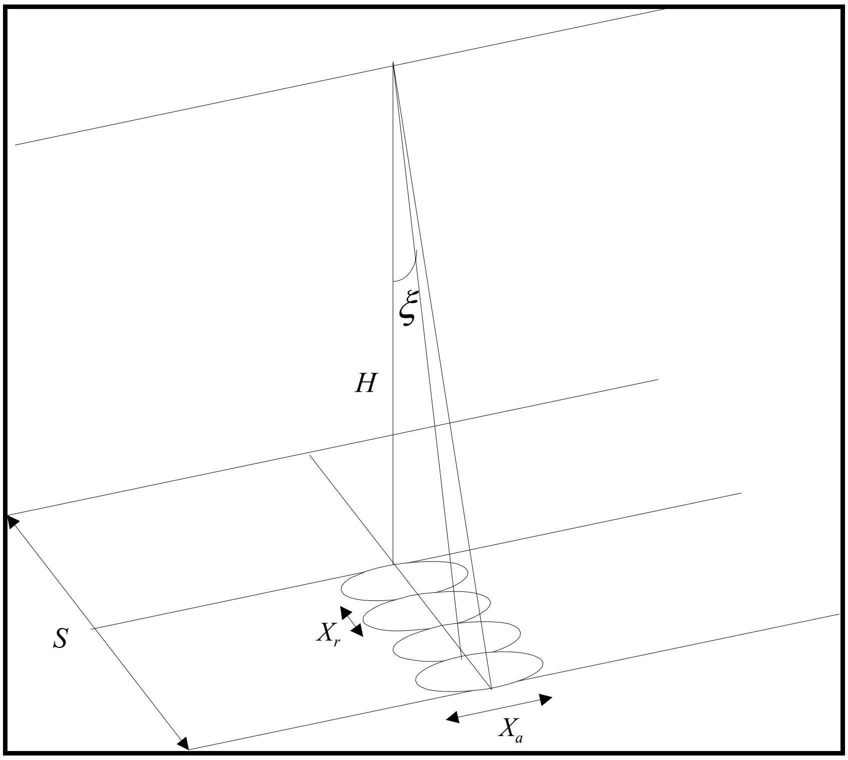

Figure 23 – Geometry for scanning off-nadir radar altimeter

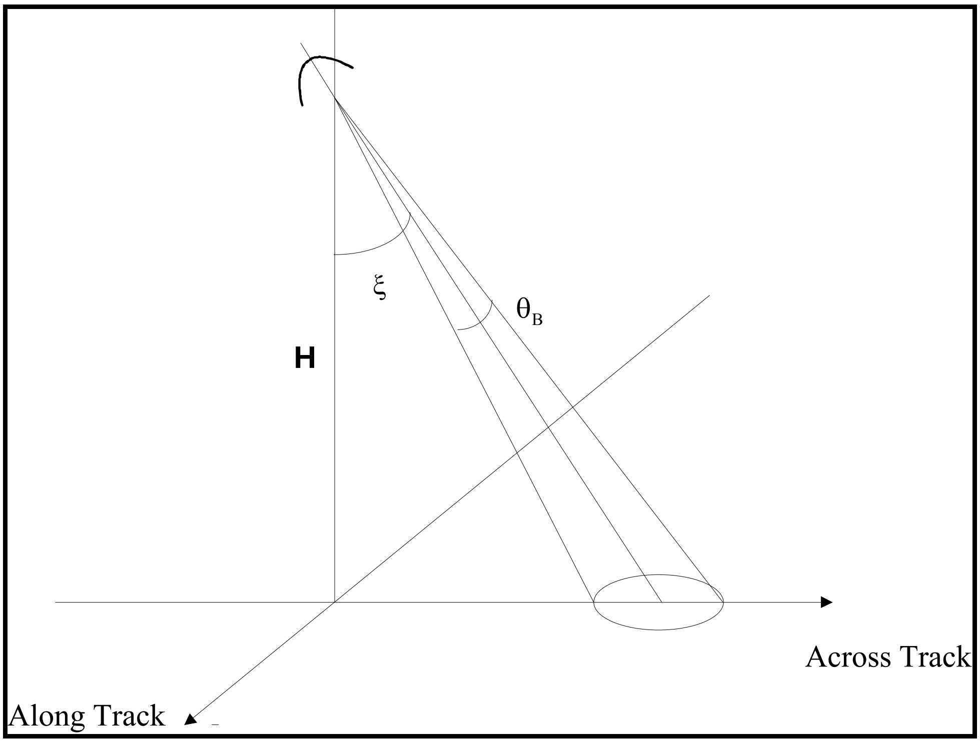

Figure 24 – Across track geometry

3.2.1 Off-Nadir FSIR Evaluation

An accurate expression of FSIR, as given in [5] and it is shown in the following relation:

$$P_{FS}(t) = \frac{\lambda^2}{(4\pi)^3 L_p} \int_S \frac{\delta\left(t - \frac{2r}{c}\right) G^2(\theta,\omega)\sigma^0(\psi,\phi)}{r^4} dA$$

where:

λ	Radar wavelength
L_p	Two-way path loss
$\delta\left(t-\frac{2r}{c}\right)$	Transmitted impulse function delayed time

c	Speed of light in vacum
$G^2(\theta,\omega)$	Two-way power Gain Pattern of the radar antenna
r	Range of the scattering area dA on surface
$\sigma^0(\psi,\phi)$	Radar Cross Section per unit area of illuminated surface

Table 3 – System Parameters

Figure 25 explains the involved geometry. The development of the FSIR has been already done in [5] by assuming the antenna pattern $G(\theta,\omega)$ as circularly symmetric Gaussian beam, given by:

$$G(\theta) = G_0 \exp\left(-\frac{2}{\gamma}\sin^2\theta\right)$$

where G_0 is the peak antenna gain (at boresight) and γ is defined by the 3 dB beamwidth of the power pattern. In [3] the evaluation is extended to elliptical Gaussian beam, given by:

$$G(\theta,\omega) = G_0 \exp\left(-\frac{2}{\gamma}\left(1+\beta\cdot\sin^2\omega\right)\sin^2\theta\right)$$

where ω is the angle about the antenna boresight axis and β is a parameter defines the ellipse. The value of γ and β are:

$$\gamma = -\frac{2\sin^2\left(\theta_B/2\right)}{\ln(0.5)},$$

$$\beta = -\left(1+\frac{\gamma\ln(0.5)}{2\sin^2\left(\theta_{CSB}/2\right)}\right)$$

where θ_B and θ_{CSB} are the scan and the across-scan beamwidths defined in two orthogonal planes whose intersection is the antenna boresight. The scan beamwidth is in the plane that contains the sub-nadir point and the antenna boresight axis. Using the above relations we obtain:

$$P_{FS}(t)=\frac{G_0^2\lambda^2}{(4\pi)^3 L_p}\int_0^{2\pi}\int_0^{\infty}\frac{\delta\left(t-\frac{2r}{c}\right)\sigma^0(\psi,\phi)}{r^4}\exp\left(-\frac{4}{\gamma}\left(1+\beta\cdot\sin^2\omega\right)\sin^2\theta\right)\rho d\rho d\phi$$

where the incremental area *dA* has been written as $\rho d\rho d\phi$ and in G_0^2 is the peak boresight antenna gain. Since the antenna beamwidths are assumed small, the radar cross section is taken to be ϕ independent. The ρ integration can be completed through a carefully selected sequence of variables to yield:

$$P_{FS}(t)=\frac{G_0^2\lambda^2 c\sigma^0(\psi_0)}{2(4\pi)^3 L_p h^3\left(ct/2h\right)^3}\int_0^{2\pi}\exp\left(-\frac{4}{\gamma}\left(1+\beta\cdot\sin^2\omega\right)\sin^2\theta\right)d\phi$$

for $t\geq 2h/c$ and $\psi_0=\tan^{-1}\sqrt{ct/h-2}$, being h the spacecraft altitude.

In order to complete the ϕ integral is more convenient to express the FSIR in term of the two-way incremental ranging time instead of absolute time $\tau=t-2h/c$:

$$P_{FS}(\tau)=\frac{G_0^2(\xi)\lambda^2(c/2)\sigma^0(\psi_0)}{(4\pi)^3 L_p h^3}\cdot$$
$$\cdot\int_0^{2\pi}\exp\left(-\frac{4}{\gamma}\left(1+\beta\frac{\rho^2\sin^2\phi}{\rho^2-2\rho\rho_0\cos\phi+\rho_0^2}\right)\left(1-\frac{(\cos\xi+\varepsilon\sin\xi\cos\phi)^2}{1+\varepsilon^2}\right)\right)d\phi$$

As shown before, for nadir pointing, an exact closed-form expression for the FSIR is given by equation (19). In case of *near* nadir pointing mode $(\xi\neq 0)$, the FSIR evaluation cannot be simplified. The most practical method of evaluation is by numerical integration of the above relation (see **[4]**), which is valid for $\tau\geq 0$.

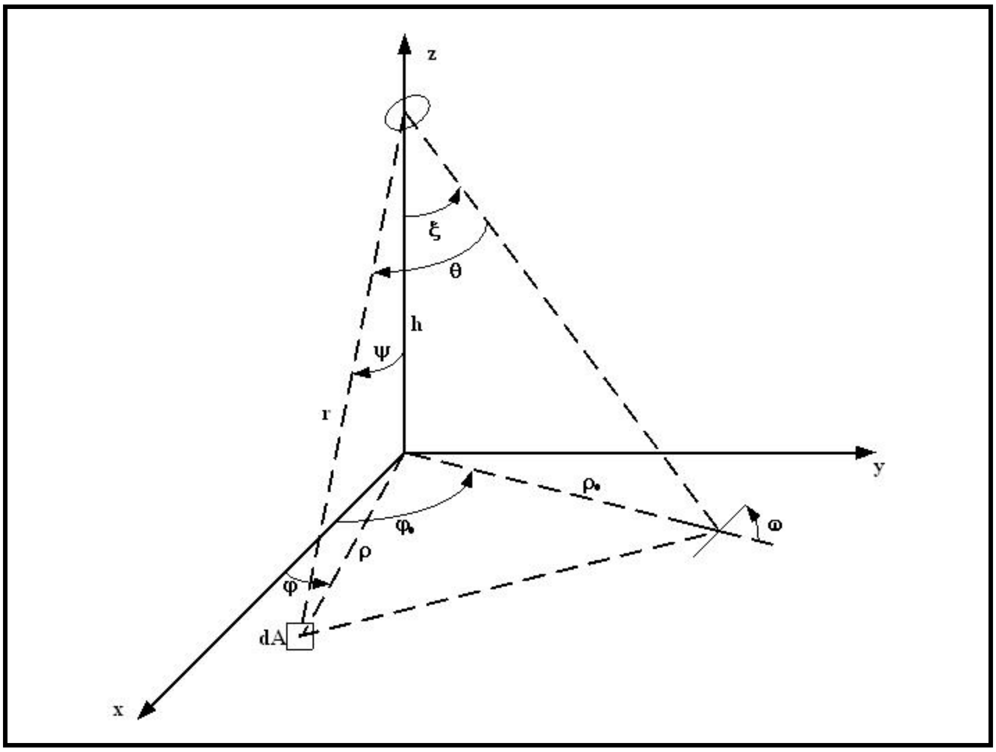

Figure 25 – Geometry for the evaluation of FSIR

The integrand in the last relation is a well-behaved, smoothly varying function that peaks in τ at the point where the antenna boresight axis intersects the illuminated surface. Since the antenna beamwidth is very small, there is only a significant contribution to the return signal when ϕ is in the neighbourhood of ϕ_0 and ε is close to ρ_0, as also stated in **[4]**.

Due to this highly peaked nature of the integrand, the ϕ integral can be evaluated asymptotically by using the Laplace's method **[7]**, thus yielding to following equation (53):

$$P_{FS}(\tau)=\frac{G_0^2\lambda^2 c\sigma^0(\psi_0)}{4(4\pi)^2 L_p h^3}\exp\left(-\frac{4}{\gamma}\frac{(\sin\xi-\varepsilon\cos\xi)^2}{(1+\varepsilon^2)}\right)\sqrt{\frac{2\pi}{a+2b}}\qquad \tau\geq 0$$

where $a=\frac{4\varepsilon}{\gamma}\frac{\sin 2\xi}{(1+\varepsilon^2)}$, $b=\frac{4\varepsilon^2}{\gamma}\frac{(\sin^2\xi+\beta\cos^2\xi)}{(1+\varepsilon^2)}$.

Considering $\beta=0$, i.e. the antenna pattern is symmetric (this is the Cassini Antenna design), then we obtain the same result as in **[5]**. The off-nadir

FSIR equation (19) becomes equation (54):

$$P_{FS}(\tau) = A\sigma^0 \exp\left(-\frac{4}{\gamma(1+\varepsilon^2)}(\sin\xi - \varepsilon\cos\xi)^2\right)\sqrt{\frac{2\pi}{a+2b}} \qquad \tau \geq 0$$

where $A = \dfrac{G_0^2\lambda^2 c}{2(4\pi)^3 L_p h^3}$, $a = \dfrac{4\varepsilon}{\gamma}\dfrac{\sin 2\xi}{(1+\varepsilon^2)}$, $b = \dfrac{4\varepsilon^2}{\gamma}\dfrac{\sin^2\xi}{(1+\varepsilon^2)}$.

As in **[4]**, we can include the spherical surface effects by writing

$$\varepsilon = \sqrt{\frac{c\tau}{h}\frac{1}{\left(1+\dfrac{h}{R_T}\right)}} \qquad (55)$$

where R_T is the mean radius of Titan (2575 km), and finally we observe that $\tau = \mathrm{K}\cdot\varepsilon^2$.

The above asymptotic approximation of equation (19) allows for easy evaluation of the FSIR for far off-nadir pointing angles and large ranging times.

According to **[5]**, a criterion is provided which, if met, ensures that the error in using the above approximation (54) in place of the numerical integration method will be less than 2% of the true value. This criterion can be expressed in the following form:

$$\tau_{\min} \geq \frac{h}{c}\left(0.849\gamma\frac{(1+\tan^2\xi)}{\tan\xi}\right)^2 \qquad (56)$$

which shows how for a given pointing angle ξ, antenna beamwidth (embedded in γ), and radar height h, there is a minimum ranging time $\tau_{\min}$ for which (54) (with $\beta = 0$) is accurate to less than 2% error, as indicated in Figure 26.

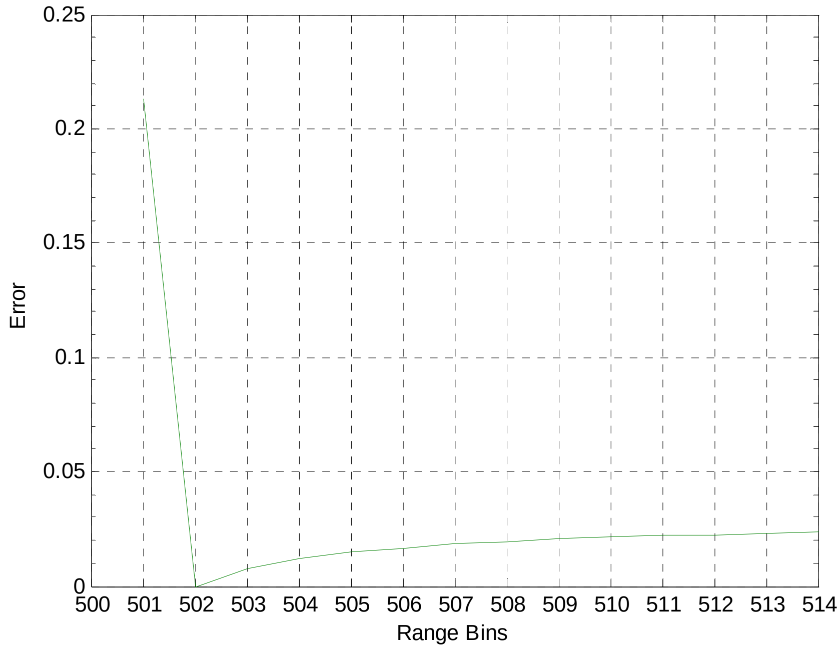

Figure 26 – Error in using the approximation (57) (ξ =0.23°, $\boldsymbol{h}$ =4000 km)

For the Cassini Radar Altimeter, the value of $\tau_{\min}$ (in range bins) with varying spacecraft altitude and off-nadir angle is given in Figure 27. As clearly shown, the error is bounded within the first few pixels.

Thus, for nadir pointing, an exact closed-form expression for the FSIR is given by equation (54), while for small ranging times or pointing angles, the FSIR must be obtained by a numerical integration of (19). For longer ranging times or larger pointing angles, the asymptotic form (54) is sufficiently accurate for the FSIR.

A comparison between the FSIR evaluated in both nadir and off-nadir case is reported in Figure 28. In the following, Figure 29 illustrates the FSIR evaluated with varying spacecraft altitude, while the evaluation with varying off-nadir angle is reported in Figure 30, so to cover all likely scenarios.

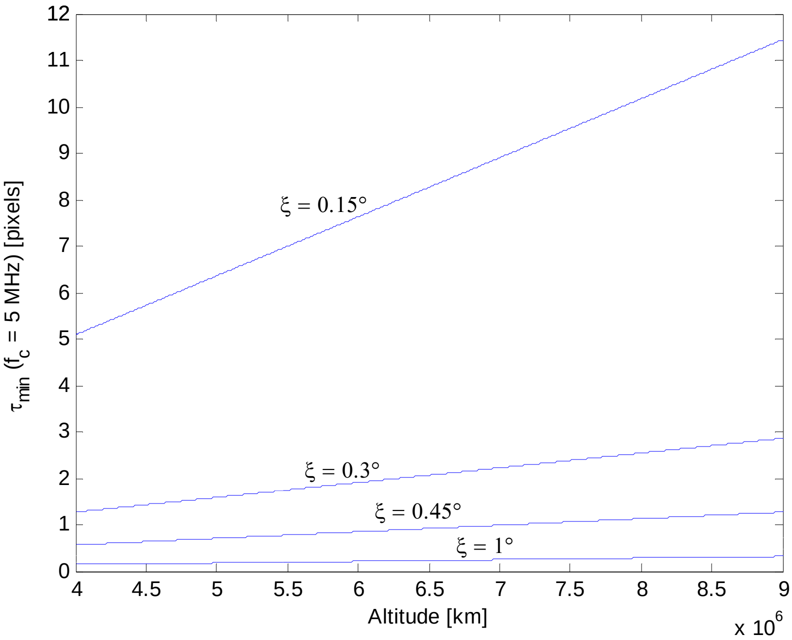

Figure 27 – Variation of τ_{min} (in range bins) with spacecraft altitude for various off-nadir angles

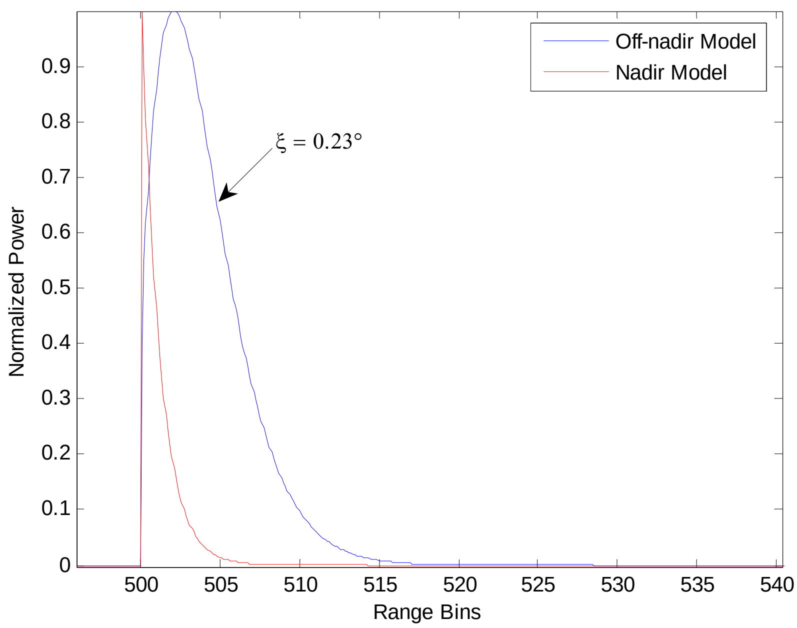

Figure 28 – Comparison between evaluated FSIR for nadir and off-nadir model

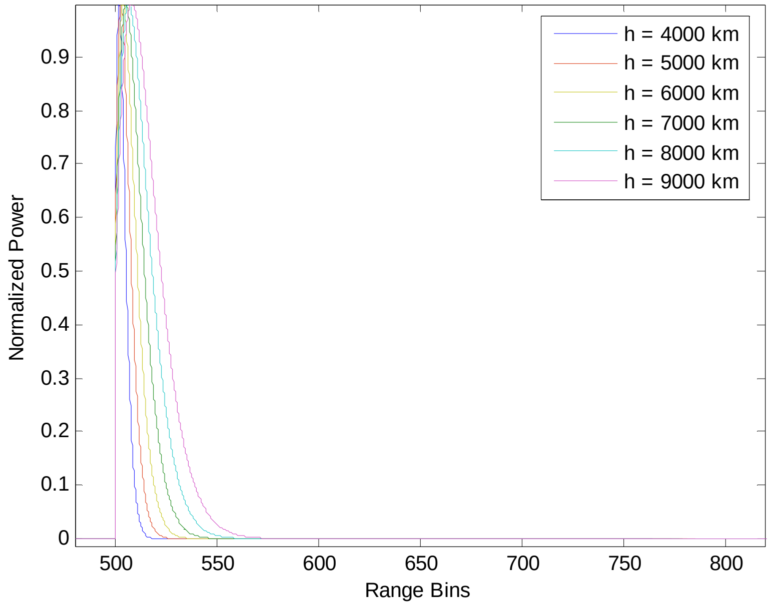

Figure 29 – FSIR evaluation with varying spacecraft altitude (ξ =0.23°)

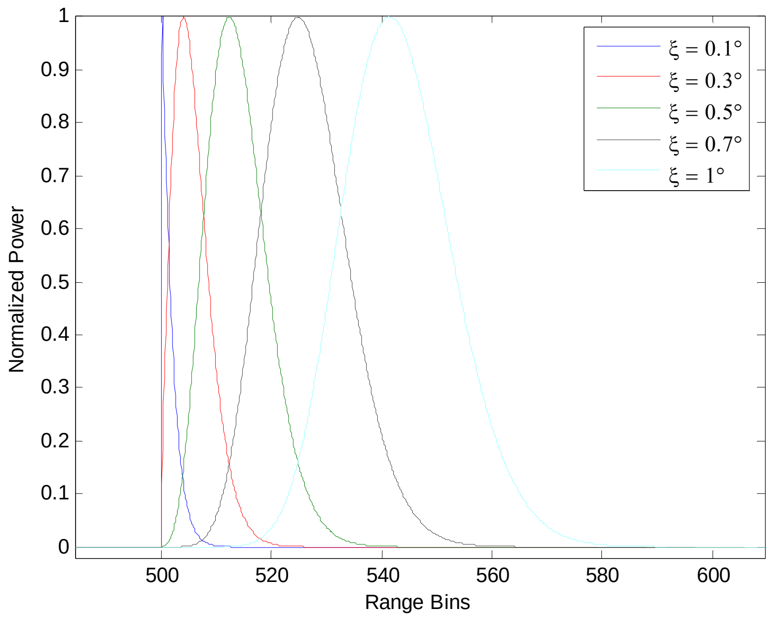

Figure 30 – FSIR evaluation with varying off-nadir angle (h =4000 km)

3.2.2 Off-Nadir IR Evaluation

As previously described, the system impulse response can be evaluated by the convolution of the FSIR with the height probability density function and the system point target response [see equation (20)]. Since the surface height distribution and the pulse response are very narrow with respect to the flat surface response, the total impulse response can be simply written as the product of the following terms [equation (57)]:

$$
\begin{aligned}
IR(\tau)\big|_{\xi\neq 0} &= P_{FS}(\tau)\cdot\sigma_P\left[1+erf\left(\frac{\tau}{\sqrt{2}\sigma_C}\right)\right]= \\
&= A\sigma^0\exp\left(-\frac{4}{\gamma\left(1+\varepsilon^2\right)}\left(\sin\xi-\varepsilon\cos\xi\right)^2\right)\sqrt{\frac{2\pi}{a+2b}}\cdot \\
&\cdot\sigma_P\left[1+erf\left(\frac{\tau}{\sqrt{2}\sigma_C}\right)\right] \qquad \tau\geq 0
\end{aligned}
$$

The above expression can be rewritten as:

$$
IR(\tau)\big|_{\xi\neq 0} = A\sigma^0\exp\left[F(\varepsilon)\right]G(\varepsilon)H(\varepsilon) \qquad (58)
$$

where:

$A=\dfrac{G_0^2\lambda^2 c}{2(4\pi)^3 L_p h^3}$, $F(\varepsilon)=\left(-\dfrac{4}{\gamma(1+\varepsilon^2)}\left(\sin\xi-\varepsilon\cos\xi\right)^2\right)$, $G(\varepsilon)=\sqrt{\dfrac{2\pi}{a+2b}}$,

and $H(\varepsilon)=\sigma_P\left[1+erf\left(\dfrac{\tau}{\sqrt{2}\sigma_C}\right)\right]$.

3.2.3 Evaluation of Gating Functions for Off-Nadir Pointing Model

Approximate Model (*Model 1*)

The expression (58) can be simplified by ignoring the term $H(\varepsilon)$ which contains the error function, thus obtaining the following approximate model (*Model 1*):

$$IR_1(\tau)\big|_{\xi\neq 0} = A\sigma^0 \exp\left[F(\varepsilon)\right]G(\varepsilon) \qquad (59)$$

In doing this, we are neglecting the effects of σ_C. Since $\sigma_C = f(\sigma_S)$, we are supposing that the model doesn't vary with the surface rms height value. Being the expected values of roughness below the vertical resolution of the altimeter, this assumption only causes an error on the first pixel (see Figure 33 in the following). The gating functions are evaluated in the following sections.

I. Evaluation of $\dfrac{\partial(IR_1)}{\partial t_0}$:

Since $\varepsilon = f(t_0)$, it is possible to derive the (58) with respect to ε and then to multiply by the derivative of ε with respect to t_0. The derivative $\dfrac{\partial(IR_1(\varepsilon))}{\partial\varepsilon}$ is simply determined. In fact, we have:

$$\begin{aligned}\frac{\partial(IR_1(\varepsilon))}{\partial\varepsilon} &= A\sigma^0\left[\exp(F(\varepsilon))F'(\varepsilon)G(\varepsilon)+\exp(F(\varepsilon))G'(\varepsilon)\right]=\\ &= IR_1(\varepsilon)F'(\varepsilon)+\frac{IR_1(\varepsilon)}{G(\varepsilon)}G'(\varepsilon)\end{aligned}$$

in which:

$$\begin{aligned}F'(\varepsilon) &= -\frac{4}{\gamma}\left[\frac{\left[\left(2\cos^2(\xi)\varepsilon-\sin(2\xi)\right)\left(1+\varepsilon^2\right)\right]-\left(\sin^2(\xi)+\cos^2(\xi)\varepsilon^2-\varepsilon\sin(2\xi)\right)2\varepsilon}{\left(1+\varepsilon^2\right)^2}\right]=\\ &= -\frac{4}{\gamma}\left[\frac{2\varepsilon\cdot\left(\cos^2(\xi)-\sin^2(\xi)\right)+\varepsilon^2\left(\sin(2\xi)\right)-\sin(2\xi)}{\left(1+\varepsilon^2\right)^2}\right]=\\ &= -\frac{4}{\gamma\left(1+\varepsilon^2\right)^2}\left[2\varepsilon\cos(2\xi)+\left(\varepsilon^2-1\right)\sin(2\xi)\right]\end{aligned}$$

Since:

$$a+2b=\frac{8\varepsilon\sin(\xi)\cos(\xi)\left[1+\varepsilon\tan(\xi)\right]}{\gamma\left(1+\varepsilon^2\right)}$$

then we can write:

$$G(\varepsilon)=\sqrt{\frac{2\pi}{a+2b}}=\sqrt{\frac{2\pi\gamma\left(1+\varepsilon^2\right)}{8\varepsilon\sin(\xi)\cos(\xi)\left[1+\varepsilon\cdot\tan(\xi)\right]}}=\sqrt{K\frac{\left(1+\varepsilon^2\right)}{\varepsilon\left[1+\varepsilon\cdot\tan(\xi)\right]}}$$

where $K=\dfrac{2\pi\gamma}{8\sin(\xi)\cos(\xi)}$.

By taking the derivative with respect to ε, we obtain:

$$G'(\varepsilon)=\frac{1}{2G(\varepsilon)}\frac{2K\varepsilon^2\left[1+\varepsilon\cdot\tan(\xi)\right]-K\left(1+\varepsilon^2\right)\left(1+2\varepsilon\tan(\xi)\right)}{\left[1+\varepsilon\cdot\tan(\xi)\right]\varepsilon^2}$$

then:

$$G'(\varepsilon)=\frac{1}{2G(\varepsilon)}\frac{K\left(\varepsilon^2-2\varepsilon\tan(\xi)-1\right)}{\left[1+\varepsilon\cdot\tan(\xi)\right]\varepsilon^2}\frac{\left(1+\varepsilon^2\right)^2}{\left(1+\varepsilon^2\right)^2}\frac{K}{K}=\frac{1}{2G(\varepsilon)}\frac{K\left(\varepsilon^2-2\varepsilon\tan(\xi)-1\right)}{K\left(1+\varepsilon^2\right)^2}G^4(\varepsilon)$$

and finally:

$$G'(\varepsilon)=\frac{G^3(\varepsilon)}{2K}\frac{\left(\varepsilon^2-2\varepsilon\tan(\xi)-1\right)}{K\left(1+\varepsilon^2\right)^2}\quad(60)$$

Now, since $\varepsilon=f(\tau)$ and $\tau=t-t_0$, then we obtain:

$$\frac{\partial\varepsilon}{\partial t_0}=-\frac{1}{2\varepsilon}\frac{c}{h\left(1+\dfrac{h}{R_e}\right)}\quad(61)$$

Finally, the first gating function is given by:

$$\frac{\partial(IR_1)}{\partial t_0}=\frac{\partial(IR_1)}{\partial\varepsilon}\frac{\partial\varepsilon}{\partial t_0}\quad(62)$$

Complete Model (Model 2)

The equation of the complete model (*Model 2*) is given by (57), which can be written in the following form:

$$IR_2(\tau)\big|_{\xi\neq 0} = IR_1(\tau)\big|_{\xi\neq 0} \cdot H(\tau) \quad (63)$$

where:

$$IR_1(\tau)\big|_{\xi\neq 0} = A\sigma^0 \exp\left[F(\varepsilon)\right]G(\varepsilon) \;\;, \; H(\tau) = \sigma_P\left[1 + erf\left(\frac{\tau}{\sqrt{2}\sigma_C}\right)\right].$$

This model is reported in the following Figure 31 and Figure 32, for all likely scenarios in terms of spacecraft altitude and off-pointing angle.

If we perform a comparison between the two IR models, it is possible note that the shape of IR_1 is really close to that of IR_2, as shown in Figure 33. This is due to the behaviour of the erf function for small off-nadir pointing angles. Therefore, its contribution (i.e. the term $H(\varepsilon)$ into the expression (52)) can be neglected without affecting the accuracy of results.

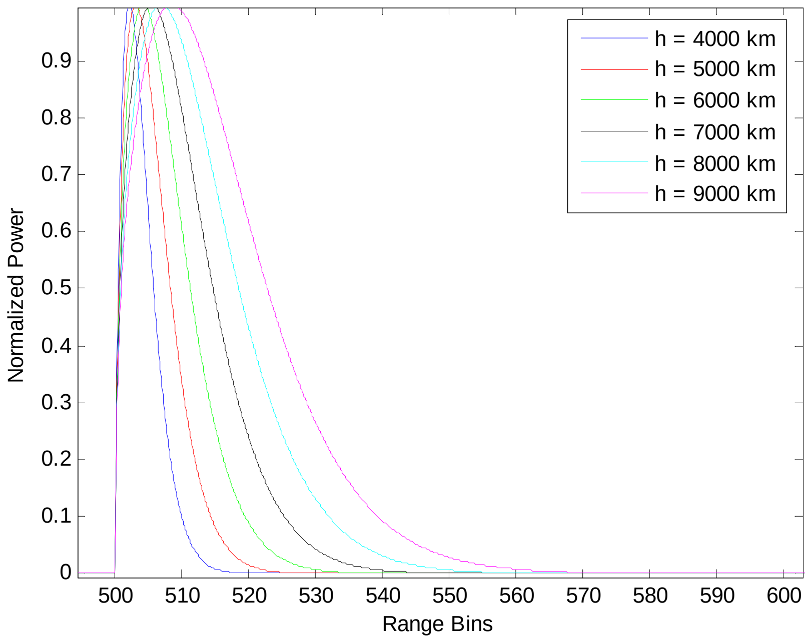

Figure 31 – Complete model with varying spacecraft altitude (ξ =0.23°)

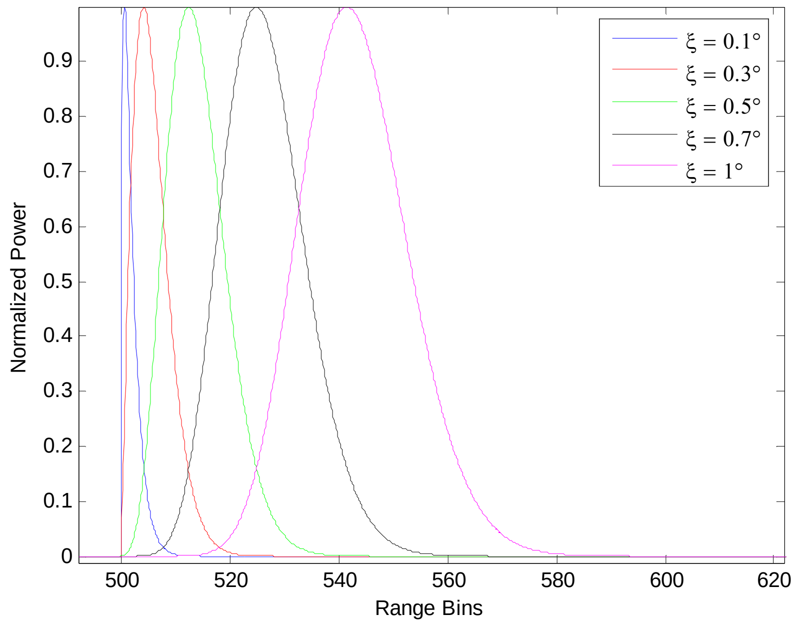

Figure 32 – Complete model with varying off-nadir angle ($\boldsymbol{h}$ =4000 km)

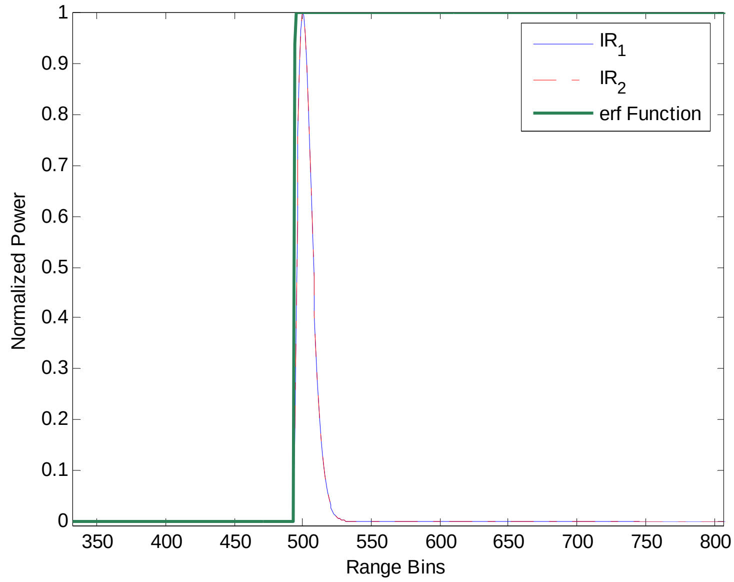

Figure 33 – Comparison between IR models (ξ =0.3°)

I Evaluation of $\frac{\partial(IR_2)}{\partial t_0}$:

The derivative of the complete model with respect to t_0 is given by

$$\frac{\partial[IR_2(\varepsilon)]}{\partial t_0}=\frac{\partial(IR_2)}{\delta\varepsilon}\frac{\delta\varepsilon}{\partial t_0}=\left[\frac{\partial Y(\varepsilon)}{\partial\varepsilon}\frac{\delta\varepsilon}{\partial t_0}H(\tau)+Y(\varepsilon)\frac{\partial H(\tau)}{\partial t_0}\right] \qquad (64)$$

where $\frac{\partial Y(\varepsilon)}{\partial\varepsilon}=\frac{\partial}{\partial\varepsilon}(\mathrm{IR}_1)$ and, as previously obtained,

$$\frac{\partial(IR_1(\varepsilon))}{\partial\varepsilon}= IR_1(\varepsilon)F'(\varepsilon)+\frac{IR_1(\varepsilon)}{G(\varepsilon)}G'(\varepsilon)$$

$$\frac{\partial H(\tau)}{\partial t_0}=-\frac{2}{\sqrt{\pi}}\exp\left(-\frac{\tau^2}{2\sigma_C^2}\right)\left(\frac{1}{\sqrt{2}\sigma_C}\right).$$

II Evaluation of $\frac{\partial(IR_2)}{\partial\sigma_0}$:

The second gating function is simply given by:

$$\frac{\partial\left(IR_2(\sigma^0)\right)}{\partial\sigma^0}=\frac{IR_2}{\sigma^0} \qquad (65)$$

III Evaluation of $\frac{\partial(IR_2)}{\partial\sigma_S}$:

The third gating function is given by:

$$\frac{\partial\left(IR_2(\sigma_s)\right)}{\partial\sigma_s}=\frac{\partial\left(IR_2(\sigma_C)\right)}{\partial\sigma_C}\frac{\partial\sigma_C}{\partial\sigma_S} \qquad (66)$$

where:

$$\sigma_C=\sqrt{\sigma_S^2+\sigma_p^2}$$

$$\frac{\partial\sigma_C}{\partial\sigma_S}=\frac{1}{2\sigma_C}(2\sigma_S)=\frac{\sigma_S}{\sigma_C},$$

and:

$$\frac{\partial\left(IR_2\left(\sigma_C\right)\right)}{\partial\sigma_C}=\frac{IR_2}{H\left(\varepsilon\right)}\frac{\partial H\left(\varepsilon\right)}{\partial\sigma_C}=\frac{IR_2}{H\left(\varepsilon\right)}\left[\frac{2}{\sqrt{\pi}}\exp\left(-\frac{\tau^2}{2\sigma_C^2}\right)\right]\left[\frac{\tau}{\sqrt{2}}\left(-\frac{1}{\sigma_C^2}\right)\right].$$

3.2.4 System of Gating Functions for Off-Nadir Models

The general gating system to be used to retrieve time delay, surface reflectivity and roughness, can be written as reported in following equation (67):

$$\begin{cases}\dfrac{\partial\left(IR\left(\varepsilon\right)\right)}{\partial t_0}=\dfrac{\partial\left(IR\left(\varepsilon\right)\right)}{\partial\varepsilon}\dfrac{\partial\varepsilon}{\partial t_0}=\left[\dfrac{\partial Y(\varepsilon)}{\partial\varepsilon}\dfrac{\partial\varepsilon}{\partial t_0}H(\tau)+Y(\varepsilon)\dfrac{\partial H(\tau)}{\partial t_0}\right]\\ \dfrac{\partial\left(IR\left(\sigma^0\right)\right)}{\partial\sigma^0}=\dfrac{IR}{\sigma^0}\\ \dfrac{\partial\left(IR\left(\sigma_S\right)\right)}{\partial\sigma_S}=\dfrac{IR}{H\left(\varepsilon\right)}\dfrac{\partial H\left(\varepsilon\right)}{\partial\sigma_C}\dfrac{\sigma_S}{\sigma_C}=\dfrac{IR}{H\left(\varepsilon\right)}\left[\dfrac{2}{\sqrt{\pi}}\exp\left(-\dfrac{\tau^2}{2\sigma_C^2}\right)\right]\left[\dfrac{\tau}{\sqrt{2}}\left(-\dfrac{1}{\sigma_C^2}\right)\right]\dfrac{\sigma_S}{\sigma_C}\end{cases}$$

In order to solve for the MLEs of interest parameters, it is possible to implement an iterative cycle using, at first attempt, initial values of variables which could be derived from the following expressions:

- the centre of gravity (COG), related to the time delay of the average surface:

$$\hat{t}_0=\frac{\int\tau\cdot g\left(\tau\right)\cdot d\tau}{\int g\left(\tau\right)\cdot d\tau}\qquad(68)$$

- the amplitude, related to the surface reflectivity:

$$\hat{a}=\frac{\left(\int g\left(\tau\right)\cdot d\tau\right)}{\hat{d}_t}\qquad(69)$$

- the pulse duration, related to the surface roughness:

$$\hat{d}_t = \frac{\left(\int g(\tau)\cdot d\tau\right)^2}{\int g^2(\tau)\cdot d\tau} \qquad (70)$$

- the dispersion, which allows the discrimination between two close echoes:

$$\hat{\alpha} = \sqrt{\frac{\int \tau^2 \cdot g(\tau)\cdot d\tau}{\int g(\tau)\cdot d\tau} - \hat{t}_0^2} \qquad (71)$$

where $g(\tau)$ is the received integrated echo waveform.

This iterative procedure is convergent if the first attempt value of any parameter to be estimated (e.g. MLE first step) is close to the right value. If not, it may converge towards a local maximum or may not to converge at all.

3.2.5 Model Implementation and Results

The results of the models implementation [models described by equations (58) and (67)] are reported in section 3.3.3, in order to compare both the off-nadir models performance.

3.3 Off Nadir IR Algorithm by Prony's Method

The assumption made in section 3.2 implies that the model (asymptotic model) described by equation (57) can be applied only in case of pointing angle greater than θ_{3dB} (asymptotic condition).

In order to obtain an equation valid for pointing angle comparable with θ_{3dB}, in the following sections it is described the application of the Prony's method in order to approximate the PFS function. This approach entails approximating the flat surface response by a series of exponentials using Prony's method (see APPENDIX A – Prony's Approximation Method). For each exponentials term in the series, the convolution can be integrated in closed form. The evaluated model allows for evaluation of Impulse Response in case off "near" off-nadir pointing angles. This model will be selected in processing chain if the off nadir angle will be greater than a selected threshold angle.

3.3.1 Near Off-Nadir IR Evaluation

For the altimeter heights and ranging times of interest the following relation subsists [4]:

$$\varepsilon^2 = \frac{c\tau}{h\left(1+\frac{h}{R_T}\right)} << 1$$

and the expression of PFS can be rewritten as follows:

$$P_{FS}(\tau) = \frac{G_0^2\lambda^2 c\sigma^0(\psi_0)}{4(4\pi)^2 L_p h^3}\exp\left(-\frac{4\varepsilon^2}{\gamma}\left(1+\frac{\beta}{2}\right)\right)I_0\left(\frac{2\beta\varepsilon^2}{\gamma}\right) \qquad \tau \geq 0 \tag{72}$$

where the $I_0(\cdot)$ is the modified Bessel function of the second kind. The followed approach entails approximating the Bessel function by a series of exponentials using Prony's method (see **[7]**). For each exponential term in the series, the convolution can be integrated in closed form to yield a rather simple function of exponentials. This method uses a variation of the covariance method of autoregressive modelling to find the denominator coefficients and then finds the numerator coefficients for which the impulse response of the output filter with numerator order *n* matches exactly the first *n* + 1 samples of given sequence.

The approximated Bessel function is given by:

$$I_0(x) \approx \sum_{i=1}^{N} C_i \exp[a_i x] \qquad (73)$$

where $x = \frac{4}{\gamma}\sin(2\xi)\cdot \varepsilon^2$.

For N≥2 we obtain:

$$P_{FS}(\tau) \approx \exp[-K_a \tau]\cdot \sum_{i=1}^{N} C_i \exp[K_i x] \qquad (74)$$

where:

$$K_a = \frac{4}{\gamma}\cos(2\xi)\frac{c}{h\left(1+\frac{h}{R_T}\right)}, \quad K_i = \frac{4}{\gamma}\sin(2\xi)\frac{c}{h\left(1+\frac{h}{R_T}\right)}\cdot a_i$$

It is worth noting that, in order to perform the implementation of Prony's method it needs a greater samples number (into the received echo), therefore during implementation phase it is possible to use over-sampling factor to evaluate the expansion coefficients C_i and a_i.

When the approximate form of flat surface response and relative expansion coefficients have been calculated, the Impulse Response can be evaluated. Hence the IR can be obtained by the convolution of (74) with Gaussian function as described in:

$$IR(\tau) = P_{FS}(\tau) * \exp\left[-K_C \tau^2\right] \qquad (75)$$

where $K_C = \frac{1}{2\sigma_C^2}$.

By using the Prony's method the IR can be rewritten:

$$IR(\tau) = \sum_{i=1}^{N} IR_i \qquad (76)$$

where:

$$IR_i(\tau) = C_i \exp[-K_a\tau]\exp[K_i\tau] * \exp[-K_C\tau^2] \tag{77}$$

Solving the convolution (75), the IR expression becomes:

$$IR_i(\tau) = \int_0^\infty C_i \exp[\overline{K}_i\tau]\exp[-K_C(t-\tau)^2]d\tau =$$

$$= \exp[K_C t^2]\cdot\int_0^\infty C_i \exp[-K_C\tau^2]\exp\left[-2\left(-\frac{\overline{K_i}}{2} - K_C t\right)\tau\right]d\tau$$

By using Abramowitz and Stegun integration method (see **[6]**), the last equation becomes:

$$IR_i\Big|_{\text{Prony}}(\tau) = \frac{1}{2}\sqrt{\frac{\pi}{K_C}}C_i \exp\left[\overline{K_i}t\right]\exp\left[\frac{\overline{K_i}^2}{4K_C}\right]\cdot\left[1 + erf\left(\frac{\overline{K_i} + 2K_C t}{\sqrt{K_C}}\right)\right] \tag{78}$$

where $\overline{K}_i = K_i - K_a$ .The equation (78) describes the IR in case of pointing angle comparable with θ_{3dB}.

3.3.2 Evaluation of Gating Functions for Off-Nadir Prony Model

The derivative of the equation (78) with respect to t_0 can be written as:

$$\frac{\partial IR}{\partial t_0} = \sum_{i=1}^{NN} \frac{\partial IR_i}{\partial t_0}$$

where:

$$\frac{\partial IR_1}{\partial t_0} = C_i \cdot \overline{K}_i \exp[K_i t]\cdot \exp\left[\left(\frac{K_i}{2\sqrt{K_C}}\right)^2\right]\cdot$$

$$\cdot\left\{\left[1 + erf\left(\frac{K_i}{2\sqrt{K_C}} + \sqrt{K_C}\cdot t\right)\right] + 2\sqrt{\frac{K_c}{\pi}}\cdot\exp\left[-\left(\frac{K_i}{2\sqrt{K_C}} + \sqrt{K_C}\cdot t\right)^2\right]\right\}$$

We can include the spherical surface effects by considering (as described in

[4]):

$$\bar{\tau} = \frac{t - t_0}{\left(1 + \frac{h}{R_{Tit}}\right)}$$

Thus the time gating function for off-nadir Prony model is given by following equation (78.1):

$$\frac{\partial IR|_{\Pr ony}}{\partial t_0} = \sum_{i=1}^{NN} \frac{\partial IR_i}{\partial t_0} = -\frac{1}{2}\sqrt{\frac{\pi}{K_c}} \exp[-K_a t] \cdot \sum_{i=1}^{NN} C_i \cdot \overline{K}_i \exp[K_i t] \cdot \exp\left[\left(\frac{K_i}{2\sqrt{K_C}}\right)^2\right] \cdot$$

$$\cdot \left\{\left[1 + erf\left(\frac{K_i}{2\sqrt{K_C}} + \sqrt{K_C} \cdot t\right)\right] + 2\sqrt{\frac{K_C}{\pi}} \cdot \exp\left[-\left(\frac{K_i}{2\sqrt{K_C}} + \sqrt{K_C} \cdot t\right)^2\right]\right\}$$

3.3.3 Model Implementation and Results

An example of fitting of Cassini LBDR data from Ta fly-by (burst #14331) with the off-nadir model previously described is reported in the following. The ML estimator is initialized with the values of COG position (i.e. $t_0 \cdot f_c$=500) and signal amplitude. The analytical values used at first attempt ensure the convergence within a limited number of steps.

The results of the iterative cycle are shown in the following Figure 34 and Figure 35 for the first and the last step of the process, respectively.

An example of fitting of real data (burst # 14364), after the application of the MLE algorithm, with both nadir and off-nadir models is reported in Figure 36, in order to evidence the differences in between.

In order to obtain the order of magnitude of the variance in the estimate of the COG position, these subsequent steps have been followed:

1) burst # 14364 has been selected
2) simulated waveform (see Figure 37) has been obtained by adding a white gaussian thermal noise to the model
3) the average of the 15 pulses within the burst has been performed in order to reduce the noise in individual pulses
4) the ML estimator has been run *N* times (see Figure 38)
5) the variance (in pixels) of the *N* estimates of the centroid position has been evaluated.

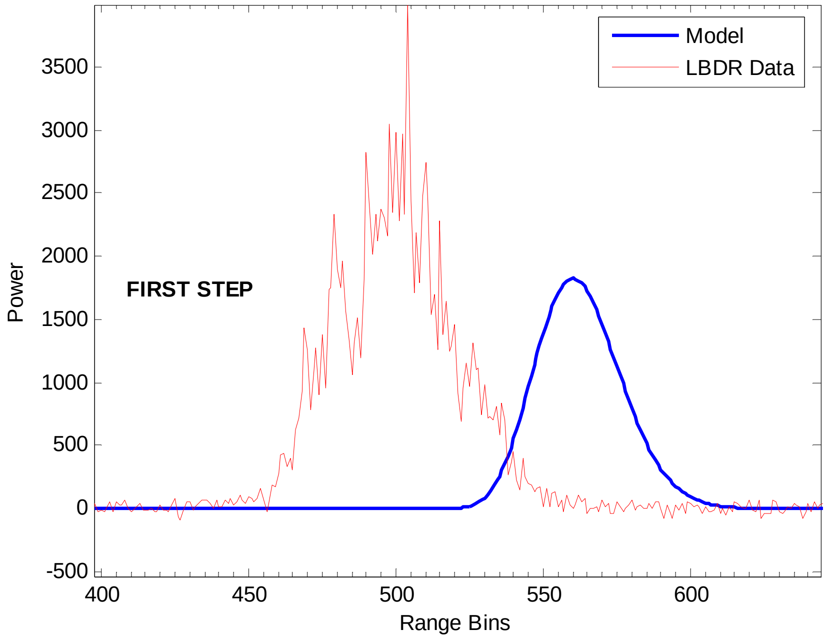

Figure 34 – MLE *first step* (ξ =0.8908°, $\boldsymbol{h}$ =5083.2 km)

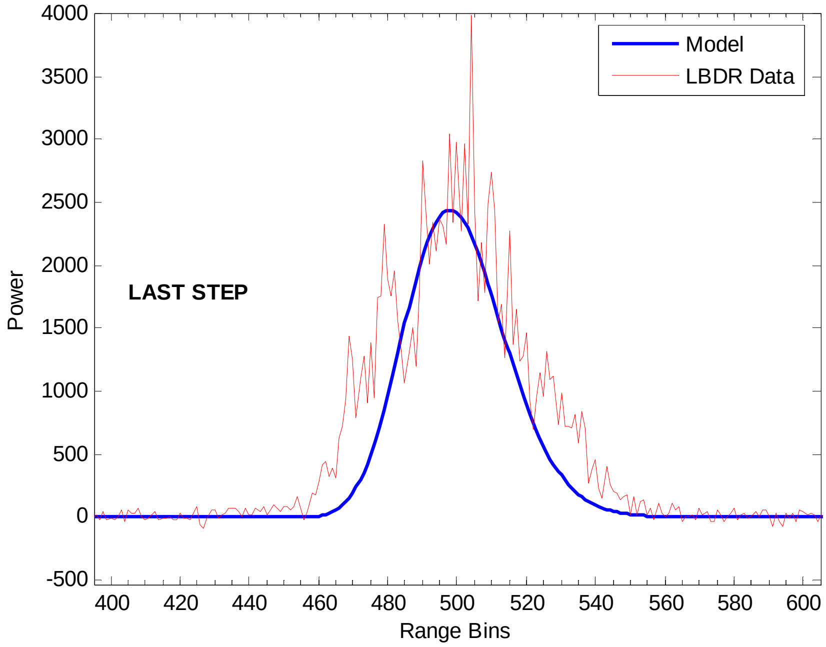

Figure 35 – MLE *last step* (ξ =0.8908°, $\boldsymbol{h}$ =5083.2 km)

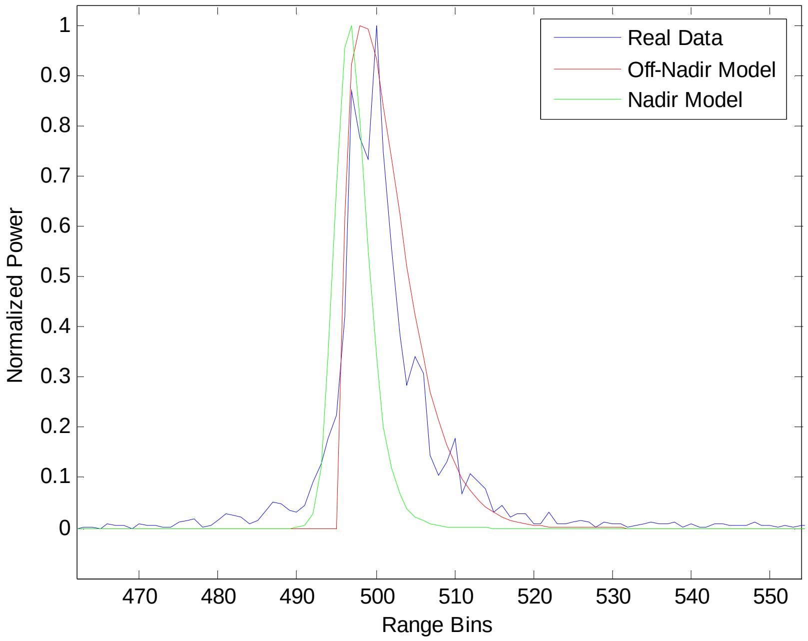

Figure 36 – Fitting of models with LBDR data (ξ =0.23°, $\boldsymbol{h}$ =5500 km)

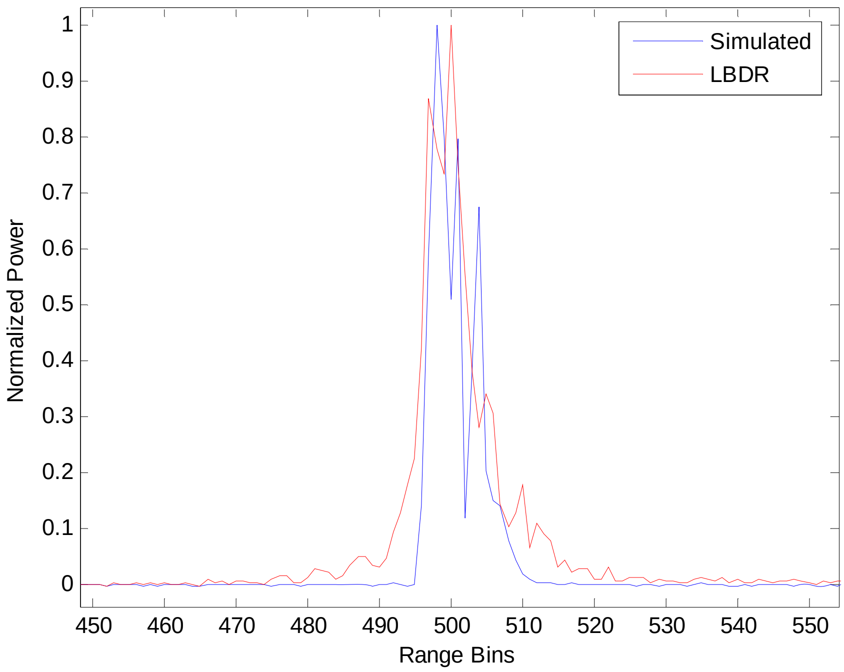

Figure 37 – Fitting between simulated and real echo waveforms (ξ =0.23°, $\boldsymbol{h}$ =5500 km)

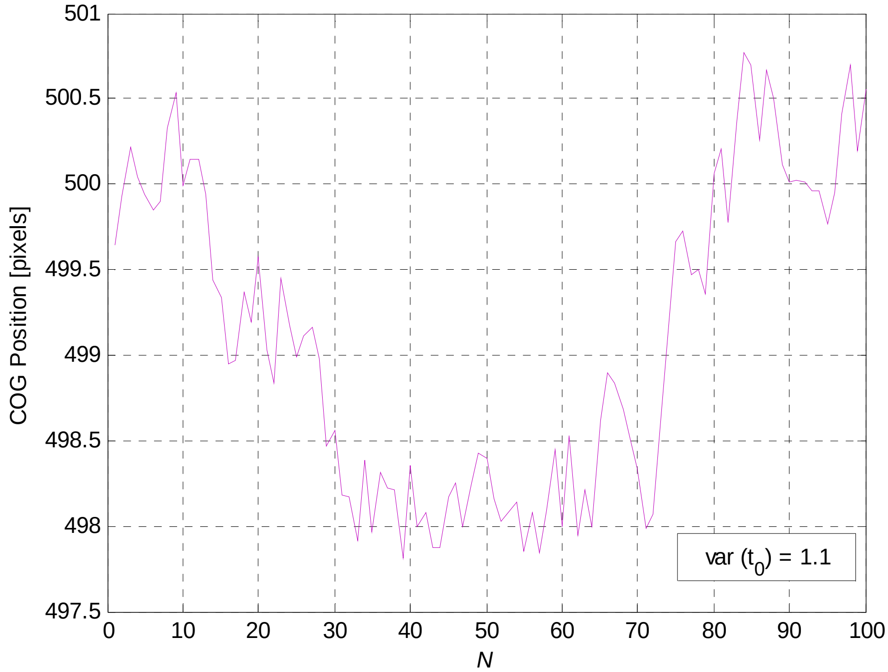

Figure 38 – Estimations of COG position over N=100 runs (burst # 14364)

3.4 Interferometric Approach

A technique suited to synthesise altimeter beam or multiple beams is based on a two interferometer elements. This is a concept widely used in radioastronomy where interferometry is used for receiving radiation from celestial radio objects as they drift across the sky through the antenna pattern. The detection and location of the objects are facilitated by the small beamwidths of the lobes of the pattern. The technique is known either as two-dish interferometry or amplitude interferometry.

Figure 39 shows the involved geometry, where the two antennas are separated by a distance d in the cross track direction and have an off-nadir angle ξ.

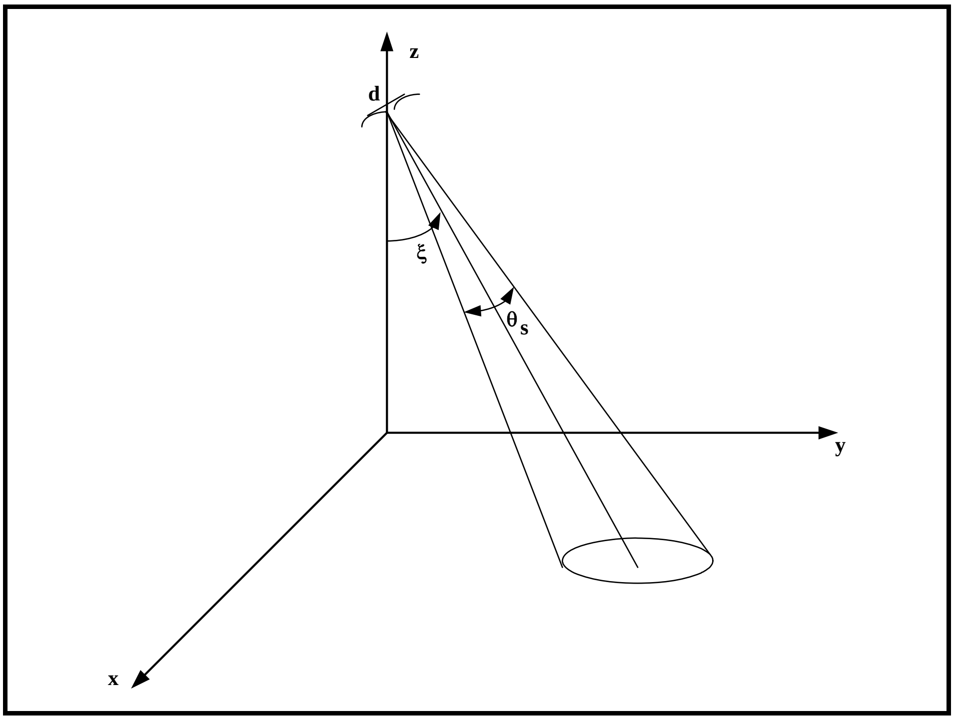

Figure 39 – Interferometric Approach Geometry

The composite antenna pattern is a product of the pattern of the individual antennas and the so called array factor. The resulting expression for the composite antenna pattern is a rather complicated function of geometry. To simplify azimuthal integration in the expression for the FSIR, certain large parameters are used in the system description. However, unlike the asymptotic evaluation presented in equation (54), the proper technique to evaluate the FSIR integral must be selected. That is, if the pattern of each antenna element is dominant, Laplace's method should be used. However, if the array factor is dominant, stationary phase should be the method of approximation. The selection can be based on the relative magnitude of k_0d compared to $(4/\gamma)sin(2\xi)$. The former represents the dominance of the array factor while the latter represents the individual antenna element. Thus, if:

$$k_0 d > (4/\gamma) sin(2\xi) >> 1 \qquad (79)$$

then the integration can be accomplished by using the stationary phase approximation, while if the inequality is reversed Laplace's method should be used. In any case, either or both of these parameters must be large compared to unity, for using asymptotic integration techniques.

The stationary phase method leads to the following approximate expression (80) for the FSIR when using the two element interferometer:

$$P_{FS}(\tau) \approx \frac{G_0^2 \lambda^2 \sigma^0(\psi_0)c}{2(4\pi)^3 L_p h^3} 6\sqrt{\frac{2\pi}{a+b}} \exp\left(-\frac{4}{\gamma(1+\varepsilon^2)}(\sin(\xi)-\varepsilon\cos(\xi))^2\right)$$

$$\left\{\sqrt{\frac{a+b}{2k_0 d|q''(0)|}}\left[\begin{array}{l}\frac{1}{3}\cos\left(\frac{2k_0 d}{(1+\varepsilon^2)^{1/2}}(\sin(\xi)-\varepsilon\cos(\xi))+\frac{\pi}{4}\right)+ \\ \frac{4}{3}\sqrt{2}\cos\left(\frac{k_0 d}{(1+\xi^2)^{1/2}}(\sin(\xi)-\varepsilon\cos(\xi))+\frac{\pi}{4}\right)\end{array}\right]+1\right\} \quad \tau \geq 0$$

where:

$$q''(0) = \frac{\varepsilon}{(1+\varepsilon^2)^{1/2}}\left(\cos(\xi)+\frac{sin(\xi)-\varepsilon\cos(\xi)}{(1+\varepsilon^2)}\right) \quad (81)$$

This result can be converted to the actual average return waveform (IR) by making the convolution of (80) by either the height probability density $P_s(\tau)$ and the system pulse $P_p(\tau)$ functions, provided that the lobes in (80) are much wider than these two functions.

The following Figure 40 and Figure 41 show some evaluations of FSIR for various values of off-nadir angle and baseline.

From the analysis of (80) it is evident that, when also the (54) holds, i.e. when the bound (56) is satisfied, the FSIR for the interferometric case is the product of the FS response of a single antenna multiplied by an oscillating term composed by two cosine function with different period. This is due to the array factor of the interferometer that, by indicating with ϕ the angle with respect the antennas broadside, can be written as:

$$F(\phi) = 2\cos\left(k_0 \frac{d}{2}\sin\phi\right) \quad (82)$$

The direction of grating lobes ϕ_g^n is the solution of the following equation:

$$\phi_g^n = \sin^{-1}\left(n\frac{\lambda}{d}\right) \quad n = ...-1,0,1,..... \quad (83)$$

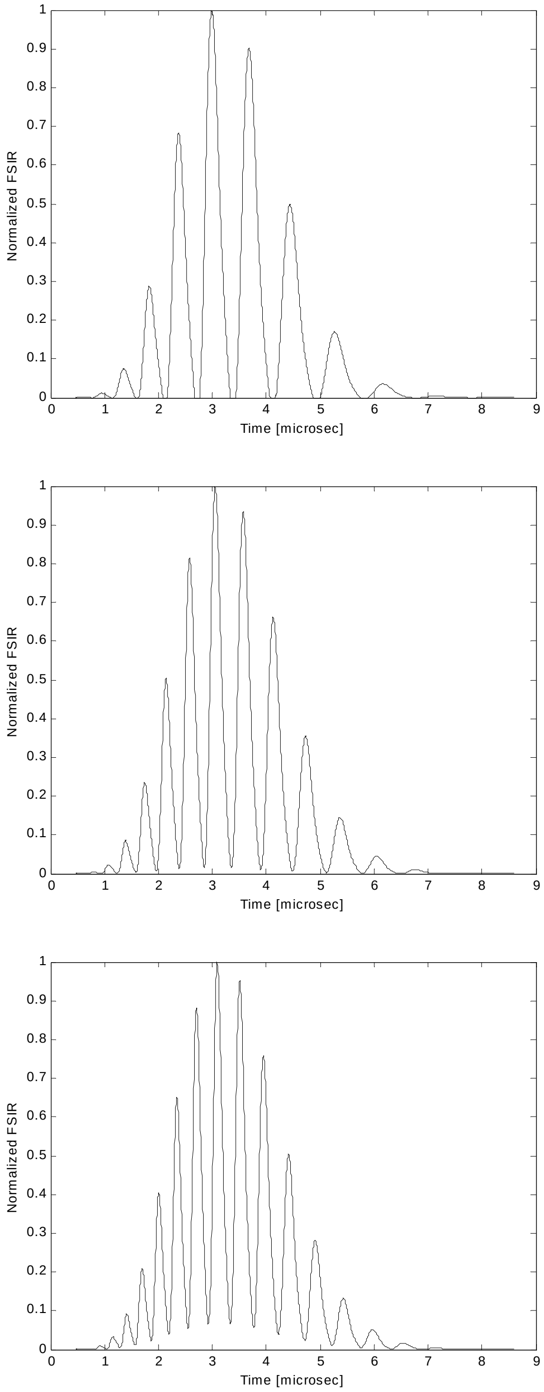

Figure 40 – FSIR for the interferometric configuration for baseline values of (from up to down) 6, 8 and 10 meters.

($\lambda = 2.22$ cm $\xi = 2°$ $\theta_{CSB} = 1°$)

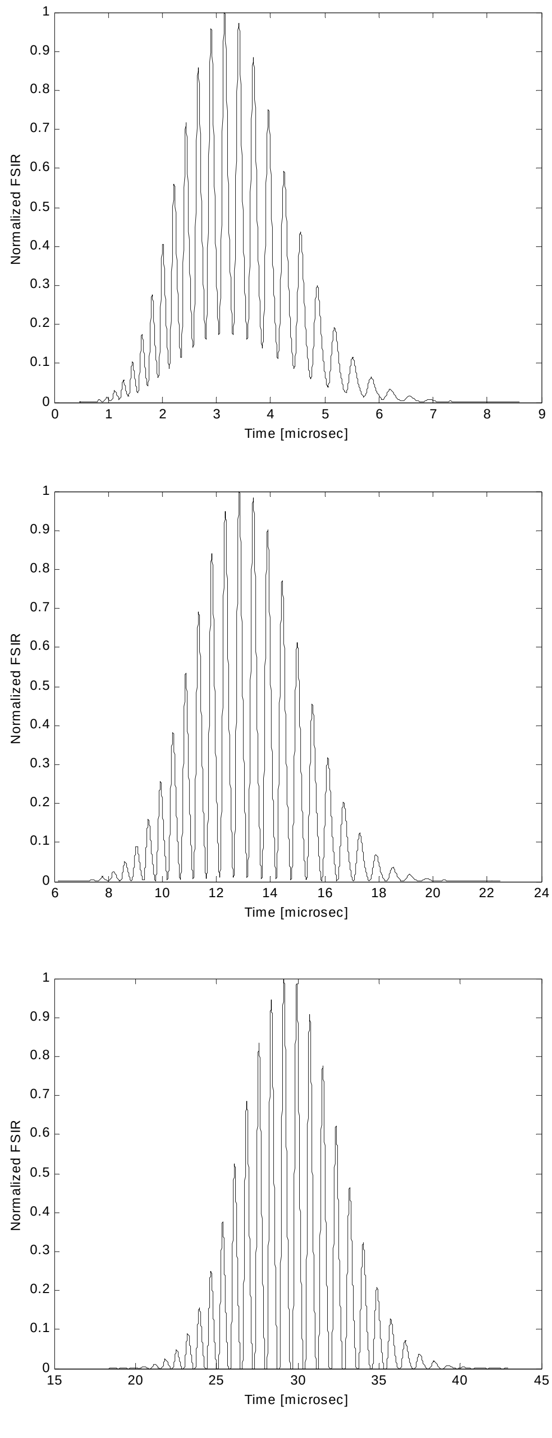

Figure 41 – FSIR for the interferometric configuration for off-nadir angle values of (from up to down) 2, 4 and 6 degrees.

$(\lambda = 8.3 \text{ mm } \mathrm{d} = 6 \ m \ \theta_{\mathrm{CSB}} = 1°)$

Therefore it is possible to evaluate the number of lobes (N_g^n) within the antenna aperture of the single antenna (θ_B) by:

$$N_g^n = \mathrm{int}\left(2\frac{d}{\lambda}\sin\left(\frac{\theta_B}{2}\right)\right) \quad (84)$$

Of course by increasing the ratio between the interferometer length and the wavelength the number of grating lobes increases as well, as shown by Figure 43.

The 3-dB aperture of the *n-th* beams (ϕ_3^n) can be evaluated by:

$$\left|F\left(\phi_g^n + \frac{\phi_3^n}{2}\right)\right| = \frac{\left|F\left(\phi_g^n\right)\right|}{\sqrt{2}} \quad (85)$$

that is equivalent to:

$$\phi_3^n = 2\left|\sin^{-1}\left(\frac{\lambda}{4d}\right) - \phi_g^n\right| \quad (86)$$

that states that the 3-dB aperture of the beams improves as $|n|$ decreases as shown in Table 4 where the first 5 beams have been considered and they have been adequately spaced in order to assure a cross-track sampling less than 10 Km. In this way the corresponding resolution can be evaluated by applying the same relation used for the single beam off-nadir case, i.e. (6) or (7), taking the new values of aperture for each beam. Similarly the accuracy can be evaluated by means of (17) by evaluating the new values of aperture and averaged impulse width for each beam.

Baseline/wavelength	**84**				
Lobe position w.r.t. broadside [deg]	-1.34	-0.67	0	0.67	1.34
3-db aperture [deg]	3.0158	1.6753	0.3351	1.0052	2.35
Baseline/wavelength	**96**				
Lobe position w.r.t. broadside [deg]	-1.19	-0.60	0	0.60	1.19
3-db aperture [deg]	2.69	1.49	0.30	0.90	2.09
Baseline/wavelength	**120**				
Lobe position w.r.t. broadside [deg]	-0.96	-0.48	0	0.48	0.96
3-db aperture [deg]	2.15	1.19	0.24	0.72	1.67

Table 4 - Parameters for some interferometric configuration

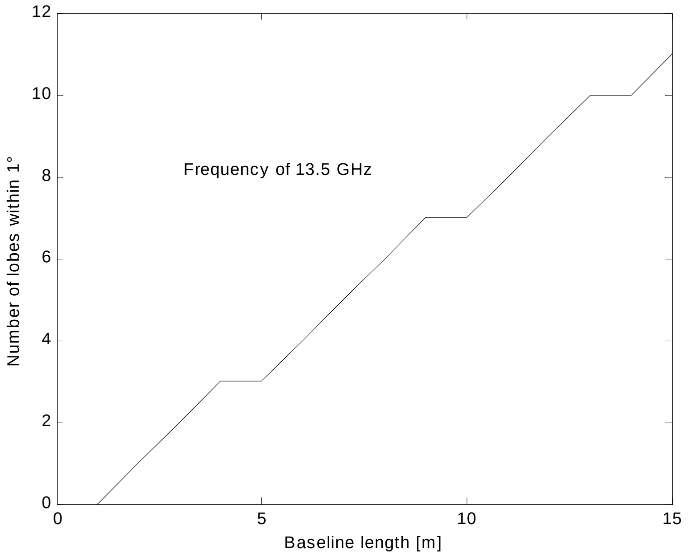

Figure 42 – Number of lobes within a specified aperture

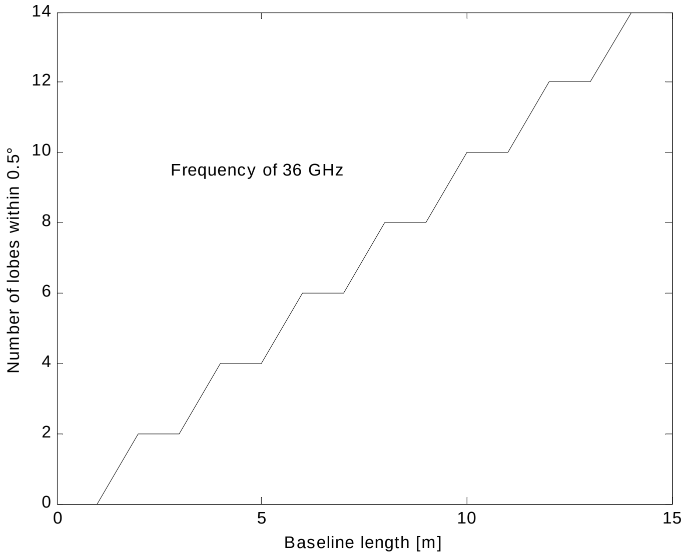

Figure 43 – Number of lobes within a specified aperture

3.5 Altimeter Models Validation Algorithm

3.5.1 Simulation Algorithm

In order to validate the models described by equations (63) and (78) an algorithm simulating the performances of the Radar Altimeters has been developed. The algorithm is based on selection of the values to be used for any model evaluation, by choosing among:

- Spacecraft Altitude
- Off-nadir Angle
- Surface Roughness
- Surface Topography
- Radar properties: chirp Band, pulse length, carrier frequency, beamwidth, etc

Starting from the above selected values, the models are evaluated as described in sections 3.2 and 3.3. Computed waveforms represent the altimeter performance with reference to the operative conditions selected. Then, random noise it is generated in order to simulate the speckle that is overlapping to received echoes. The simulated speckle is random noise (white noise) with predefined power level and with time series exponential distribution. The output of this simulation's step is a model of exponential noise distribution that is then overlapped to waveforms, previously evaluated, in order to obtain the simulation of a range compressed pulse. Figure 44 depicts the range compressed data simulation algorithm.

The next step in simulation phase is to model the target surface. In case of altimeter this means to simulate the shape of the sensed surface, that is their topography. The topography is simulated by generating autocorrelated array of heights with autocorrelation function exponential or Gaussian.

The last step, in this algorithm, is to correlate simulated pulse compressed echoes and the corresponding topography. This is done taking into account the observation geometry and the radius of the satellite orbit. Topographic heights are used to evaluate the two-way time delay for each pulse and the position of relative pulses centroid. Simulated echoes are centered, into their acquisition window, by using the relative centroid position previously computed.

The main simulation algorithm steps can be summarized as follows:

1) Identification of operational Scenario
2) Evaluation of the related waveforms
3) Simulation of the speckle
4) Overlap of the speckle and waveforms in order to obtain simulated range compressed data
5) Simulation of the topography
6) Correlation (in terms of time-delay) between the centroids of range compressed data and the topography

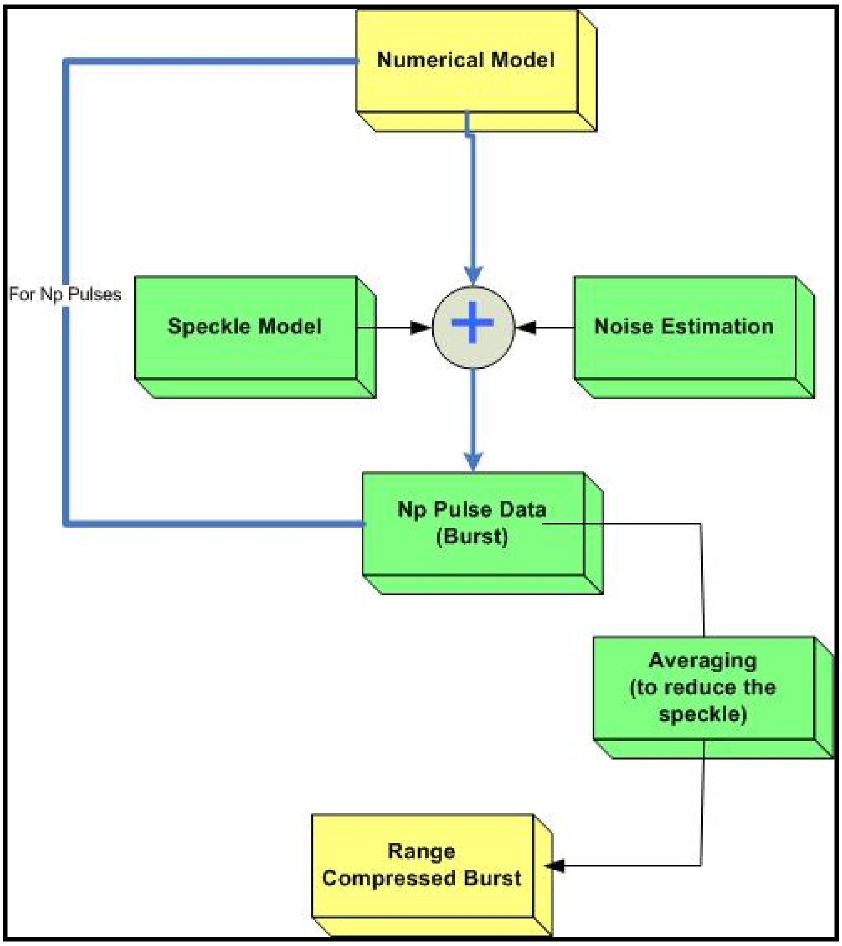

Figure 44 – Range Compressed Data Simulation Algorithm

The core of the validation algorithm consists in following checks:

1. to check the best fitting (in statistical sense) of the models and simulated range compressed data
2. to check the correlation (and the rms errors) between the simulated topography and estimated topography (by MLE algorithm described in section 3.1.3).

In order to finalize the validation algorithm it is needed to apply the MLE algorithm, as described in section 4.3, by using, in input, simulated range compressed data. Figure 45 depicts the main validation algorithm steps. The results of the waveforms evaluation have been previously reported in sections 3.1.5, 3.2.5 and 3.3.3. The following figures show the output of simulation steps for the Cassini specific case study.

In details, bursts of 15 pulses have been simulated (see Figure 46 to Figure 49) with an off-nadir value linearly variable into the range [0.05, 1] degrees. Figure 50 shows the waveform model computed for ξ=0.3 deg. and Figure 49 depicts the effect of the speckle simulation. In this specific simulation, the pseudo-code, showing the algorithm approach, is reported in the following:

```
for ii=1:N_burst   %number of burst
    Np=15;              % number of pulses per burst
    for k=1:Np        %number of pulses per burst
        modello_speckle=exprnd(modello);   %speckle modelling
        noise = exprnd(amp/20,1,length(tau));  %noise modelling
        x(k,:)=modello_speckle+noise;  %noise overlapping
    end
      dati=mean(abs(x),1); %burst averaging
end
```

Simulated topography is depicted in Figure 52. It is worth noting that the estimation errors, at the end of MLE algorithm, is less than Radar vertical resolution (30m), as showed in Figure 53 and Figure 54.

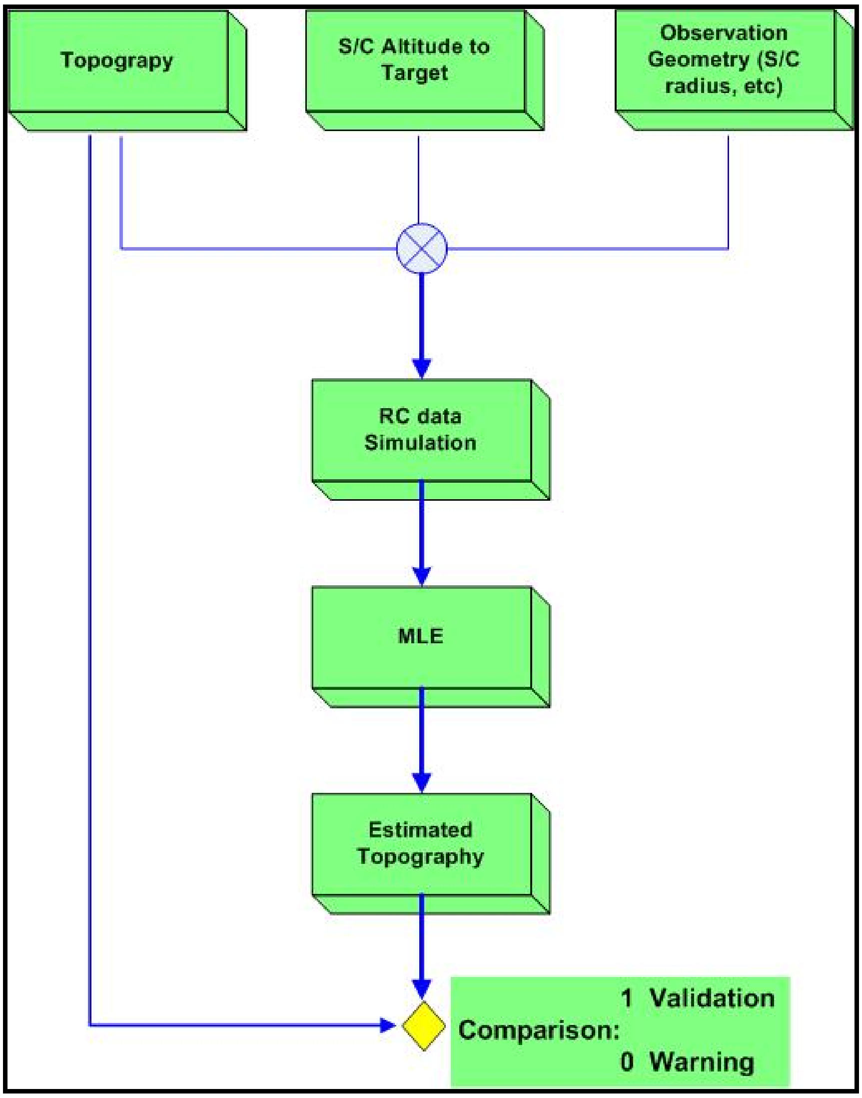

Figure 45 – Models Validation Algorithm

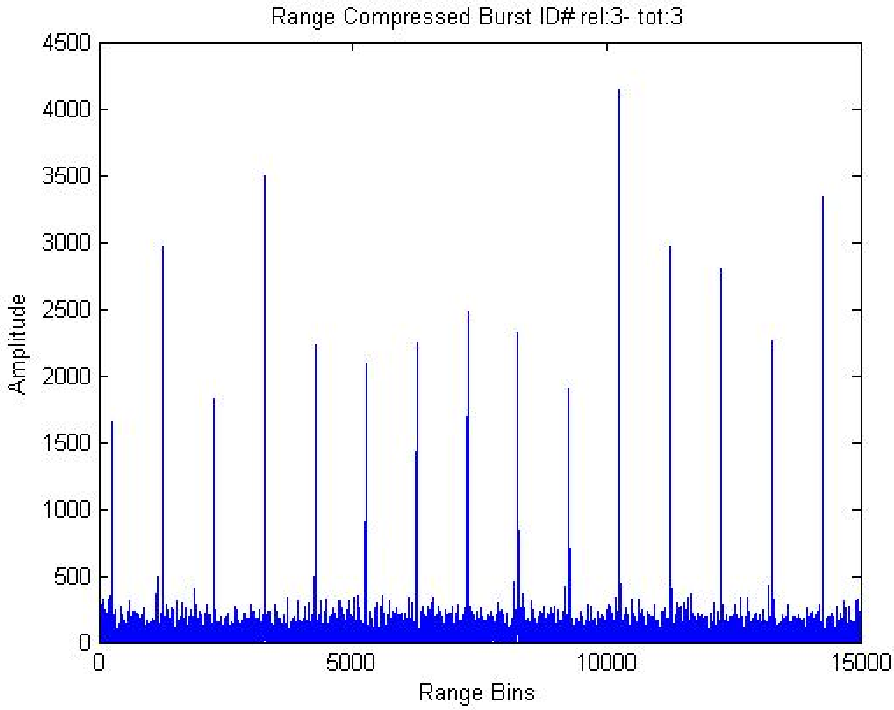

Figure 46 – Simulated Range Compressed Burst

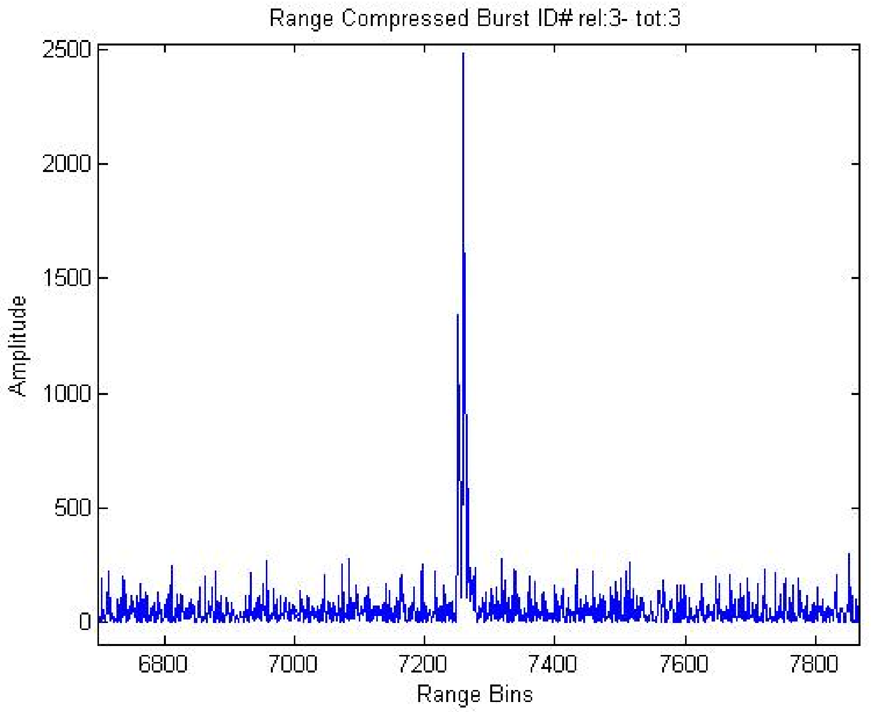

Figure 47 – Simulated Range Compressed Burst: Pulse Zoom In

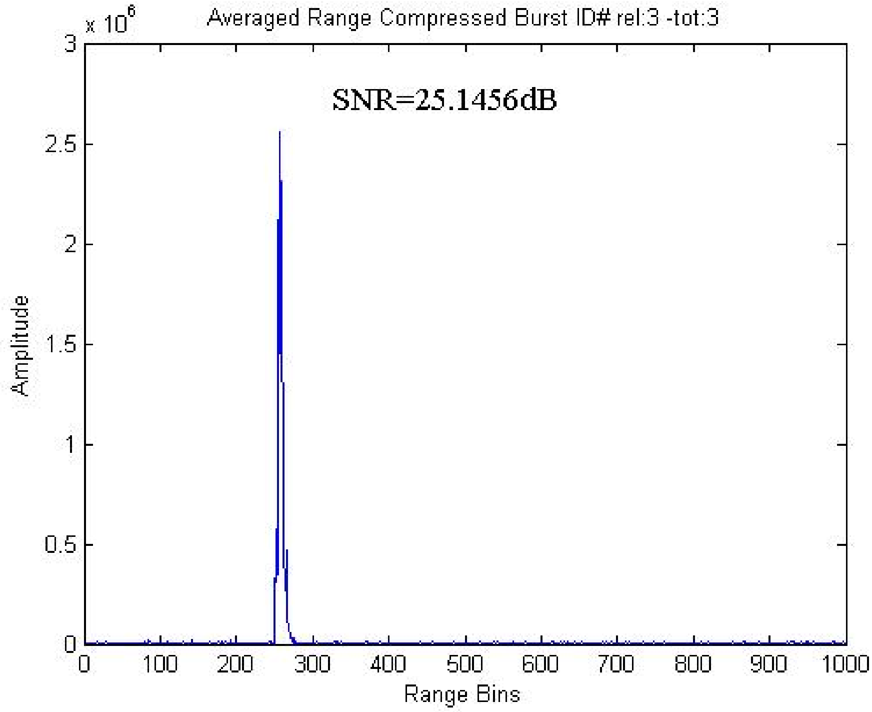

Figure 48 – Averaged Range Compressed Burst

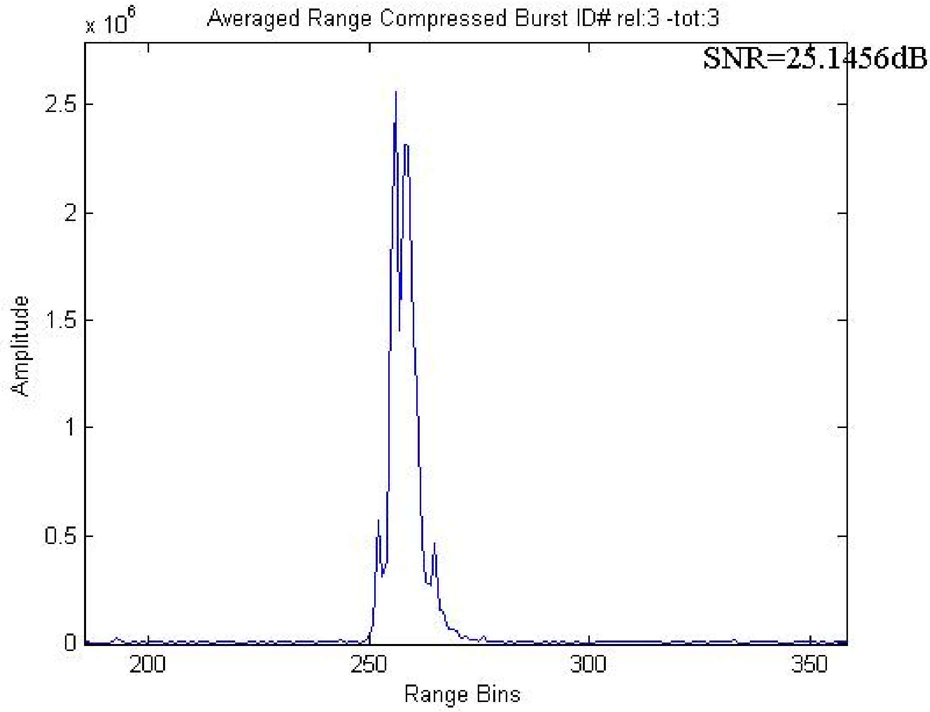

Figure 49 – Averaged Range Compressed Burst: Zoom In

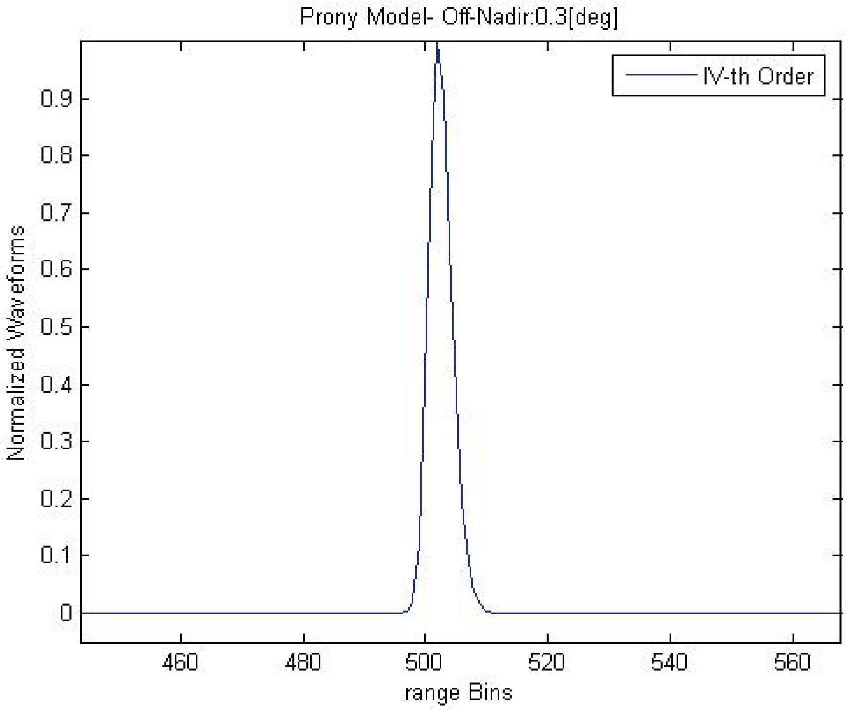

Figure 50 – Example of Evaluated Waveform

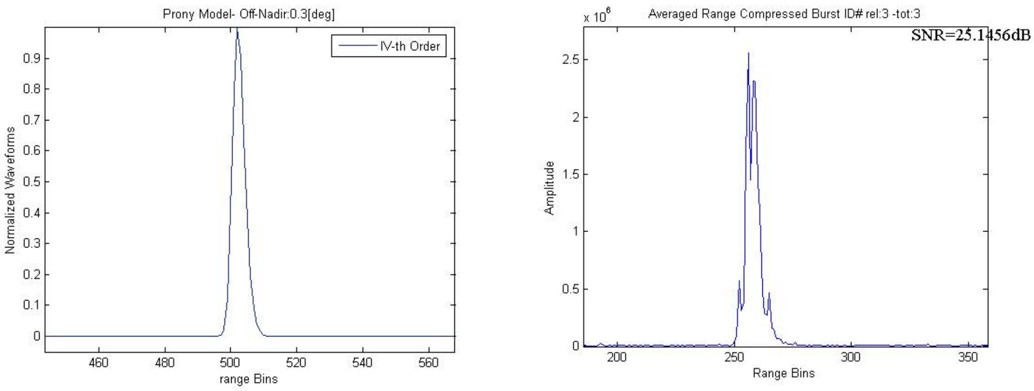

Figure 51 – Comparison between evaluated waveform (left) and waveform simulating the speckle

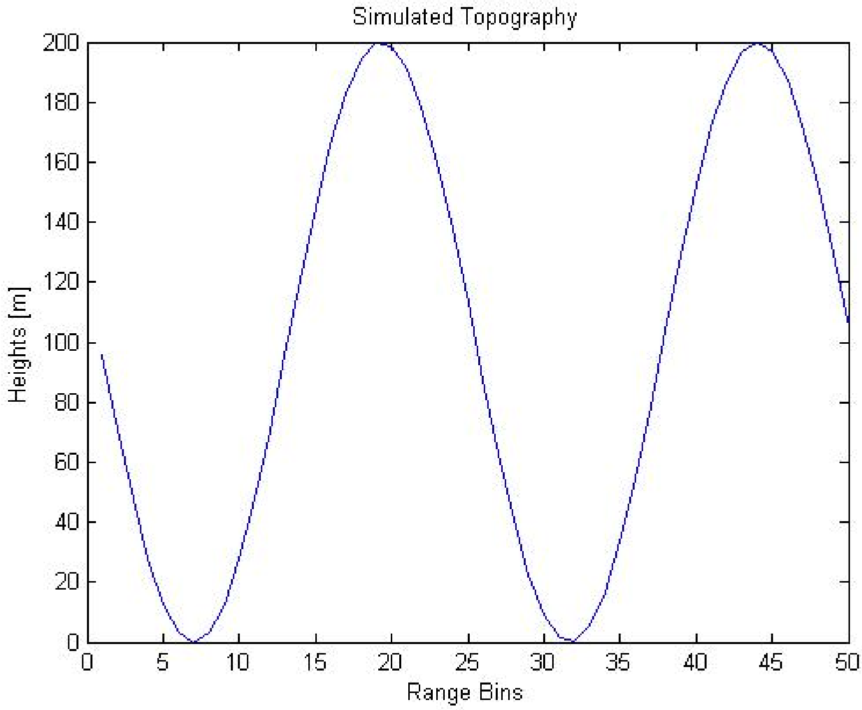

Figure 52 – Example of Simulated Topography Shape

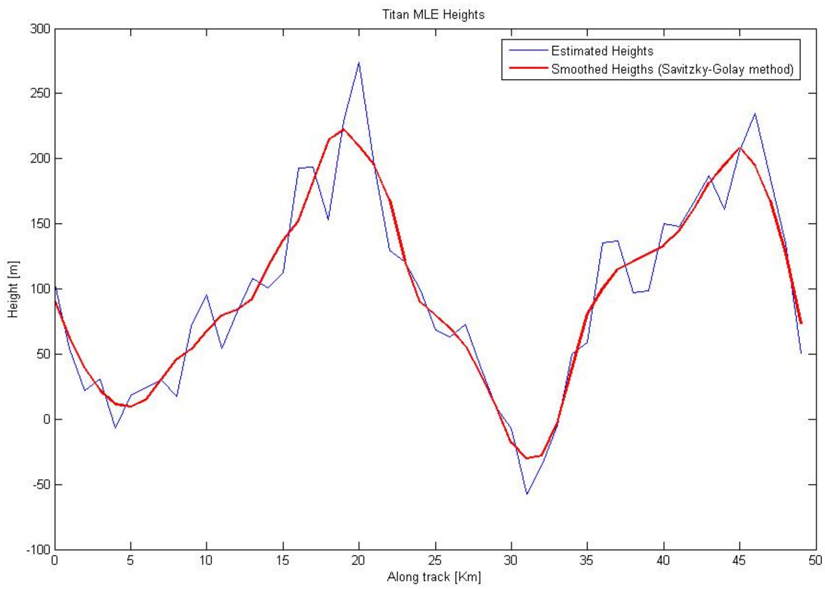

Figure 53 – Estimated Topography

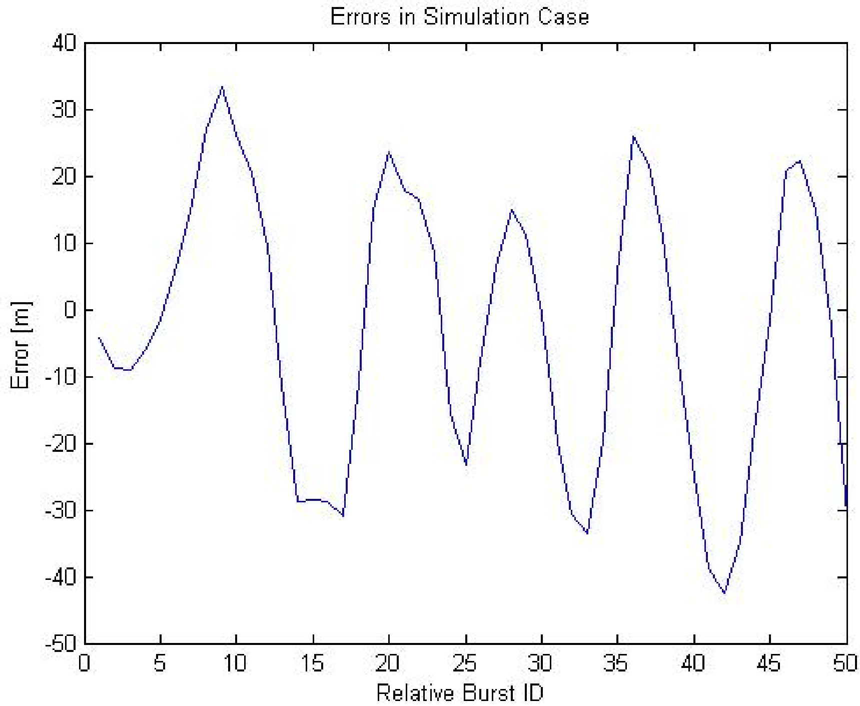

Figure 54 – Error in meters: *[(Simulated Topography-Estimated Topography)]*

3.5.2 Comparison with numerical solutions

A different approach to validate the off-nadir models [described in equations (63) and (78)] is represented by the direct comparison versus the numerical integration of the convolutional form (see [2]) expressed in equation (20).

The following Figure 55 shows the errors (in percentage) between the equations (63) and (78) and the numerical integration of the (20). The x-axis shows the off-nadir angle value (used in model evaluation), the y-axis shows the percentage errors.

It is evident that within the off-nadir range:

$$\xi \in]0, 0.37]\text{deg}$$

the equation (78), the Prony approximation model, ensures an error less than 2% respect to numerical solution. When the off-nadir value is greater than 0.37 degree, which is the range:

$$\xi \in]0.37, 2[\text{deg}$$

the equation (63), the asymptotic model, ensures an error less than 2% respect to numerical solution.

Tacking into account the above considerations it is possible to extract the applicability diagram, depicted in Figure 55, showing the applicable scenario for each model and relative errors.

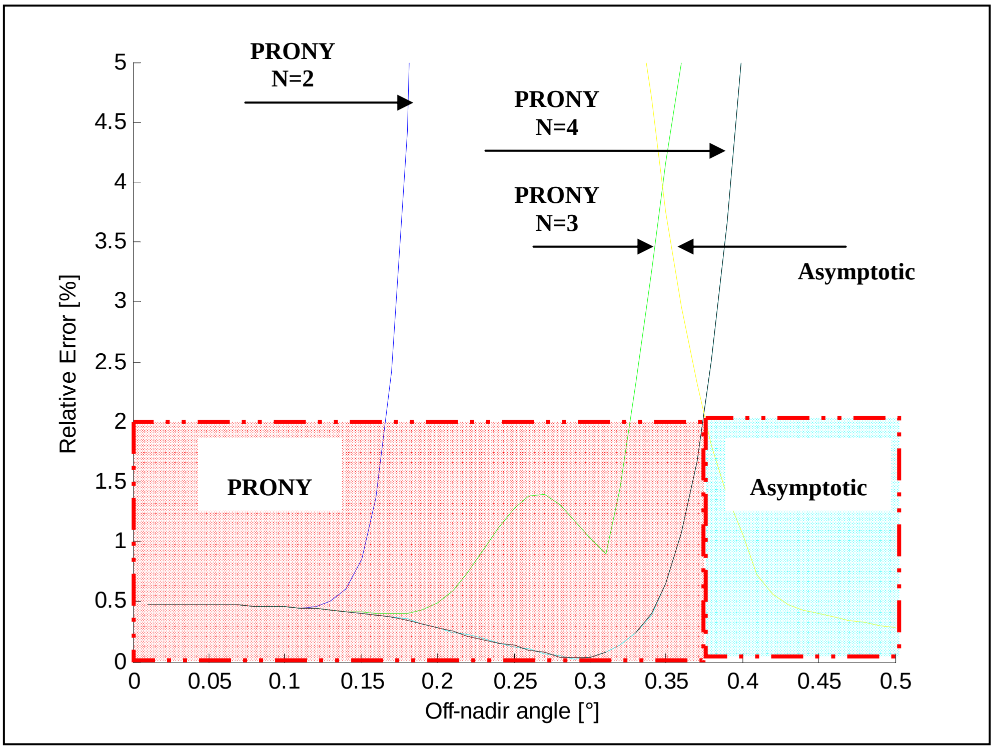

Figure 55 – Models Applicability Diagram

REFERENCES

[1] Elachi, C., Im, E., Roth, L.E., Werner, C.L., *"Cassini Titan Radar Mapper"*, Proceedings of the IEEE, Vol. 79 , Issue 6, Jun. 1991, pp. 867 - 880

[2] Montefredini, E., Morelli, F., Picardi, G., Seu, R., *"A non-coherent surface backscattering model for radar observation of planetary bodies and its application to Cassini radar altimeter",* Planet. Space Sci., Vol. 43, No. 12, 1995, pp. 1567-1577

[3] Brown, G.S, *"The average impulse response of a rough surface and its applications"*, Antennas and Propagation, IEEE Transactions on [legacy, pre-1988], Vol. 25, Issue 1, Jan. 1977, pp. 67-74

[4] Newkirk, M.H., Brown, G.S, *"Issues related to waveform computations for radar altimeter applications"*, Antennas and Propagation, IEEE Transactions on, Vol. 40, Issue 12, Dec. 1992, pp. 1478-1488

[5] Brown, G.S, *"A useful approximation for the flat surface impulse response"*, Antennas and Propagation, IEEE Transactions on, Vol. 37, Issue 6, Jun. 1989, pp. 764-767

[6] Abramowitz, M., Stegum, IA, Eds., "*Handbook of Mathematical Functions"*, New York: Dover Publications, 1972

[7] Bender, C.M., Orzag, S.A., *"Advanced Mathematical Methods for Scientists and Engineers",* New York: Mcgraw-Hill, 1978

[8] L.J. Bain, M. Engelhardt, "*Introduction to Probability and Mathematical Statistics"*, PWS-Kent Publishing co., 1992

[9] Azzalini, A. , "*Inferenza statistica, una presentazione basata sul concetto di verosimiglianza",* 2ª ed., Springer-Verlag, 2001

[10] Myung, J.I., Navarro, D.J. (in press) *"Information matrix"*, in B. Everitt & D. Howell (Eds.) "*Encyclopedia of Behavioral Statistics"*, Wiley

[11] G.S. Hayne, 1980, *Radar Altimeter Mean Return Waveforms from Near-Normal-Incidence Ocean Surface Scattering*, IEEE VOL. AP-28, N°5

[12] J.R. Jensen, 1999, *Radar Altimeter Gate Tracking: Theory and Extension*, IEEE, VOL. 7, N°2

[13] C.G. Rapley, H.D. Griffiths, 1990, "Proceeding of the Consultative Meeting on Imaging Altimeter Requirements and Techniques", University College London, ESA Referene MSSL/RSG/90.01

[14] Ulaby, Moore, Fung, 1982, *Microwave Remote Sensing: Active and Passive, VOL. II : Radar Remote Sensing and Surface Scattering and Emission Theory*, Addison Wesley Publishing Company, Inc.

[15] D.J. Wingham, Rapley, Griffiths, 1986, *New Techniques in satellite tracking systems*, IGARSS'86 Symp.Dig., VOL.I, pp.185-190

[16] D.B. Chelton, E.Walsh, 1989, *Pulse Compression and sea level tracking in Satellite Altimetry*, Journal of Atmosferic and Oceanic Tech., VOL.6, pp. 407-438

[17] D.W. Hancock, G.S. Hayne, R.L. Brooks, 2001, GFO Altimeter Engineering Assessment Report, The First 20 Cycles Since Acceptance, NASA TM-2002-209984/VER.1/VOL.III

[18] R.J. Jensen, R.K.Raney, 1996, *Multi-Mission Radar Altimeter: Concept and performance*, Proceedings IEEE International Geoscience and Remote Sensing Symposium IGARSS'96, Lincoln, Nebraska, USA, IEEE N°98CH36174, pp. 2011-2013

[19] R.K. Raney, 1995, *A Delay/Doppler Radar fot ice sheet Monitoring*, IEEE Geoscience & Remote Sensing Symposium IGARSS'95 Firenze, N°95CH35770, pp. 862-864

[20] C.G. Rapley, H.D. Griffiths, P.A.M. Berry, 1990, Proceedings of the Consultative Meeting on Imaging Altimeter Requirements and Techniques, University College London, ESA Reference MSSL/RSG/90.01

[21] F. Rémy, B. Legresy, P. Vincent, 1999, New *Scientific Opportunities from Ka-band Altimetry*, IGARSS'99, Symp. Dig., Hamburg, Germany

[22] C.H. Davis, H.J. Zwally, 1993, Geographic and Seasonal variations in the surface proprieties of the ice sheets by satellite radar altimetry, Journal of Glaciology, VOL.39, N°133, pp. 687-697

[23] G.Picardi, R.Seu, S.Sorge, 1998, Extensive Non Coherent Averaging In Doppler Beam Sharpened Space-Borne Radar Altimeters, Proceedings of Geoscience and Remote Sensing Symposium IGARSS'98, Seattle, USA, IEEE N° 98CH36174, pp. 2643-2645

[24] R.K.Raney, 1998, The Delay/Doppler Radar Altimeter, IEEE VOL. 36, N°5, pp. 1578- 1588

[25] C.H. Davis, 1992, Satellite Radar Altimetry, IEEE VOL.40, N°6, pp.1070-1076

[26] S.Barbarossa, P.T.Melacci, G.Picardi, R.Seu, 1990, A conceptual SAR/Altimeter Radar with Subsurface Capabilities for Space Missions, IEEE N° CH2882-9/90/0000-0076

[27] V.N. Zarkov, Struttura Interna della Terra e dei Pianeti, Editori Riuniti

[28] G. Franceschetti, R. Lanari, 1999, Synthetic Aperture Radar processing, CRC, Press

[29] G. Alberti, G. Salzillo, A. Moccia, Algoritmi per la produzione di immagini*,* CO.RI.S.T.A., www.corista.it

[30] Li Qi, S, Woodruff, D. Cartes, prony Analysis for Power System Transient Harmonics, 2006, Hindawi Publishing Coorporation,

[31] B. Ventura, D. Casarano, C. Notarnicola, D. Di Rosa, F. Posa ,and the Cassini Radar Science Team , Cassini RADAR: modeling and Bayesian inference ofphysical and morphological parameters of Titan'ssurface features, Geophysical Research, Vol. 9, 06489, 2007

[32] B. Ventura, D. Casarano, C. Notarnicola, D. Di Rosa, F. Posa, Modeling the electromagnetic response of Titan's surface features observed by Cassini Radar, 2006, Proceedings of SPIE -- Volume 6363

4 CASSINI ALTIMETER DATA PROCESSING ALGORITHMS

The main objective of the Cassini Radar Mission is Titan coverage [35]. In order to study the surface proprieties and processes of Titan, the spacecraft will make a number of close flybys during its 4-year nominal mission. During these flybys, the Cassini Radar and other instruments onboard the spacecraft will conduct intense observations, in order to achieve the scientific goals. The first targeted fly-by of Titan (Ta) occurred on Tuesday, October 26, 2004 at 15:30 UTC [33].

While operating as an altimeter (ALT mode), the instrument will be able to measure surface elevations along the sub-satellite ground tracks. At an inhospitable temperature (around 90 K), the chemistry that drives surface processes is fundamentally different from Earth's: it is methane to perform many of the same functions on Titan that water does on Earth [JPL, 2006]. As a consequence, the mapping of Titan is an especially challenging puzzle, because the most likely constituent materials in this chemical and temperature regime are likely to exhibit different scattering properties than at Earth and Venus, the only other worlds mapped by spaceborne radars [38].

In the frame of the Cassini Radar Program, the Cassini Processing of Altimetric Data (PAD) System has been conceived in order to process the data collected by the Cassini Radar, while operating as an Altimeter. The integrated software application, developed by CORISTA and Alcatel Alenia Space Italia under ASI contract, offers all the specific instruments needed to process, manage, visualize, archive and disseminate the scientific products containing all the retrieved information about the Titan surface topography, starting from the raw data as provided by JPL/NASA.

The height retrieval functionality, core of the altimetric processing, is performed by using implemented algorithms which are based on *ad hoc* developed mathematical techniques necessary to simulate analytically the average return power waveform, as obtained from the received signal, in order to cope with the particular operating conditions, and with the expected occurrence of off-nadir measurements.

In the following, after a brief introduction concerning the Cassini Radar, an overview of the PAD System architecture in terms of implemented functionalities, component applications and system design will be given.

4.1 The Cassini Radar

The Cassini Radar is a multimode microwave instrument that uses the 4 m high gain antenna (HGA) onboard the Cassini orbiter. The instrument operates at Ku-band (13.78 GHz or 2.2 cm wavelength) and it is designed to operate in four observational modes (Imaging, Altimetry, Backscatter and Radiometry) at spacecraft altitude below 100.000 Km, on both inbound and outbound tracks of each hyperbolic Titan flyby, and to operate over a wide range of geometries and conditions [38]. The instrument has been designed to have a wide range of capabilities in order to encompass a variety of possible surface proprieties.

From signal to noise and data rate considerations, the ALT mode is planned to operate at S/C altitudes between 4000 and 9000 Km, approximately from 16 min before the closest Titan approach of each Titan flyby until 16 min after the closest encounter. During such operation, the radar will utilize the central, nadir-pointing antenna beam (Beam 3, a circular beam 0.350° across) for transmission and reception of chirp pulse signals at a system bandwidth of 4.25 MHz [38, 51].

The Altimeter operates on "burst mode", similar to the imaging mode. When the ALT mode is executed, bursts of frequency modulated pulse signals (chirp pulses) of 150 μs time duration and at 5 MHz bandwidth will be transmitted in a Burst Period (the Burst Repetition Interval is 3333 ms). The transmit time varies from 1.4 to 1.8 μs. The number of pulses transmitted in each burst will vary throughout a single flyby pass.

The collected altimeter measurements are expected to have horizontal resolutions ranging between 24 and 27 Km, and a (final achievable) vertical resolution of about 30 m. In addition to the limitation due to the intrinsic vertical resolution, the accuracy in estimating the relative surface elevation (that is, the change in local surface elevation relative to a reference datum) depends also on the topographic relief of the surface as well as on the knowledge of the spacecraft's ephemeris and attitude. An estimate of such accuracy is between 100 and 150 m.

4.2 Cassini PAD System Overview

As part of the Cassini Radar Program, ASI required to process and exploit the Cassini altimetry data, by means of an *ad hoc* developed system: the Cassini Radar PAD. The implemented system contains the HW and SW tools necessary to:

- receive and elaborate the Cassini Radar Altimeter instrument raw data sets
- generate the science data products from the received Cassini Radar Altimeter data sets
- archive and manage the science data products within the system.

The system is able to manage BODP files supplied by JPL. Basically, these are data sets at various stage of processing, organized as time-ordered records for each burst. They are fixed header length and fixed record length files, compliant to PDS standards. The header is an attached PDS label. According to SIS, BODP products come in three different record formats (see [36] and [37], Vingione et al., 2007):

- Short Burst Data Record (SBDR)
- Long Burst Data Record (LBDR)
- Altimeter Burst Data Record (ABDR).

The SBDR is produced for every Titan flyby, and it is divided into three consecutive segments from three different levels of processing (Engineering, Intermediate Level and Science Data Segments) containing radar telemetry, timing and spacecraft geometry information and all relevant scientific data. The LBDR is simply a SDBR which also contains sampled echo data. The LBDR data for altimetry supplied by JPL to ASI will contain only basic engineering unit conversions and geometry calculations. The ABDR data is the same as the SBDR, except that it includes the altimeter profile. The ABDR file is generated from the altimeter processor and it can be furthermore used to perform additional altimetry processing.

The physical architecture of the PAD System is composed by several software components distributed on two operating system platforms. The server platform, supported by a Linux operating system, hosts the local data archive and acts as the domain server, while the client platform, supported by a Windows® XP Professional operating system, hosts the data processing subsystem. On the server platform, the logical component of the local data archive is the distributed file system: the local archive is accessed as a network drive by the data processing subsystem. The server handles the definition and the authorizations of the domain's groups and users to access the distributed resources. On the client platform, the data processing subsystem is represented by the Cassini Radar PAD application, installed with same functionalities on each workstation.

The core of the system is represented by processing algorithms and tools developed in a Matlab® environment. Each tool is provided with a user-friendly GUI, which allows users to exploit all implemented functionalities. The core tools are integrated into a framework, which is a standard

Windows® application written following the design specifications and guidelines of the official guidelines for user interface developers and designers.

PAD Components

The PAD System actually can be divided into six main logical components, briefly described in the following:

PAD Framework

The main functionality of the PAD Framework software is to give users a global vision of the status of all the operations that can be made on the BODP files within the Cassini Radar PAD. It provides easy access to all system functionalities. Users can select the flyby to operate and start any operation available for the processing of telemetry files.

PAD File Manager

The PAD File Manager is the software component that allows users to import the PDS telemetry files into the Local Archive, and to deliver the output ABDR products to the scientific community.

The LBDR data retrieval can be executed through the JPL secure HTTPS site, or from any file system location indicated by the user. The delivery functionality can publish the ABDR file on a public FTP repository and/or copy it to a writable portable transfer media.

PAD Data Publisher

The PAD Data Publisher is the software component containing all the commands and the methods that allow users to forward the ABDR files to the Cassini Ground System repository located at JPL. The produced ABDR file is not physically sent nor moved to the Cassini Ground System repository located at JPL. Once the PAD File Manager has published the ABDR files to the public FTP repository, the scientific community receives an e-mail notification to access the password protected repository in order to download the new available file.

ABDR Production Tool

The off-line ABDR Production Tool (PT) retrieves the input LBDR files by managing a list of LBDR files locally stored, allowing user to select the input file. After interactive selection of the LBDR file to be processed, the tool proposes to start the creation of subsets of the input LBDR product (intermediate PT Files) each containing only data records pertinent to one of the *active* Cassini Radar operational modes, i.e. Altimeter, SAR and Scatterometer mode. These files are created for internal use and stored into the local archive in both binary and ASCII format, in order to be accessed by SLT. The PT allows user to perform the generation of the ABDR product starting from the selected LBDR file. Moreover, user is allowed to interactively modify selected keywords into ABDR PDS label.

An ABDR file is produced which contains records for only the two periods (one inbound, one outbound) in which the radar is in altimeter mode, by filling in automatically all the appropriate data fields in the Science Data Segment with the values obtained from SLT processing, and by filling the end of each record in the LBDR file with the values resulting from range compression of sampled echoes data counts (i.e. the altimeter profile), starting from SLT results files. When LBDR processing is terminated, the ABDR PT stores the new file into the local archive along with a report file. Data contained into the ABDR product shall be validated by using SLT functionalities, before submission to the local file server.

<u>*Science Look Tool*</u>

The off-line Science Look Tool (SLT) is in charge to perform the altimetric processing implementing proposed models in equation (63) and (74). It is a graphical application including procedures and algorithms designed to check and simulate the performances of the Cassini Radar Altimeter through calculation, visualization and plotting of relevant parameters. The SLT uses an intermediate BODP file produced by the ABDR Production Tool, stored into the local archive, and it automatically performs range compression of sampled data.

The SLT evaluates the altimeter profile range start, altimeter profile range step and altimeter profile length required for the PT ABDR production functionality, starting from compressed data. Each compressed burst is constituted of *Np* chirp pulses. In order to reduce the speckle, a single pulse is obtained by averaging all the received pulses within the burst. Hence, each compressed burst becomes an array containing only one averaged pulse-compressed echo. The averaged bursts are stored into internal memory as bi-dimensional arrays.

The range compressed data are used to perform waveform analysis and final altitudes estimate by using different altimetry models previously implemented. In addition, the tool permits user to simulate the performances of the Cassini Radar Altimeter, thus allowing obtaining a complete analysis of ALT data from a scientific perspective.

In order to infer the significant geophysical parameters describing the surface's topography from the altimetry data, a Maximum Likelihood Estimator (MLE) has been implemented to be enclosed in the developed algorithm. The Maximum Likelihood Estimator algorithm is based on fitting averaged bursts with a theoretical model describing the Radar Impulse Response. The algorithm is able to select automatically which is the best theoretical model to be used during the processing. The selection is based on threshold criteria related to the current value of the off-nadir angle, in order to cope with the expected occurrence of near-nadir measurements along the hyperbolic trajectory followed during the flyby. All the performances have been numerically evaluated: this method ensures the best fitting of data, thus reducing the errors in heights estimation.

The SLT Tool allows users to specify the default processing parameters by using a Configuration File containing:

- threshold values for off-nadir angles
- minimum number of MLE iterations
- first attempt values
- thresholds for MLE Error Reducing Procedure, etc.

The SLT provides several auxiliary functionalities that allow the user to obtain the complete monitoring of both processing and results. On user request, the SLT provides 2-D or multi-plots of S/C and Radar ancillary data, processing results and algorithm configuration. All the results can be exported (i.e. printed/saved) by user. In addition, on user request, a report file in xml format is generated containing all the results produced by the SLT, e.g. relevant processing parameters, MLE procedure results, relative elevations of Titan's surface vs. along-track distance (i.e. topographic profiles), altimeter waveforms vs. range bins, ancillary data (e.g. observation geometry and orbital parameters vs. time, instrument data, etc.), surface parameters vs. along-track distance, etc. It will be used by scientists for further validation of data, which is propaedeutical to ABDR production.

Map Tool

The off-line PAD Map Tool (MT) is a graphical application that allows users to visualize and navigate through Titan's 2D and 3D maps, finalized to the analysis of their informative content, as immediate instrument of interpretation of scientific data. From the point of view of scientific surveying, altimetric maps could be confronted and joined with maps obtained by radiometric surveys and with the analysis made by other instruments onboard the Cassini Spacecraft, in order to provide a global vision, as far as it is possible, of the characteristics of Titan's surface.

The purpose of MT is the production of altimetric regional maps obtained by visualization of sub-satellite ground-tracks and overlapping of data collected along tracks to a pre-existent map of Titan, over the region illuminated by the Cassini Radar in high-resolution ALT mode, for each Titan fly-by. Hence, Titan's maps represent the final results of data processing. The realization of the altimetric map can be accomplished by referencing the radar altimetry profile with respect to the surface of Titan.

The Titan's altimetric maps are generated starting from SBDR, LBDR and BIDR data files, and from output data produced by the SLT (e.g. the topographic profile with information about the surface slope, etc.) which could be superimposed to referenced images of Titan surface in a given projection. The content of SBDR, LBDR and BIDR data files is extracted by means of a *Data Production Utility*, which saves all relevant information needed to produce MT datasets (map internal files) containing satellite geometry, Scatterometer, Radiometer and SAR data, which becomes then available to Map Tool for visualization.

The SLT output data needed to MT procedures execution are retrieved from the local archive or database. Titan's images (e.g. Mercator albedo maps from HST, ESO, etc, images acquired by optical observation by the Cassini ISS, etc.) to be used as map background, shall be made available, for example by the Cassini Ground System at JPL/NASA, and shall be also stored in the local database. All maps produced by the Map Tool are stored into the local archive, for further distribution.

4.3 Cassini ALTH Models Implementation

As previously mentioned, the implementation of the parameters estimation process into the Cassini PAD is performed by using a Maximum Likelihood (ML) estimator algorithm. The main outputs of MLE algorithm are the time delay and surface roughness. A diagram containing main parameters estimation processing is reported in Figure 56. Evaluation of estimated variables is split into three main actions using dedicated algorithms:

- First Attempt values evaluation
- Selection, update and evaluation of theoretical model and dedicated gating functions
- MLE errors evaluation and heights computations

Dedicated flags are used to establish which model and gating function shall be used to fit the Cassini Radar data. The flags are:

- *nadir_flg*
- *prony_flg*

The value of each flag (false=0 or true=1), related to threshold values for the off-nadir angle, are evaluated according to consideration made section 3.5.1 and reported in Figure 55.

In particular, if:

- nadir_flg=1 & prony_flg=0, will be selected the theoretical nadir model [see equation (28)] and relatives gating functions.
- nadir_flg=0 & prony_flg=1, will be selected the theoretical off-nadir model and relatives gating functions derived by Prony's approximation.
- nadir_flg=0 & prony_flg=0, will be selected the theoretical off-nadir derived by asymptotical form of flat surface response model and relatives gating functions.

In the following an example of pseudocode is reported.

```
if (current off nadir value <threshold1)
    nadir_flg=1;
    prony_flg=0;
     NN=0;
  elseif (current off nadir value < threshold2)
    nadir_flg=0;
    prony_flg=1;
    NN(index)=2;
  elseif (current off nadir value < threshold3)
    nadir_flg=0;
    prony_flg=1;
    NN(index)=3;
  elseif (current off nadir value < threshold4)
    nadir_flg=0;
    prony_flg=1;
    NN(index)=4;
  else
    nadir_flg=0;
    prony_flg=0;
    NN=0;
  end
```

```
if ( nadir_flg==1 & prony_flg==0 )
        modello=IR_nadir_model
       gate_time=gate_time_nadir
   elseif (nadir_flg==0 & prony_flg==1 );
      [modello aa cc]=IR_model_Prony
      gate_time=gate_time_Prony
   else (nadir_flg==0 & prony_flg==0 );
      modello=IR_Brown_asymptotic
      gate_time=gate_time_Brown
end
```

After the appropriate model selection, the MLE algorithm evaluates the error in estimation process by implementing the following equation or each variable to estimate:

$$error\Big|_{i=1}^{N} = \frac{V-\overline{V}}{\overline{V}^2}\cdot\frac{\partial\overline{V}}{\partial\underline{A}}$$

Starting from above errors the algorithm updates the value of variables and repeats the process until the error will be greater than threshold value.

It is worth noting that, at each iteration, the algorithm evaluates the model and gating function by using current estimated variables. At first iteration, errors values must be initialized to zero and the values of variables (to be estimated) must be initialized. In order to perform the estimation algorithm, more estimation loop shall be executed, one for each variables to estimate.

In order to solve for the MLEs of interest parameters, it is possible to implement an iterative cycle using, at first attempt, initial values of variables. Hence, to perform the MLE process it is necessary to initialize the algorithm with first attempt values, in particular the centroid position (related to the time delay) and pulse amplitude. The process is repeated for each burst, as shown in following figure.

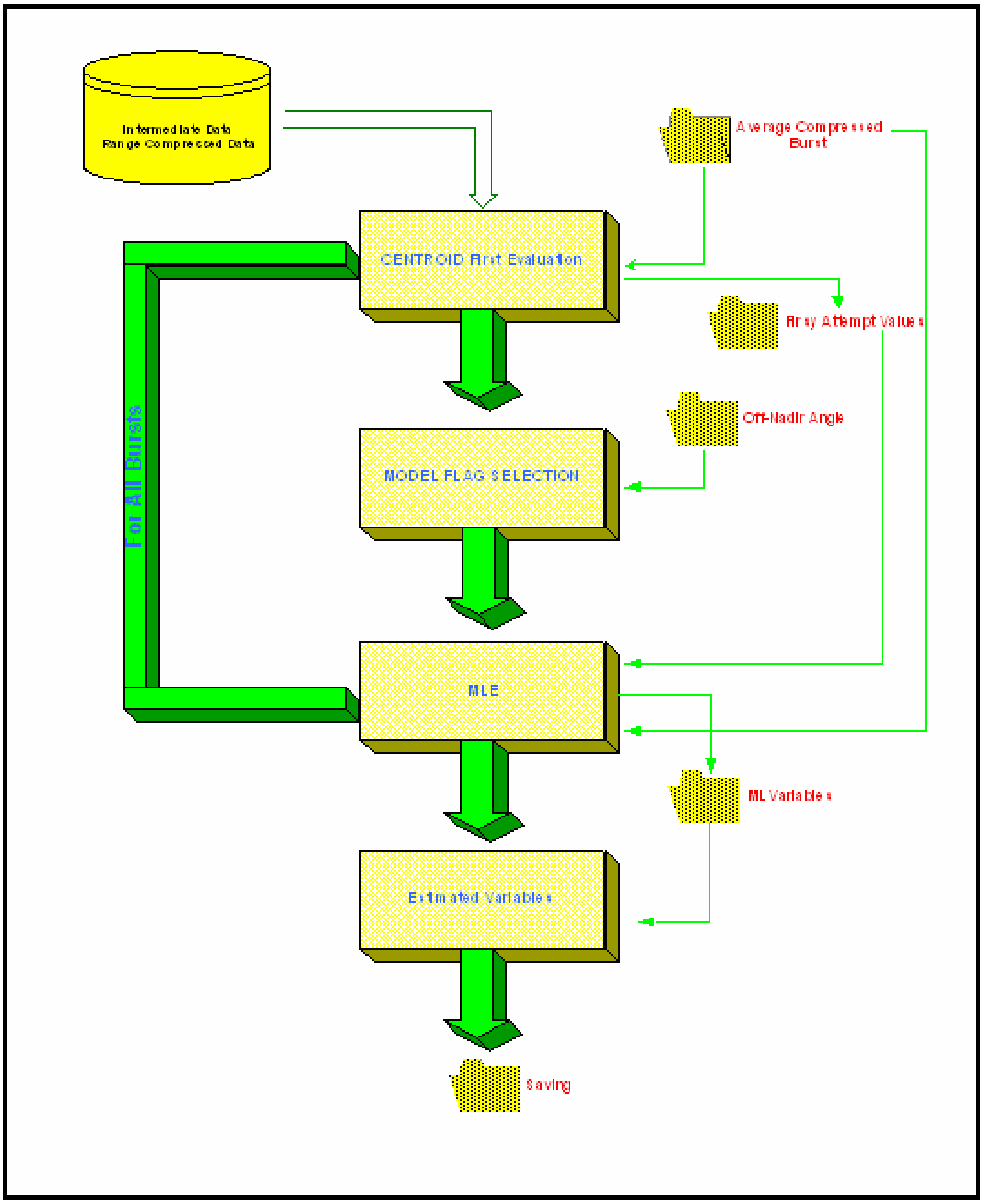

Figure 56 – Cassini MLE algorithm implementation

4.4 Cassini Model Implementation: final considerations

The implementation of MLE algorithm combined with proposed models allowed to identify some anomalies into the averaged range compressed data received from Cassini Radar. A typical range compressed impulse is shown in Figure 57. For each range compressed impulse the MLE performs a best fitting process by using models expressed in equations (63) and (74). A typical process of convergence, for which it is required a number of iterations not greater than 10, is shown in Figure 58 (first step, N=1, of the MLE iterations) and Figure 59 (last step, N=20 of the MLE iterations). The errors in best fitting process trend asymptotically to zero, as showed in Figure 60.

Sporadically the following anomalies have been identified into the Cassini range compressed pulse:

- Echoes spreading (see Figure 61)
- Double peaks into the 3dB pulse band (see Figure 63)
- Secondary lobes (see Figure 64)

The effect of these anomalies on MLE loop is the divergence of the algorithm (see Figure 65) and consequentially the propagation of the error in height retrieval estimation (see the peak in Figure 67).

By analysing the MLE errors it is possible to mark the anomalous pulses and correct the corresponding time delay estimation in post-processing analysis (when anomalies causes are well understood).

By excluding errors in range compression matched filtering, the possible causes of these anomalies are addressed to target surface composition. On basis of the present analysis it is not possible yet to identify the real nature of the above anomalies except for the double peaks into the 3dB pulse band.

In last case, in fact, the simulations showed that nature of double peaks can be related to the speckle distribution (see Figure 66).

Regarding the other anomalies the following possible sources could be identified:

- Volumetric Scattering <=> Secondary lobes
- Sub-surface clutter <=> Secondary lobes
- Surface slope <=> Echoes spreading

Further analysis is required to model the effects of Volumetric Scattering and to delete eventually clutter distortions.

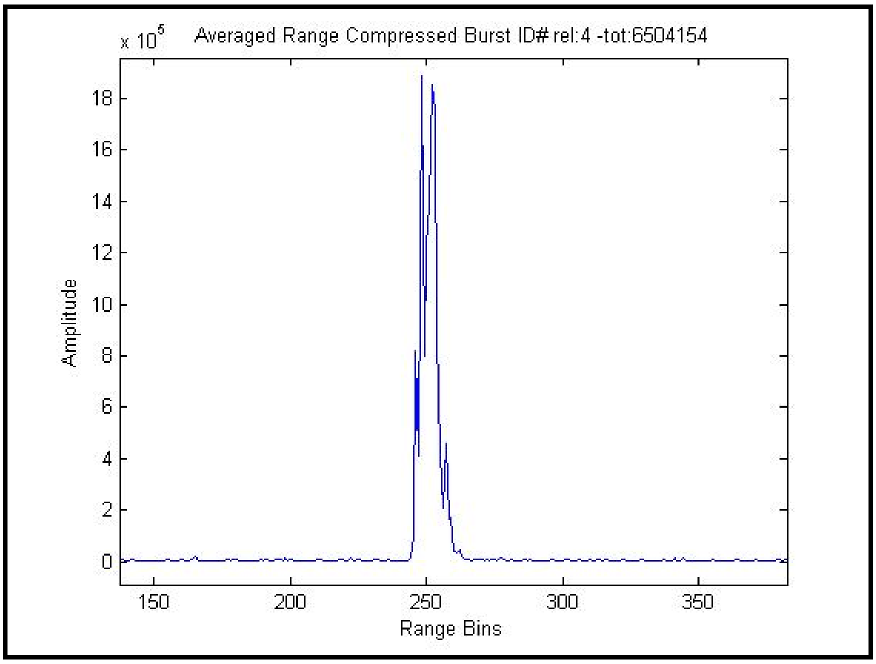

Figure 57 – Cassini T3 Range Compressed Pulse #65016572

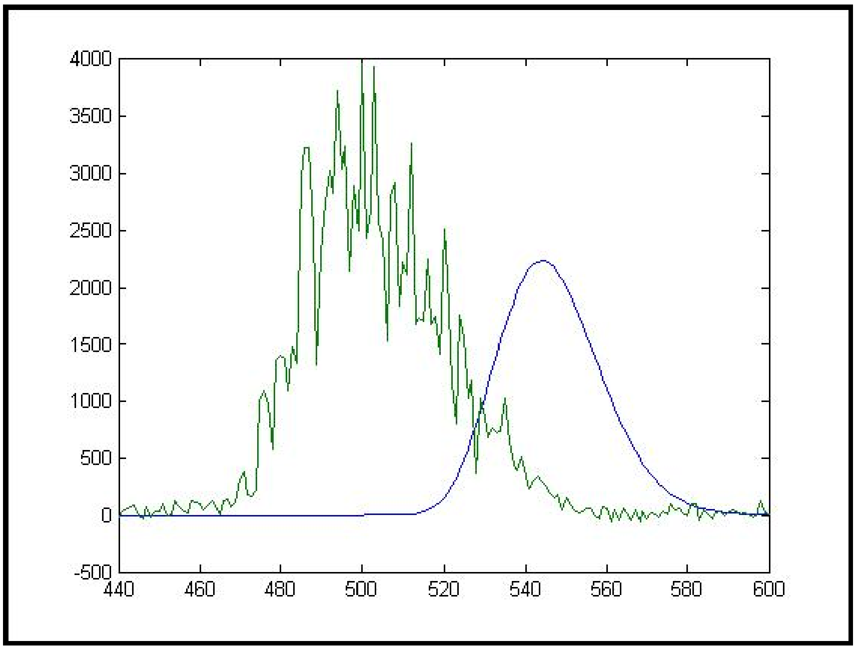

Figure 58 – MLE Best fitting process: 1st step

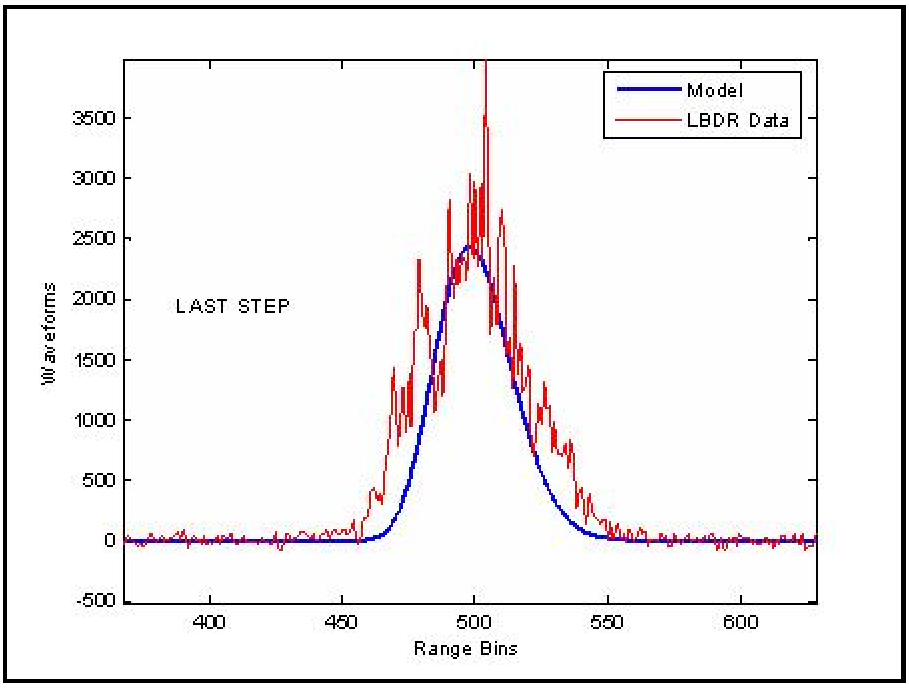

Figure 59 – MLE Best fitting process: last step

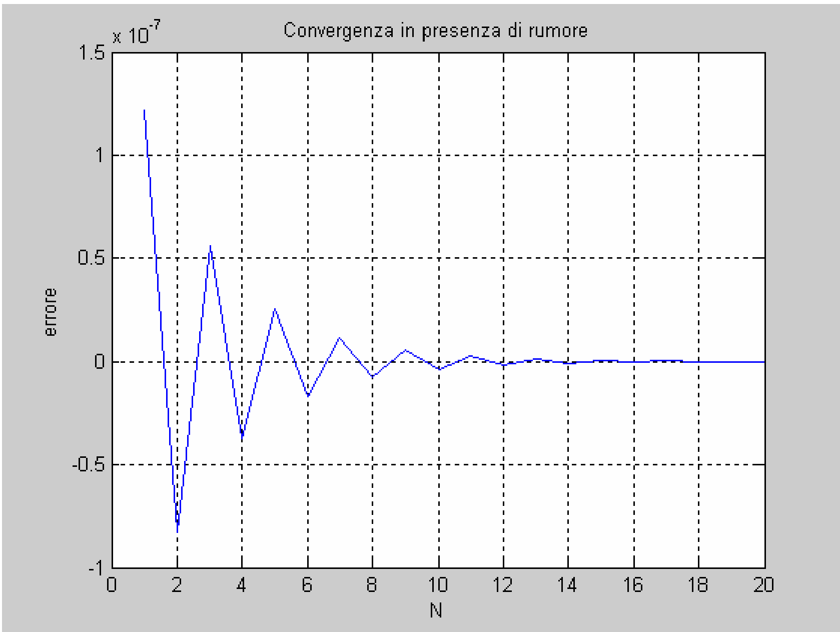

Figure 60 – MLE Best fitting process: error convergence.
(It is evident that at iteration 10^{th} the error is practically zero)

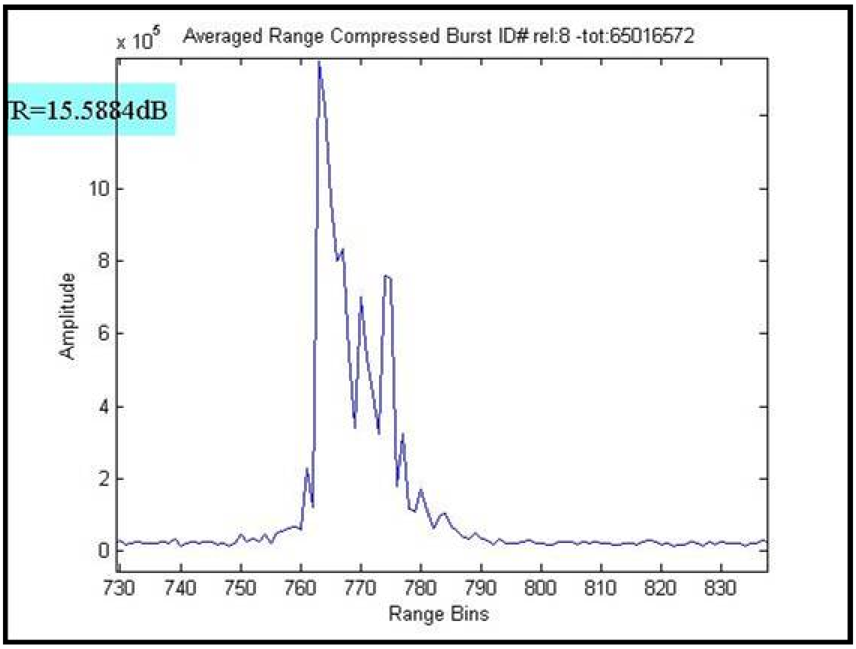

Figure 61 – Cassini Ta Range Compressed Pulse #65016572.
(Example of impulse spreading)

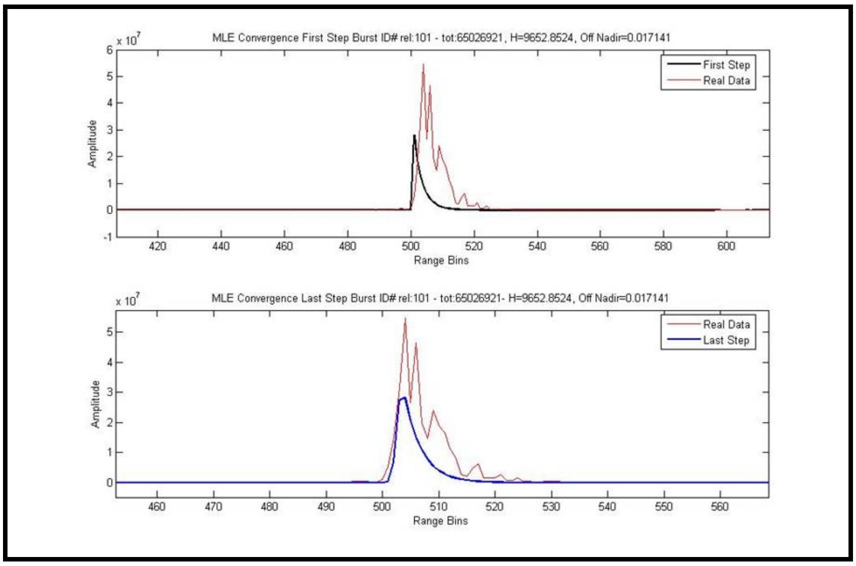

Figure 62 – Example of fitting impulse spreader.
It is possible to note that theoretical models is not able to fit the pulse (which is “larger” than the theoretical one)

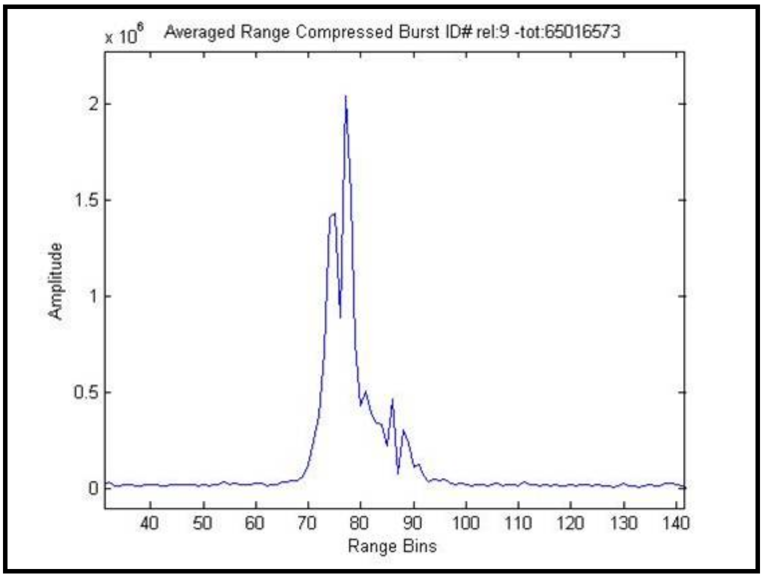

Figure 63 – Cassini T3 Range Compressed Pulse #65016573
Example of double peaks into the band.

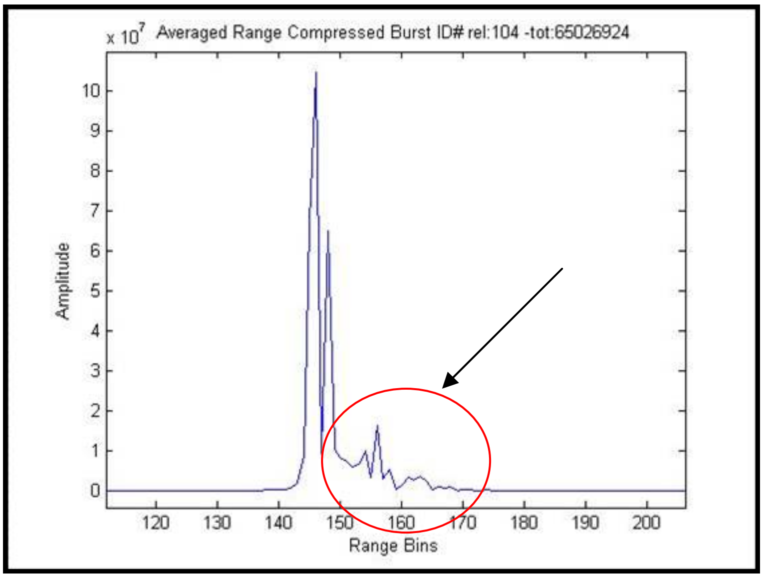

Figure 64 – Cassini T3 Range Compressed Pulse #65026924
Example of secondary lobes

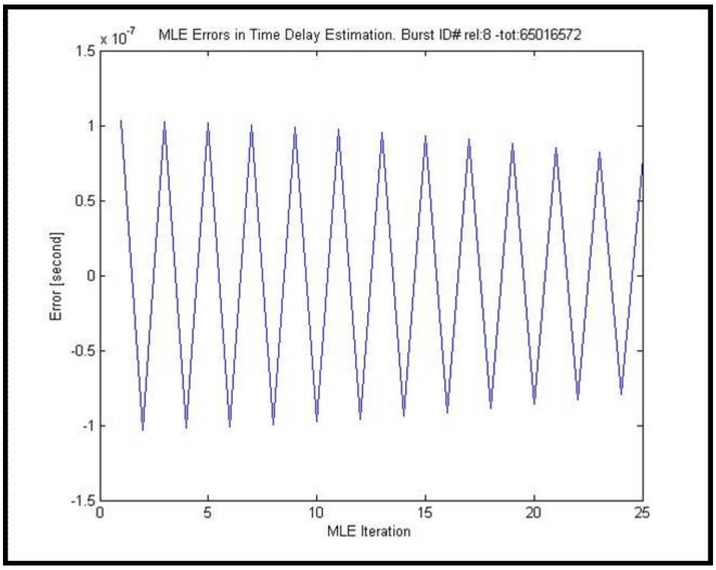

Figure 65 – MLE Best fitting process: error divergence.
It is clear that the model it is not able to fit the real data and the error diverges.

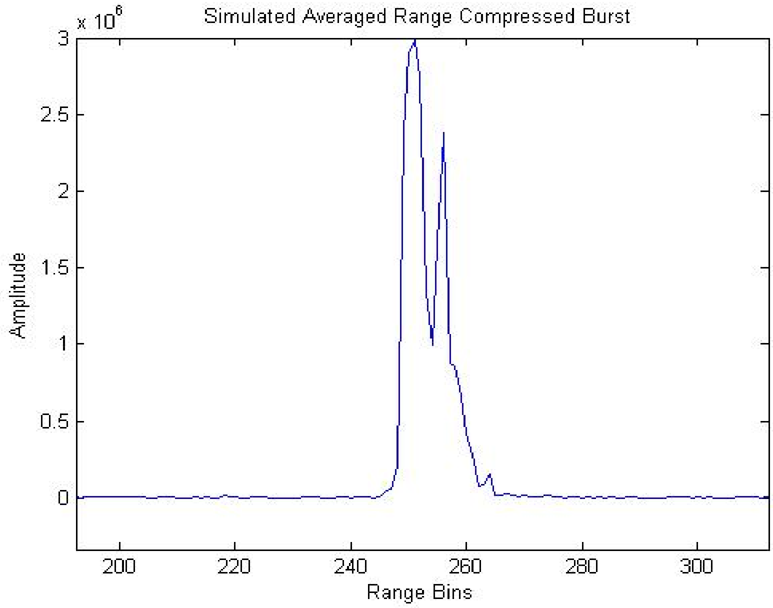

Figure 66 – Simulation of Averaged Range Compressed Pulse
(It is possible to note the presence of a double peak into the 3dB band. This is due to the nature of the speckle phenomena)

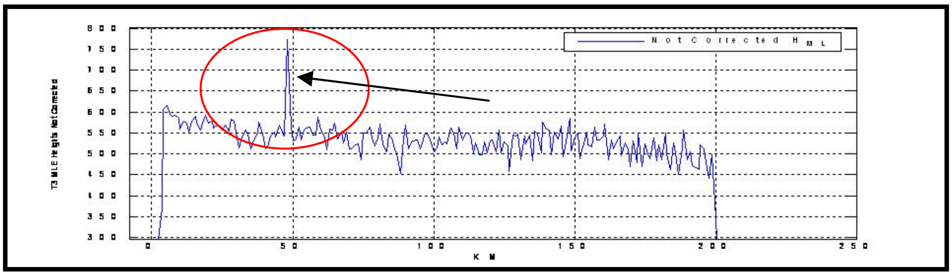

Figure 67 – The MLE divergence becomes an error in topography estimation as clearly shown in the red box

REFERENCES

[33] JPL Publication No.D-11777, Cassini Document 699—070-2, Cassini Program Environmental Impact Statement Supporting Study.

[34] Cassini Mission Plan Document, D. Seal, 2003. (JPLD-5564)

[35] The Cassini-Huygens Mission to the Saturnian System, Dennis Matson, Space Science Reviews 104: 1–58, 2002.

[36] G. Alberti, L. Festa, G. Vingione , E. Flamini (Agenzia Spaziale Italiana), R. Orosei (Istituto Nazionale di Astrofisica), G. Picardi, R. Seu (Università di Roma "La Sapienza"), "The Processing of Altimetric Data (PAD) System for Cassini RADAR", VII Convegno Nazionale di Scienze Planetarie, 5-9 settembre 2006, San Felice al Circeo (LT), Italia.

[37] G. Vingione, G. Alberti, C. Papa, L. Festa (CO.RI.S.T.A), G. Picardi, R. Seu, P.P. Del Marmo (INFO-COM, University of Rome La Sapienza), R. Orosei (IASF Istituto di Astrofisica Spaziale e Fisica Cosmica, CNR), P. Callahan, S. Wall (Jet Propulsion Laboratories, California Institute of Technology), "Processing of Altimetric Data of CASSINI mission", European Geosciences Union General Assembly 2007 Vienna, Austria, 15 – 20 aprile 2007. See http://www.corista.unina.it/docs.html

[38] Charles Elachi, Cassini Titan Radar Mapper, Proceeding of the IEEE, Vol.79,N°6, June 1991

[39] R. Lorenz *et al.*, *Planet. Space Sci.* **47**, 1503 (1999)

[40] D.Casarano, F.Posa, R.D.Lorentz, 2000, CASSINI RADAR: data analysis of the Earth flyby and simulation of Titan flyby's data, Icarus.

[41] R.D.Lorentz ea al., 2003, CASSINI RADAR: prospects for Titan surface investigations using the microwave radiometer, Planetary and Space Science 51, 353-364

[42] Eastwood, Johnson, Hensley, 2000, CASSINI RADAR for Remote Sensing of Titan-Design Considerations, JPL.

[19]. L.Borgarelli, G.Picardi, R.Seu, 1995, Altimetry in the Cassini mission, IEEE 0-7803-2567-2, 1598-1600.

[43] Ralph Lorenz, Oct 2000, The Weather on Titan, Planetary and Space Science 290, Number 5491, Issue of 20, pp. 467-468.

[44] David Doody, George Stephan, 1995, Basic of Space Flight, JPL D-9774 Rev.A

[45] J.H.Vilppola, 1998, Cassini Mission and the CAPS/IBS Instrument, University of Oulu

[46] S.Pessina, S.Campagnola, M.Vasile, Preliminary Analysis of

Interplanetary Trajectories with Aerogravity and Gravity Assist Manoeuvres , 1999

[47] http://www.jpl.nasa.gov/cassini

[48] http://www.sp.ph.ic.ac.uk/~nach/mag_planning.html

[49] Eastwood, Johnson, Wheeler, 1994, Developement Status of Cassini Radar for Remote Sensing of Titan, IEEE 0-7803-1947,2, 1562-1564

[50] Ralph Lorenz, J. Lunine, 1997, *Titan's surface reviewed : the nature of bright and dark terrain*, *Planet. Space Sci.* VOL.45 N°8, 981-992

[51] K.S. Chen, A.K. Fung, 1992, *A backscattering Model for Ocean Surface*, IEEE VOL.30, N°4, 811-817

[52] Monfredini, Seu, Picardi, Morelli, 1995, *A non coherent surface backscattering model for radar observation of planetary bodies and its applications to Cassini radar altimeter*, *Planet. Space Sci.* VOL.43 N°12, 1567-1577

[53] Curlander, Mc Donough, 1991, *Syntethic Aperture Radar Systems and Signal Processing*, John Wiley Publications

[54] Samuel et al., 1998, *Performance Analysis of an Topography Mission Final Report*, ESTEC Contract N° 12124/NL/CN

[55] W.G.Rees, Physical *Priciples of Remore Sensing* (2nd ed.), Cambridge University Press, Cambridge UK, 343 pp.

[56] Bamber, 1994, *Ice sheet altimeter processing scheme*, International Journal of Remote Sensing, VOL. 15, N°4, pp. 925-938

[57] C.Elachi, 1988, *Spaceborne Radar Remote Sensing: Applications and Techniques*, IEEE Press, New York

5 CONCLUSIONS

In this work, a model for estimating the radar altimeter performance has been derived [see equations (63) and (74) presented in section 3]. Unlike the previous existing models, with the proposed method, the estimated Impulse Response is independent from the specific operative conditions and instrument characteristics (Pulse Limited or Beam Limited). This implies that above equations are capable of modelling the average return waveforms for an altimeter system with no restriction on altitude, antenna beamwidth or transmitted pulsewidth. Previous models had restrictions on one or more of these system parameters, which rendered them incompatible with waveform modelling for high altitude or beamwidth limited altimetry remote sensing.

The proposed models have been implemented and tested by using dedicated simulator. Provided simulations demonstrate that above equations are not sensitive to pointing angle variations (as the pulse limited system for low altitude operation typical of the Earth Observation scenarios). The only criterion to take into account is a thresholding selection of the appropriate equation, according to consideration made in section 4.3.

Furthermore, due to specific Cassini mission constrains, the proposed models have been selected to be implemented into the Cassini Processing Altimetric Data ground system, actually installed and integrated at Thales Alenia Space Italia premises in Rome, funded by Italian Space Agency. The models presented in this work represent the core of the nominal processing algorithm for the Cassini altimeter data. The first results show the capability of the models to fit the compressed burst received from the Cassini Radar, for very different fly-by, allowing to obtain a topographic profile of the Titan moon more accurate than the corresponding profile estimated by JPL_NASA and based on leading edge algorithm.

The results shown during both simulations and processing analysis (of Cassini ALTH data) suggest, hence, that proposed models are suitable for all the altimetry processing scenarios. Applicability diagram provided in Figure 55 represents an useful guideline to be applied in order to guarantee, in processing the real data, a maximum error of 2% respect to numerical integration of the convolution model.

Another relevant advantage in using the proposed equations is the possibility to manipulate analytical solutions (not numerical). That allows to adopt classical estimation algorithm (i.e. Maximum Likelihood Estimation) in order to retrieve statistical information about investigated target surface. This implies that, unlike classical processing algorithms (leading edge, adaptive noise thresholds, etc.), the equations (63) and (74) allow to distinguish the difference between height anomalies due to noise peak and a change in real topography.

In addition, the implementation of the models into the Cassini ground System has shown also that the potential errors that could be introduced in height retrieval algorithms can be reduced at manageable levels and corrected for by leaving the traditional leading edge processors.

In conclusion, this work has demonstrated the need of using predicted pulse waveforms for altimeter measurements. General altimeter waveform models can ensure the improvement of altimetry processing techniques and, as a consequence, of the processing outputs accuracy. Therefore, general altimeter models can be combined, in a post-processing phase, with geoid precise models in order to derive a global topography model for the target surface. In particular for Earth Observation scenarios, the possibility to combine altimetry models with additional theoretical models could make possible the global modelling of the Earth dynamic system.

APPENDIX A – PRONY'S APPROXIMATION METHOD

Prony analysis is a method of fitting a linear combination of exponential terms to a signal as shown in (A1). Each term in (A1) has four elements: the magnitude A_n, the damping factor σ_n, the frequency f_n, and the phase angle θ_n. Each exponential component with a different frequency is viewed as a unique mode of the original signal *y(t)*. The four elements of each mode can be identified from the state space representation of an equally sampled data record. The time interval between each sample is T:

$$y(t) = \sum_{n=1}^{N} A_n e^{\sigma_N t} \cos(2\pi f_n t + \theta_n), \text{ n=1,2,3,....N} \qquad \text{(A1)}$$

Using Euler's theorem and letting $t = MT$, the samples of *y(t)* are rewritten as (A2):

$$y_M = \sum_{n=1}^{N} B_n \lambda_n^M \qquad \text{(A2)}$$

where:

$$B_n = \frac{A_n}{2} e^{j\theta_n} \qquad \text{(A3)}$$

and

$$\lambda_n = \exp[(\sigma_n + j2\pi f_n)T] \qquad \text{(A4)}$$

Prony analysis consists of three steps. In the first step, the coefficients of a linear predication model are calculated. The linear predication model (LPM) of order N, shown in (A5), is built to fit the equally sampled data record *y(t)* with length M. Normally, the length M should be at least three times larger than the order N:

$$y_M = a_1 y_{M-1} + a_2 y_{M-2} + ... + a_N y_{M-N} \qquad \text{(A5)}$$

Estimation of the LPM coefficients a_n is crucial for the derivation of the frequency, damping, magnitude, and phase angle of a signal. To estimate these coefficients accurately, many algorithms can be used. A matrix representation of the signal at various sample times can be formed by sequentially writing the linear prediction of y_M repetitively. By inverting the matrix representation, the linear coefficients a_n can be derived from (A6). An algorithm, which uses singular value decomposition for the matrix inversion to derive the LPM coefficients, is called SVD algorithm,

$$\begin{bmatrix} y_N \\ y_{N+1} \\ \bullet \\ y_{M-1} \end{bmatrix} = \begin{bmatrix} y_{N-1} & y_{N-2} & \bullet & y_0 \\ y_N & y_{N-1} & \bullet & y_1 \\ \bullet & \bullet & \bullet & \bullet \\ y_{M-2} & y_{M-3} & \bullet & y_{M-N-1} \end{bmatrix} \begin{bmatrix} a_1 \\ a_2 \\ \bullet \\ a_N \end{bmatrix} \qquad \text{(A6)}$$

In the second step, the roots λn of the characteristic polynomial shown as (A7) associated with the LPM from the first step are derived. The damping factor σ_n and frequency fn are calculated from the root λ_n according to (A4):

$$\lambda^N - a_1\lambda^{N-1} - \ldots - a_{N-1}\lambda - a_N = (\lambda - \lambda_1)(\lambda - \lambda_2)\ldots(\lambda - \lambda_N) \qquad \text{(A7)}$$

In the last step, the magnitudes and the phase angles of the signal are solved in the least square sense. According to (A2), (A8) is built using the solved roots λ_n:

$$\underline{Y} = \Phi \underline{B} \qquad \text{(A8)}$$

where:

$$\underline{Y} = [y_0, y_1, \ldots\ldots, y_N]^T$$

$$\underline{\underline{\Phi}} = \begin{bmatrix} 1 & 1 & \bullet & 1 \\ \lambda_1 & \lambda_2 & \bullet & \lambda_N \\ \bullet & \bullet & \bullet & \bullet \\ \lambda_1^{M-1} & \lambda_2^{M-1} & \bullet & \lambda_N^{M-1} \end{bmatrix}$$

$$\underline{B} = [B_1, B_2, \ldots\ldots, B_N]^T$$

The magnitude A_n and phase angle θ_n are thus calculated from the variables B_n according to (A3). The greatest advantage of Prony analysis is its ability to identify the damping factor of each mode in the signal. Due to this advantage, transient harmonics can be identified accurately.

APPENDIX B –AUTHOR'S PUBBLICATIONS

- G. Alberti, L. Festa, G. **Vingione** , E. Flamini (Agenzia Spaziale Italiana), R. Orosei (Istituto Nazionale di Astrofisica), G. Picardi, R. Seu (Università di Roma "La Sapienza"), "The Processing of Altimetric Data (PAD) System for Cassini RADAR", *VII Convegno Nazionale di Scienze Planetarie, 5-9 settembre 2006, San Felice al Circeo (LT), Italia.*
- A.Tassa, G. **Vingione** ,A. Buongiorno, E. Monjoux, , 2006, From Telemetry to Level 1b: GOCE Processing Flows and Products, *Proc. Of the 3rd GOCE International User Workshop, Rome, Italy, Nov. 6-8. http://earth.esa.int/goce06/*
- A.Tassa, G. **Vingione,** A. Buongiorno, E. Monjoux, 2006, From Telemetry to Level 1b: GOCE Processing Flows and Products, *PowerPoint presentation held during the 3rd GOCE International User Workshop, Rome, Italy, Nov. 6-8. http://earth.esa.int/goce06/*
- A.Tesseri, **G. Vingione**, E. Boissier, GOCE Level 1b Products: XML Formats and data access tools, *Proc. Of the 3rd GOCE International User Workshop, Rome, Italy, Nov. 6-8. see http://earth.esa.int/goce06/*
- M. Epifani, A. Tassa, G. **Vingione**, A. Buongiorno, Total Electron Content (TEC) estimations from very low orbit satellite GOCE, *European Geosciences Union General Assembly 2006, Vienna, Austria, 02 – 07 April 2006*
- G. Vingione, G. Alberti, C. Papa, L. Festa (CO.RI.S.T.A), G. Picardi, R. Seu, P.P. Del Marmo (INFO-COM, University of Rome La Sapienza), R. Orosei (IASF Istituto di Astrofisica Spaziale e Fisica Cosmica, CNR), P. Callahan, S. Wall (Jet Propulsion Laboratories, California Institute of Technology), "*Processing of Altimetric Data of CASSINI mission*", European Geosciences Union General Assembly 2007 Vienna, Austria, 15 – 20 aprile 2007. See http://www.corista.unina.it/docs.html
- C. Caramiello, G. **Vingione**, A. Tassa, A. Buongiorno, Image superresolution via filtered scales integral reconstruction for

GOCE Geoid Model, *International Union of Geodesy and Geophysics (IUGG) Perugia 2007*

- G. Alberti, G. **Vingione** et al., *Innovative Radar Altimeter waveform modelling,* Planetary and Space Science (Paper Submitted, **UNDER REVIEW**)